Measurement and Device Design of Left-Handed Metamaterials

by

Zachary M. Thomas

B.S. Electrical Engineering
Syracuse University, 2003

Submitted to the
Department of Electrical Engineering and Computer Science
in partial fulfillment of the requirements for the degree of

Masters of Science in Electrical Engineering

at the

MASSACHUSETTS INSTITUTE OF TECHNOLOGY

June 2005

Author .....
Department of Electrical Engineering and Computer Science
May 19, 2005

Certified by.....
.....
Jin Au Kong
Professor
Thesis Supervisor

Certified by....
.....
Tomasz M. Grzegorczyk
Research Scientist
Thesis Supervisor

Accepted by...
Arthur C. Smith
Chairman, Department Committee on Graduate Students

Measurement and Device Design of Left-Handed Metamaterials

by

Zachary M. Thomas

Submitted to the Department of Electrical Engineering and Computer Science
on May 19, 2005, in partial fulfillment of the
requirements for the degree of
Masters of Science in Electrical Engineering

Abstract

The properties of a variety of left-handed metamaterial (LHM) structures are analyzed and measured to verify consistent behavior between theory an measurements. The structures are simulated using a commercial software program and a retrieval algorithm is used to determine the effective constitutive parameters. The constitutive parameters are used to predict the behavior of the metamaterial under various configurations. Measurements are conducted to verify the presence of a negative index of refraction. Transmission through an LHM slab from several incidences is shown to be consistent with theory.

A four-port device utilizing the dispersive nature of an LHM prism is designed and measured. The measurements show that the refraction angle of an incident signal is frequency dependent. Two ports are constructed to receive the positively refracted and negatively refracted power. In the frequency band where the incident signal cannot propagate in the LHM prism, the power is reflected from the interface towards a third measurement port. The three ports are shown to achieve unique mutually exclusive bandwidths. A general study is conducted on the design of such a device.

Finally, the use of a left-handed metamaterial as a substrate for a microstrip line is investigated. An LHM substrate consisting of split-ring resonators is shown to enhance the performance of a stop band filter. The measurement results are in good agreement with simulation where the substrate is modelled by its effective medium parameters.

Thesis Supervisor: Jin Au Kong
Title: Professor

Thesis Supervisor: Tomasz M. Grzegorczyk
Title: Research Scientist

Acknowledgments

This material is based upon work supported under a National Science Foundation Graduate Research Fellowship. Any opinions, findings, conclusions or recommendations expressed in this publication are those of the author(s) and do not necessarily reflect the views of the National Science Foundation.

This material is based upon work supported under a National Science Foundation Graduate Research Fellowship. This work was sponsored by the Department of the Air Force under Air Force Contract F19628-00-C-0002, and the ONR under Contract N00014-01-1-0713. Opinions, interpretations, conclusions and recommendations are those of the author and are not necessarily endorsed by the United States Government.

A special thanks is due to the number of people who have made this thesis possible. I'd like to thank my thesis supervisors Dr. Tomasz M. Grzegorczyk and Professor Jin Au Kong for their assistance and support over the past two years. They have made CETA a wonderful place to work and do research.

I'd like to thank the coauthors for the publications that have resulted from this work. Namely they aforementioned advisors, Dr. Bae-Ian Wu, and Xudong Chen. Their contributions have been invaluable.

The many member of CETA with whom I've shared some time at MIT also deserve my sincere thanks. This includes the aforementioned as well as the current members James Chen, M'baye Diao, Shaya Famenini, Brandon Kemp, Jie Lu, Wallace Wong, Beijia Zhang, visiting members Soon Cheol Kong, Hongsheng Chen, Dr. Ran Lixin, and former members Dr. Benjamin Barrowes, Dr. Christopher Moss, and Dr. Joe Pacheco Jr.

The inspiration I've received from friends old and new has also made these last two years a pleasure. I'd like to specifically thank Vasanth, Laura, Shubahm, Holly, Keith, Jamie, Chris, Jerid, Tim, Mike, Rich, Alex, Peter and Eric.

I'd like to thank my academic mentors Dr. Jay Kyoon Lee, and Dr. Lisa Osadciw, as well as my spiritual mentors Dr. Brother Thomas Purcell OFM Conv, and my aunt Sister Jeremy Midura CSSF.

I'd like to also thank my entire family; it's not to large to list. I thank my immediate family, my mother Christine, father Isaac, sister Margot; my aunts and uncles Jackie and Larry, and Tina and Richard; and my cousins Missy, Greg, and Joe. A special thanks to my living grandparents, Kathy and Ike Thomas, and Veronica Midura.

This thesis is dedicated to the memory of my deceased grandfather Casmier Midura.

Contents

List of Figures

List of Tables

Chapter 1

Introduction

The interaction of electric and magnetic fields with materials plays a central role in the study of electromagnetics. In general materials are complex arrangements of atoms and molecules, each of which contributes to the scattering of an electromagnetic wave. Fortunately in describing the interaction of an electromagnetic wave with a material, an approximation can be made when the structure of the material is much smaller than the wavelength, λ. In this case the material can be described by relational constants called constitutive parameters. In simple media only two constants are needed. The permittivity, ϵ, describes the relationship between the electric field strength, $\overline{E}$, and the electric displacement, $\overline{D}$. The permeability, μ, describes the relationship between the magnetic field strength, $\overline{H}$, and the magnetic flux density, $\overline{B}$. The constants are determined from the scattering properties of the material.

In more complicated materials the constitutive parameters may depend on the direction of the wave. In this case permittivity and permeability are described the tensors $\bar{\bar{\epsilon}}$ and $\bar{\bar{\mu}}$. Such a material is said to be anisotropic. Most generally, bianisotropic materials exist where $\overline{D}$ and $\overline{B}$ are proportional to both $\overline{E}$ and $\overline{H}$. Up to seventy-two parameters are needed to describe such a material.

The constitutive parameters of most natural materials have positive real parts. An exception is a class of materials called plasmas where the presence of free electrons results in a volume current when excited by an electromagnetic wave [1]. The effective permittivity of such a medium is described by negative values for frequencies below

the plasma frequency. When this occurs the wave number, k, becomes imaginary ($k = \omega\sqrt{\epsilon\mu}$), and a wave of the form, $E(x) = E_o e^{ikx}$, is evanescent.

If it were possible to have a medium where the permeability was also negative for the same frequency as the permittivity, however, the wave number would be real and the wave would propagate. In 1968 Victor Veselago published a paper that discussed such a hypothetical media having simultaneously negative values of permeability and permittivity and showed that indeed an electromagnetic wave could propagate in such a medium [2]. Veselago showed that if such an isotropic material existed, the wave vector would be anti-parallel to the direction of the group velocity. This is distinctly different from the isotropic media with positive ϵ and μ where the wave vector and group velocity are parallel. Veselago coined the name "left-handed substances" to refer to these materials because of the left-handed triad formed by the $\overline{E}$, $\overline{H}$ and $\bar{k}$ vectors. This is in contrast to the "right-handed substance," where the triad is right-handed. Veselago showed that a left-handed substance will have a negative index of refraction, negative phase advance, and the reversal of the Vavilov-Cerenkov effect and Doppler shift.

Without a material to demonstrate these predicted properties, Veselago's work was likely regarded by some as academic nimiety for the subsequent thirty years. Further consideration in the literature of such a media is either esoteric or nonexistent. The idea of left-handed substances remained primarily dormant until 1998 when J.B. Pendry published a method to achieve negative permittivity at microwave frequencies [3]. In 1999 Pendry followed that work with a method to achieve negative permeability at microwave frequencies [4] as well. In both works Pendry used the well known fact that metal inclusions in an insulator could change the effective material properties [5]. Pendry's insight was that the use of a resonant structure could drastically change the properties for frequencies near the resonance, and in fact negative values could be achieved for the properly designed resonator. The use of repetitive metallic inclusions inside an insulator were shown to produce these novel constitutive parameters. In this work we refer to any material designed to achieve negative permittivity or negative permeability by using metallic inclusions as a left-handed

metamaterial, or LHM.

Not long after [3] and [4] were published, several experiments were conducted demonstrating the presence of negative permittivity and permeability in a material [6, 7, 8]. These experiments use split-ring resonators to produce negative permeability and rod structures to produce negative permittivity simultaneously.

With both a methodology to achieve negative parameters and its verification, the field of left-handed materials was legitimized as physically meaningful. Research in the area has grown quickly, and practically every area of electromagnetism bares reinvestigation in this new light. Work has concentrated both on the theoretical consequences of negative parameters and methods of practically realizing LHM for various applications. Many of the phenomena that Veselago predicted for LHM have been under thorough investigation. Of particularly great interest is the perfect lens concept suggested by Pendry [9]. Sub-wavelength focusing through an LHM slab has been studied in [10, 11, 12]. Negative refraction of LHM has been verified in [8], and is again verified in this work. Reverse Cherenkov radiation also has been of interest [13].

As with traditional materials, constitutive parameters are relevant only in the case that the wavelength is much longer than the periodicity of the materials structure. Effective media theory has proven useful in describing LHM for frequencies near the resonance where negative values are expected and the periodicity is typically near $\lambda/5$. At significantly higher frequencies, however, the behavior is complicated by the inhomogeneities of the metamaterial that become visible to the wave.

1.1 Overview of the Work

The Center for Electromagnetic Theory and Applications (CETA) at the Massachusetts Institute of Technology has been studying LHM for the past several years, primarily in a theoretical capacity, but recently has had rising interest in the demonstration of of these materials through measurements. As the field matures, in turn more interest lies in the applications of metamaterials to real world problems. It is in this context that the work for this thesis has emerged.

Through its relationship with MIT Lincoln Laboratory, CETA's first endeavors into LHM manufacturing and measurement were in the form of a metamaterial antenna design [14]. For this work several LHM designs have been constructed for measurements by both Lincoln Laboratory and CETA's sister group at Zhejiang University in Zhejiang Province, China.

Chapter 2 introduces the dispersion relationship of the LHM studied and the method of determining the angle of refraction at an LHM interface. The metamaterial samples are characterized by effective parameters and transmission measurements are conducted to compare with the predicted behavior.

In chapter 3 measurements are conducted to verify the dispersion relationship predicted for several LHM materials. Results for a prism refraction experiment are presented along with a brief discussion on measuring the index of refraction from a beam shifting experiment. The inversion of critical predicted for certain anisotropic metamaterials is also measured and discussed.

Chapters 4 and 5 introduce a four-port device designed to separate an incidence signal into three transmission bands. The device utilizes a LHM prism to achieve spatial separation of the bands. Because of the dispersive nature of LHM, the refraction angle and transmitted power level varies with frequency. Ports are placed to collect negatively refracted power, positively refracted power, and the power reflected from the prism. Chapter 4 introduces the concept of the device and presents a verification measurement while chapter 5 gives a detailed study for complex metamaterials with one, two, or three dispersive parameters.

This thesis presents measurements conducted on these materials to observe a number of theoretically predicted properties of LHM. Classic measurements similar to those done in [8] are done to verify the presence of negative constitutive values. Right-handed materials such at Teflon and Plexiglas are used for comparison. Several new measurements are conducted to verify the dispersion relationships of LHM. Their results are also presented and discussed.

In chapter 6, a left-handed metamaterial is used as a substrate for a microstrip line. The LHM substrate consists of split-ring resonators that are shown to create

a negative permeability in one direction. The performance of an open circuit stub, stop band filter is shown to be enhanced when the LHM substrate is used.

A summary and conclusions are given in chapter 7. References follow. Appendix A gives a brief introduction to microwave measurement theory and presents the verification measurements used to test the measurement equipment. Appendix B lists the equipment used for the work. Additional appendices present mathematical details.

1.2 New Contributions

Several of the results presented in this thesis have not yet been reported in the literature. The new contributions found in this thesis are referred to below.

- Section 3.3 discusses the inversion of critical angle. A transmission experiment using an LHM slab where the inversion of critical angle is expected is measured and the results are compared to theory. The measurements show the LHM slab behaves like a medium where the inversion of critical angle is expected [15].

- The four-port device introduced in chapter 4 uses a metamaterial prism as a filter. Measurements of the device demonstrate this application of metamaterials [16].

- In chapter 5 the four-port device is refined and investigated analytically. The analysis demonstrates the performance potential of the device for various metamaterial configurations [17].

- The use of LHM as a microstrip substrate is demonstrated in chapter 6. Treatment of the LHM substrate as a homogeneous material with parameters found from retrieval [18] is shown to be consistent with measurements. The substrate is used to enhance the performance of a microstrip filter design [19].

Chapter 2

Left-Handed Metamaterials

Left-handed metamaterials exhibit many different properties than are found in normal materials. This difference results from the positive and negative values in the tensors $\bar{\bar{\epsilon}}$ and $\bar{\bar{\mu}}$ as well as the dispersive nature of LHM. This in turn affects the dispersion relationship which can vary both in shape and behavior over a small frequency range.

In this chapter the refraction laws pertinent to metamaterials are introduced. The models used to describe the frequency dependent permittivity and permeability are also given. The metamaterials available for measurements are introduced and the constitutive parameters are calculated directly from the simulated transmission properties of the structure. The transmission properties are compared with experimental measurements.

2.1 Dispersion and Negative Refraction

Metamaterials are constructed by the periodic inclusion of metallizations in an insulating material. Properly designed, these inclusions result in effective media parameters that have negative values for some frequencies. The most common form of inclusion is a split-ring resonator (SRR), to achieve negative permeability; and a metallic rod, to achieve negative permittivity. An example structure is shown in Fig. 2-1.

From this picture is it is clear that the metamaterial structure is not isotropic.

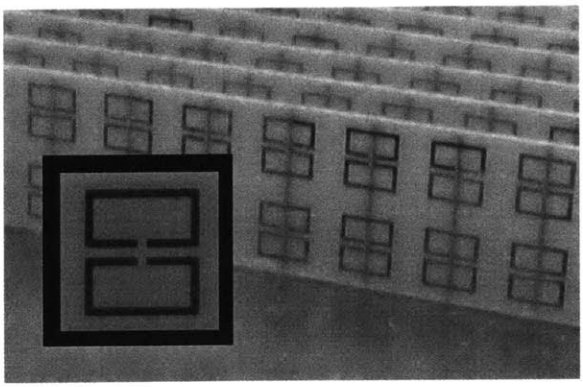

Figure 2-1: Metamaterial Sample with Symmetric SRR and Rod (photo).

The SRRs and the rods have an orientation and are not symmetric. The dispersive permeability and permittivity resulting from their presence are direction dependent. This being the case we expect the constitutive parameters to be in tensor form. In this thesis we are only concerned with anisotropic metamaterials whose permittivity and permeability are diagonalizable. We write the permittivity and permeability tensors respectively as

$$\overline{\overline{\epsilon}} = \begin{bmatrix} \epsilon_x(\omega) & 0 & 0 \\ 0 & \epsilon_y(\omega) & 0 \\ 0 & 0 & \epsilon_z(\omega) \end{bmatrix} \epsilon_o \tag{2.1}$$

$$\overline{\overline{\mu}} = \begin{bmatrix} \mu_x(\omega) & 0 & 0 \\ 0 & \mu_y(\omega) & 0 \\ 0 & 0 & \mu_z(\omega) \end{bmatrix} \mu_o. \tag{2.2}$$

ϵ_o and μ_o represent the freespace permittivity and permeability and ω represents the radial frequency. These equations draw attention to the fact that a metamaterial, in general behaves differently depending on the orientation and frequency of the wave within the material.

Many of the experiments in this work are conducted in a parallel plate waveguide (PPW) operating in its fundamental mode. A wave is incident upon the metamaterial from air. If the plate separation is in the $\hat{y}$ direction the polarization of the wave is

known and the incident wave can be written as

$$\bar{E}(\bar{r}) = \hat{y} E_o e^{i\bar{k}\cdot\bar{r}}, \tag{2.3}$$

where $\bar{k}$ is the wave vector, and $\bar{r}$ is the position vector. The reference $e^{-i\omega t}$ is assumed here and throughout the thesis. The wave inside the metamaterial is also of this form since the wave must travel in free space prior to reaching the metamaterial. The free space wave is limited to the TEM propagation mode by virtue of the plate separation and excitation frequencies. This condition is met for all frequencies where the wavelength, λ, is less than twice the plate spacing. This condition is needed to prevent the propagation of higher order modes which complicate the anaylsis. The phase matching property will insure that the k_y is also zero inside the metamaterial.

From Maxwell's equations, equation 2.3, and the requirement that $\bar{k} = \hat{x}k_x + \hat{z}k_z$, we find a relationship between $\bar{k}$, $\bar{\bar{\epsilon}}$, and $\bar{\bar{\mu}}$. This dispersion relationship is given in equation 2.4. A derivation is given in appendix C.

$$k_z^2 = \frac{\omega^2}{c^2}\mu_x(\omega)\epsilon_y(\omega) - \frac{\mu_x(\omega)}{\mu_z(\omega)}k_x^2 \tag{2.4}$$

It is important to note that only $\{\epsilon_y, \mu_x, \mu_z\}$ are relevant. The remaining parameters, $\{\epsilon_x, \epsilon_z, \mu_y\}$ are not needed to characterize the field for this configuration. Equation 2.4 may describe elliptical and hyperbolic curves in the (k_x, k_z) plane.

Equation 2.4 and the frequency dependent parameters can be used to determine the direction of group velocity inside a medium. The group velocity as a function of $\bar{k}$ is defined

$$\bar{v}_g \equiv \nabla_k \omega(\bar{k}). \tag{2.5}$$

As discussed in [20, 21], the group velocity is normal to the dispersion curve at the point of the present $\bar{k}$ vector. Since there are two normal directions, the remaining ambiguity can be resolved by selecting the side to which a curve of slightly greater frequency lies. This choice requires models of the dispersive constitutive parameters

as they change with frequency. It has been shown in [20] that for low loss materials, the constitutive parameters must have a positive derivative, provided a derivative can be defined.

It is now possible to predict the angle of refraction of a wave incident on a metamaterial. Consider two media with a boundary along the $\hat{x}$ axis as shown in figure 2-2. A wave is incident from the first medium onto the second medium. Any mismatch at the interface will result in a reflected wave. The transmitted power will be refracted either positively or negatively at the boundary. If the $\hat{x}$ components of the incident and transmitted group velocity are of the same sign the the refraction is positive. If the signs are opposite the refraction is negative. The behavior of refracted and reflected wave depends on the two mediums, their physical orientation at the boundary if anisotropic, and the incident wave.

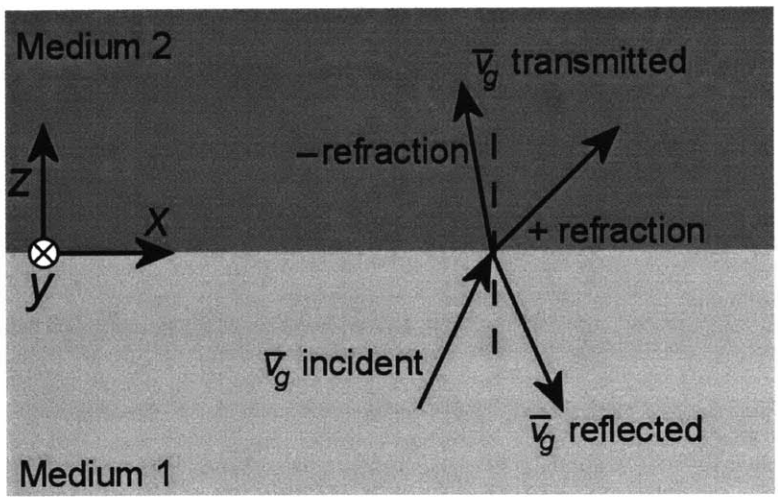

Figure 2-2: Transmission and reflection between two media.

Consider the case where medium 1 is a right-handed, isotropic medium, and medium 2 is a metamaterial with its $\hat{x}$ axis aligned with the the material interface. The characteristics of the dispersion curve and refraction, first summarized in [21] are given in table 2.1 as a function of the sign of the constitutive parameters $\{\epsilon_y, \mu_x, \mu_z\}$.

Figure 2-3 illustrates the reflection and refraction for the cases listed in table 2.1 when the relative parameters are normalized to k_o, and selected as ± 1. In the figure the corresponding cases from table 2.1 are labelled with roman numerals. The solid

Table 2.1: Refraction properties for anisotropic materials.

Case	ϵ_y	μ_x	μ_z	Shape	Refraction
i	+	+	+	elliptical	positive
ii	+	+	−	z^*-hyperbolic	negative
iii	+	−	+	x-hyperbolic	positive
iv	+	−	−	imaginary	
v	−	+	+	imaginary	
vi	−	+	−	x-hyperbolic	negative
vii	−	−	+	z-hyperbolic	positive
viii	−	−	−	elliptical	negative

* *Indicates the axis on which the foci lie.*

lines indicate the real solutions of the dispersion relation, and the dotted lines indicate the imaginary solutions. The black arrows indicate the negative refraction, and the gray arrows indicate positive refraction. Both the wave vector, $\bar{k}$, and the group velocity, $\bar{v}_g$, are shown. The smaller arrow head indicates the $\bar{k}$ vector.

Inspecting figure 2-3, it is interesting to classify the behavior. Figure 2-3(a) is perhaps the most familiar. It occurs when all three constitutive parameters are the same sign as in cases *i* and *viii*. The general case is an ellipse when μ_x and μ_z are not equal. For small k_x the wave transmits into the medium. At some critical angle, when the incident k_x exceeds $\sqrt{\epsilon_y \mu_z}$, the wave cannot be phase matched into the second medium. This is called the *cutoff* case.

In contrast to this, figure 2-3(c) shows the case where k_x must be large enough to support a transmitting wave. This occurs if μ_x is of opposite sign of ϵ_y, and μ_z as in cases *iii* and *vi*. A wave at normal incidence is completely reflected, while an obliquely incident wave may be transmitted. This is referred to as the *anti-cutoff* case.

Figure 2-3(b) is seen to be always transmitting and k_z is always real. Any incident wave can be transmitted into the medium. This occurs when μ_z is of opposite sign of ϵ_y, and μ_x as in cases *ii* and *vii*. This is referred to as the *never cutoff* case.

Finally when ϵ_y is the opposite sign of μ_x and μ_z, k_z is always imaginary in the second medium and a wave cannot propagate (cases *iv* and *v*) as is shown in figure 2-3(d). At these frequencies the materials are *always cutoff*.

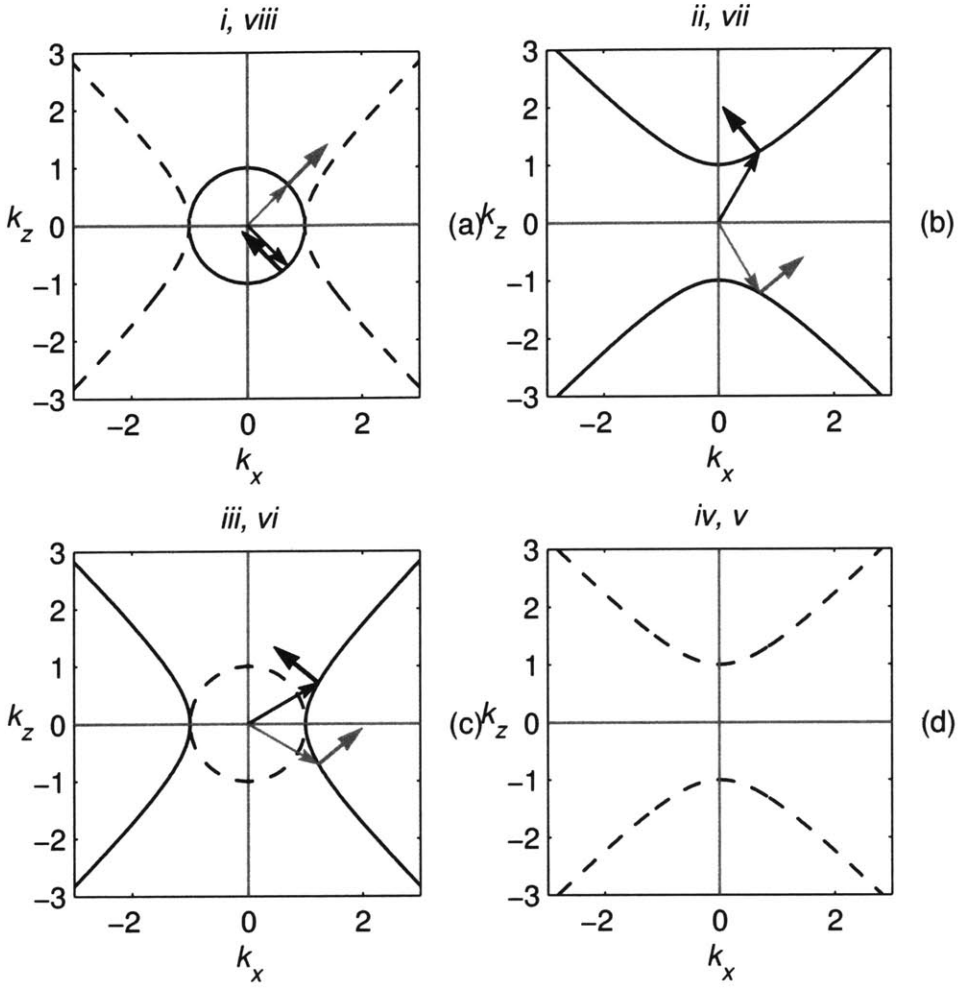

Figure 2-3: Dispersion curves for anisotropic metamaterials. The solid curves are the real part, and the dashed portion are the imaginary part. The arrows originating at the origin and having the smaller arrow heads are the $\bar{k}$ vectors. The larger arrow heads indicate the direction of $\bar{v}_g$. The black arrows indicate the cases where the refraction is negative, and the gray arrows indicate the cases where the refraction is positive. The subplots represent the cases presented in table 2.1, (a) cutoff, (b) never cutoff, (c) anti-cutoff, and (d) always cutoff.

Of course the boundary of the material does not have to correspond to the $\hat{x}$ or $\hat{y}$ principle axis of the material. If the physical boundary is askew with the principle axis the dispersion curves are rotated accordingly. The same principles of phase matching and group velocity are used to determine the transmitted wave vector and group velocity from the dispersion relationship. When the material has been rotated it is possible to have negative refraction even if all parameters are positive. In this

case, however, the sign of refraction depends on the incident angle.

2.1.1 Dispersive Models

The metallic inclusions that produce negative values of permeability and permittivity are directional and dispersive. The frequency band where metamaterials take negative values is a narrow band or low pass effect. In order to design the metallizations, the proposed structure is generally simulated as a two port device in an electromagnetic wave simulator. The S-parameters are then used to compute the constitutive parameters using an inversion technique called parameter retrieval [18].

In this work we use analytic models to desicribe the shape of the dispersive components of the permeability and permittivity. The frequency dispersive permeability found in some metamterials is in good agreement with the Lorentz model for dispersive media [4].

$$\mu = 1 - \frac{f_{mp}^2 - f_{mo}^2}{f^2 - f_{mo}^2 + i\gamma_m f/2\pi} \tag{2.6}$$

The parameters f_{mo} and f_{mp} represent the magnetic resonance and magnetic plasma frequency of the material. The plasma frequency must be larger than the resonance. These parameters can easily be extracted from the parameter retrieval. If a lossy model is to be used to describe the medium, the magnetic damping factor γ_m is taken to be non-zero.

When a component of the permittivity of a metamaterial medium is dispersive, the Drude model is used to estimate the values. The Drude model is simply a special case of the Lorentz model in which the resonance frequency is zero,

$$\epsilon = \epsilon_{bg}\left(1 - \frac{f_{ep}^2}{f^2 + i\gamma_e f/2\pi}\right). \tag{2.7}$$

The parameters are the electric plasma frequency, f_{ep}, and the electric damping factor, γ_e.

Figure 2-4 gives an example of the shape of the permeability and permittivity curves for a hypothetical metamaterial. The permeability is characterized by $f_{mo} =$

8 GHz, $f_{mp} = 8.5$ GHz, and $\gamma_m = 0$. The permittivity is characterized by $f_{ep} = 9$ GHz and $\gamma_e = 0$ with a background material $\epsilon_{bg} = 3$. If these were homogenous material parameters and valid in all material directions, the regions where the parameters are of opposite signs would not support propagating waves, while the regions of same sign would support right and left-handed propagation for, positive and negative valued regions respectively.

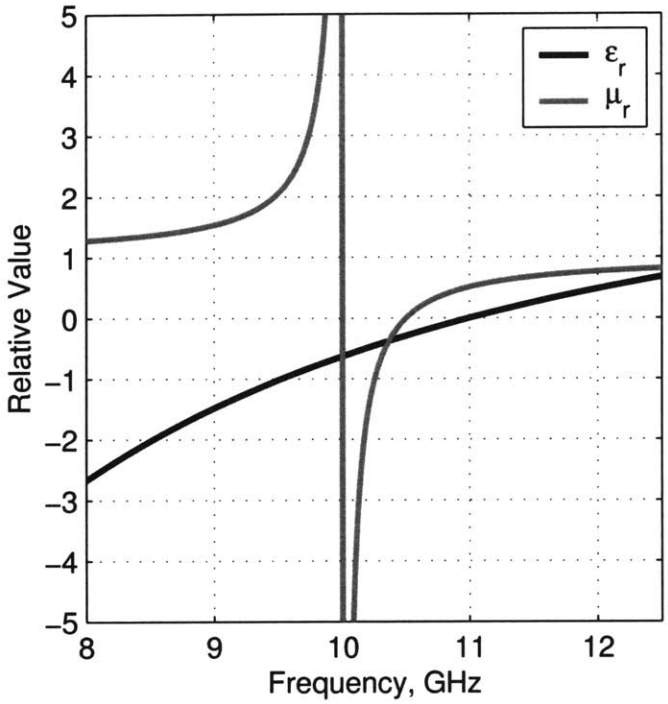

Figure 2-4: Examples of dispersive permeability and permittivity. The chosen parameters for μ are $f_{mo} = 8$ GHz, $f_{mp} = 8.5$ GHz, and $\gamma_m = 0$. ϵ is characterized by $f_{ep} = 9$ GHz and $\gamma_e = 0$ with a background material $\epsilon_{bg} = 3$.

The Drude and Lorentz shapes are typically only applied for frequencies a few gigahertz above the plasma frequencies. This is because the effective media approximation is not valid at high high frequencies. Retrieval generally shows behavior deviating from the models for frequencies well beyond the plasma frequency. Some caution is thus needed in using equations 2.6 and 2.7.

For a given metallic structure, if the background medium surrounding the structure changes, the location of the resonance and plasma frequencies shift. Above the

plasma frequency the permittivity asymtptotically approaches the background permittivity. This is implemented by including the term ϵ_{bg} in the Drude model equation 2.7. While aberrant behavior is expected high above the plasma frequency, the inclusion of ϵ_{bg} is important since it is affects the permittivity at all frequencies.

2.2 Metamaterials

Several different types of metamaterials were used for measurements in this thesis. In this section we present the structures, give the retrieved constitutive parameters, and compare the measured transmitted power through a slab of the material with the predicted transmission in some cases.

For each material the unit cell structure was simulated as a two port device using the commercial software package CST Microwave Studio. Perfect electrical conductor (PEC) and perfect magnetic conductor (PMC) boundary conditions are used as appropriate to simulate a slab of the metamaterial with infinite extent in the directions perpendicular to the propagation direction.

2.2.1 Constitutive Parameter Retrieval

In order to convert the predicted S-parameters into complex values of permittivity and permeability, the retrieval method presented in [18] is used. The S-parameters and the thickness of the simulated slab are needed for the retrieval process.

2.2.2 Transmission Measurements

Measurements of the material are conducted in a parallel plate waveguide setup shown in figure 2-5. The transmitter is positioned at one end of a 15 inch channel supported by microwave absorbing material. The device under test (DUT) is positioned inside the channel, typically directly in front of the receiver. Measurements are made at X-band frequencies.

For each material two orientations are measured corresponding to the $\hat{x}$ and $\hat{z}$

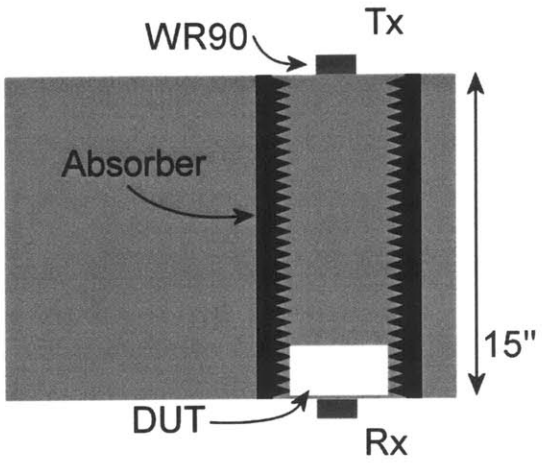

Figure 2-5: LHM transmission measurement setup inside a PPW with top plate removed. The DUT is placed inside an absorber padded PPW. A WR90 transmitter and receiver are used to measure the transmission.

directions of the unit cell structure. Each material required slightly different accommodations because of its size and difficulty to achieve the desired effect. Adjustments to the channel width, DUT position, and pressure on the top plate were made as necessary.

The system has apparent losses that are not entirely due to the heating of lossy metamaterials. Across the measurement channel, much of the energy enters the absorbers or passes out of the waveguide but not into the rectangular waveguide coupler. The transmitted power also suffers because the input coupler is mismatched with the parallel plates resulting in an S_{11} measurement of approximately -10 dB for the air filled waveguide. As a basis of comparison, measurements of an open channel are included in each figure to indicate the the attenuation due to the metamaterial itself.

2.2.3 Symmetric Split-Ring Resonator

The symmetric split-ring resonator (SSRR) was originally proposed by Pendry [22]. The design was customized by Weijen Wang in her masters thesis [14, 23]. It is her design that was manufactured by Lincoln Laboratory and is used for these measurements. The design is given in figure 2-6 and the parameters are given in table 2.2. A

photo of the manufactured strip is given in figure 2-7. The substrate the metallic rings are etched on has a relative permittivity of approximately 4. The region in front of and behind the ring and substrate is filled with the background material. We explore changes in both the thickness, h, and permittivity of the background material.

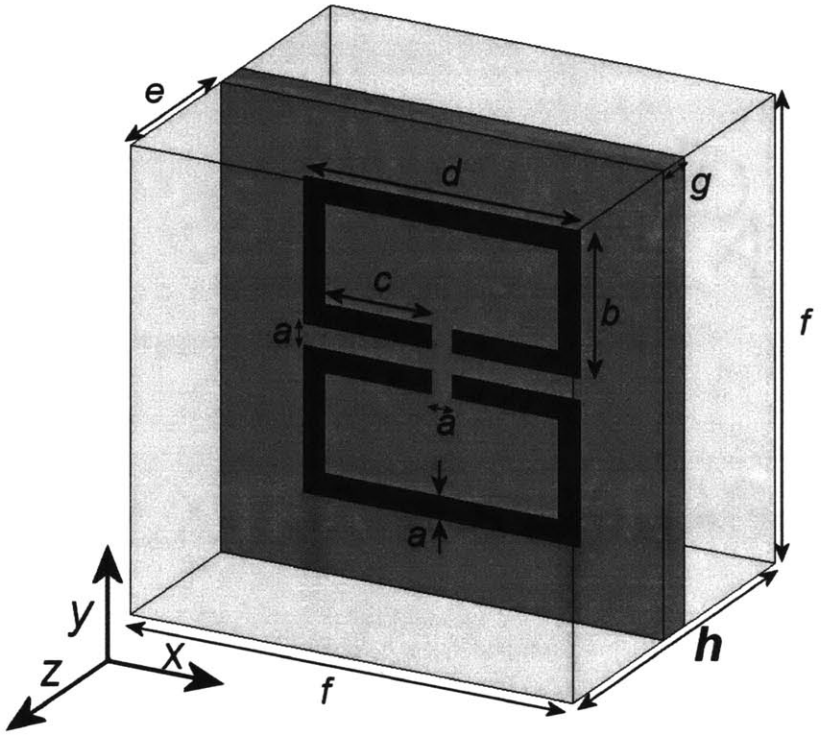

Figure 2-6: Symmetric SRR design schematic.

Table 2.2: Symmetric SRR dimensions of Fig. 2-6.

Label	a	b	c	d	e	f	g	h
Value (mm)	0.24	1.25	1.20	3.12	2.25	5.00	0.50	5.00

Retrieval Results for the SSRR Structure

The retrieval results with a background material of air are shown in figure 2-8. In order to characterize the media two incidents are used. When the wave is incident in the $\hat{x}$ direction the retrieval results is for ϵ_y and μ_z. For this incidence the magnetic field couples with the split-rings giving a dispersive permeability. The rings also have

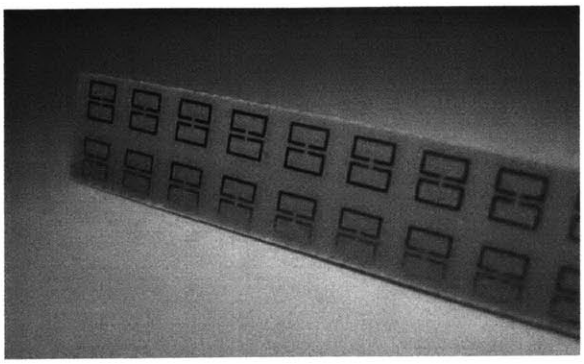

Figure 2-7: Symmetric SRR strip (photo).

an an effect on the permittivity which away from resonance is approximately 1.64 before the resonance, and 1.95 after the resonance. The retrieved permeability is seen to very closely follow the Lorentz model when the resonance and plasma frequencies of $f_{mo} = 10.08$ GHz and $f_{mp} = 10.56$ GHz respectively are used. The region where the imaginary part of the permeability becomes significantly negative is suppressed because the retrieval results are felt to be unreliable in this region, just above the resonance frequency.

When the incidence is in the $\hat{z}$ direction ϵ_y and μ_x are retrieved. The permittivity is very nearly a constant value of 1.2 while the permeability, which is not shown for clarity, is very near 1.0.

Beyond simply noting the reasonably good fit of the Lorentz model, we also drawn attention to the discrepancy between the two retrievals of ϵ_y. The discrepancy in values for ϵ_y is attributed to the high dielectric PCB card that the ring is printed on. Additional simulations have shown that if the background dielectric is completely homogeneous, the agreement between the retrieved value for the $\hat{x}$ and $\hat{z}$ incidences is much better. In order to treat this as an effective medium, ϵ_y must be single valued for a given frequency. To use effective medium theory, an approximation must be made. In the design examples given later in the thesis we assume that the permittivity is simply that of the background material and is not affected by the PCB card.

There are two parameters that can be easily varied experimentally for the SRR, namely the spacing between cards and the background material. As can be seen from

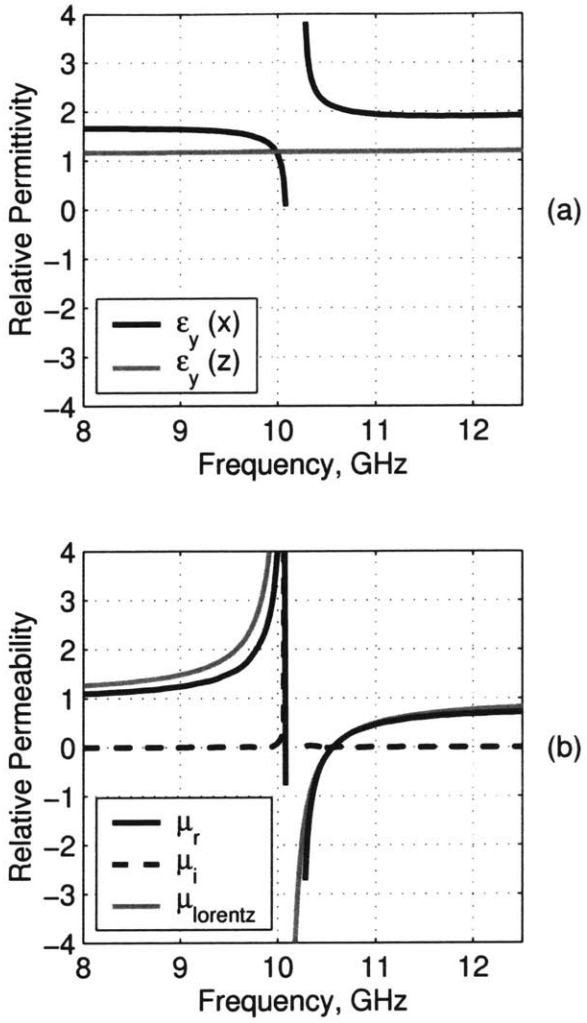

Figure 2-8: Symmetric SRR retrieval for propagation in the $\hat{x}$ and $\hat{z}$ directions with $\epsilon_{bg} = 1$. (a) Retrieved permittivity. (b) Retrieved permeability ($\mu_x \approx 1$ not shown).

figure 2-7, the rings are printed on strips that can be spaced arbitrarily next to each other. The value of h is changed by varying the tickness of the spacer. The spacing between adjacent strips can be filled with a material other than air.

To test the effect of varying the ring separation, spacings of 3 mm and 10 mm are simulated and compared to the original spacing of 5 mm. Air is used as the background material. The real part of the permittivity and permeability are shown in figure 2-9. The retrieval for the reference distance of 5 mm is also included. The spacing has minimal effect on the plasma frequency, however, the resonance frequency is lower for smaller spacing. The effect the SSRR has on the retrieved permittivity is

also significantly stronger when the spacing is reduced.

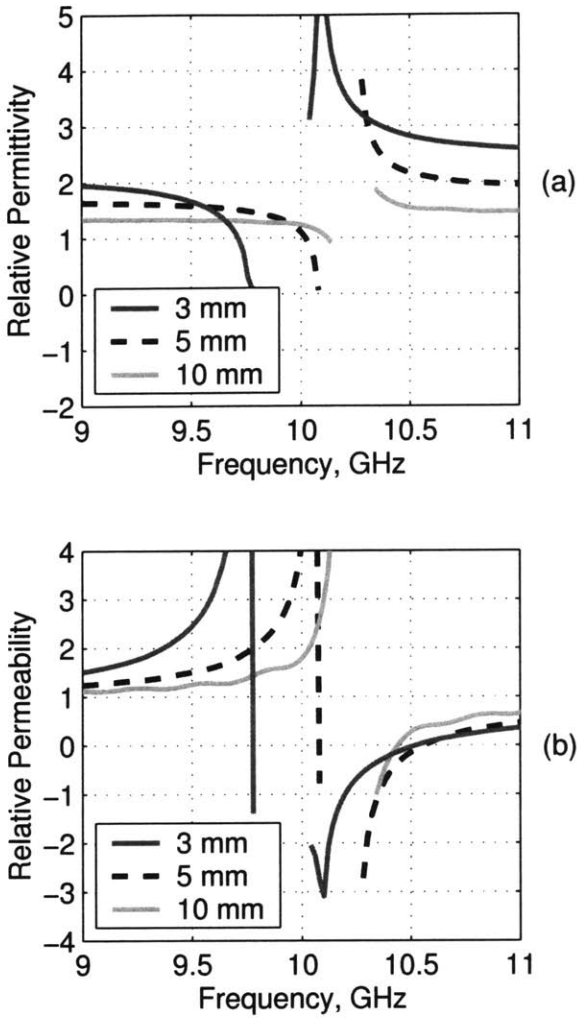

Figure 2-9: Spacing study for SSRR. (a) Permittivity. (b) Permeability.

To test the effect of changing the background material, ϵ_{bg} is simulated with values of 2 and 3. The results are shown in figure 2-10. The reference card spacing of 5 mm is maintained. Increasing the dielectric constant reduces the wavelength inside the dielectric making the metal rings effectively larger. The resonance and plasma frequencies are both shifted down in frequency. The difference between the two frequencies remains approximately constant. Table 2.3 summarizes the retrieval results.

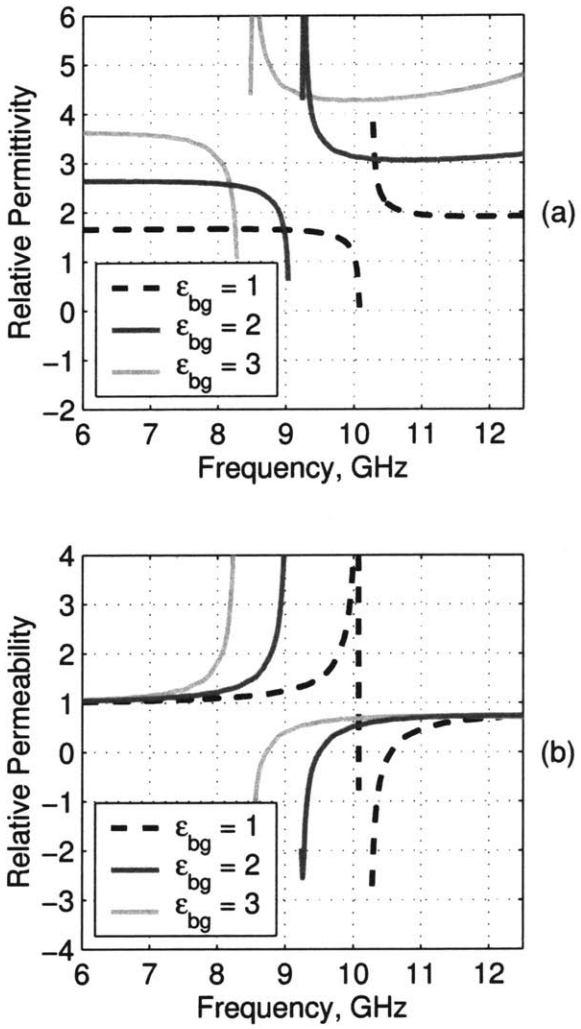

Figure 2-10: Background permittivity study for SSRR. (a) Permittivity. (b) Permeability.

Table 2.3: SSRR retrieval results summary.

Spacing (mm)	Background	f_{mo} (GHz)	f_{mp} (GHz)	Negative BW (MHz)
5	1	10.08	10.56	480
3	1	9.78	10.52	740
10	1	10.20	10.44	240
5	2	9.06	9.51	450
5	3	8.30	8.73	430

Symmetric SRR Measurements

We now use the retrieval results to predict the transmitted power through a slab of the SSRR metamaterial. The predicted results are compared with the transmission (S_{21}) measured experimentally. Measurements are taken for air and Teflon background materials.

The SSRR with air background is 9 cm long in the $\hat{x}$ direction. Figure 2-11 shows the measurements and simulation results for this material in addition to the air measurements for comparison. Only the simulation for transmission in the $\hat{x}$ direction is shown.

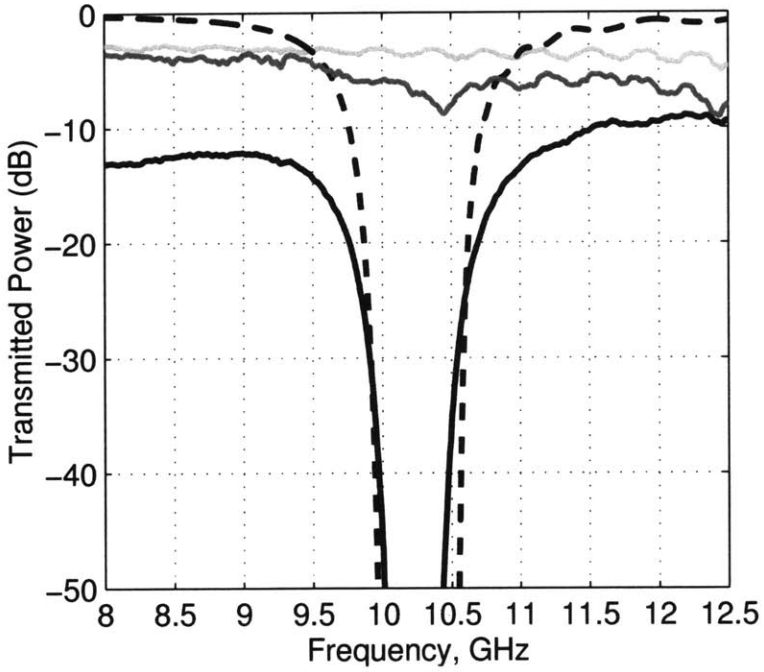

Figure 2-11: SSRR with air background for $\hat{x}$ and $\hat{z}$ orientations. *Solid Black*– $\hat{x}$ Measurements. *Solid Dark Gray*– $\hat{z}$ Measurements. *Dashed Black*– $\hat{x}$ Simulation. *Solid Light Gray*– Air baseline.

The theoretical results are calculated by using the Lorentz model for permeability based on the retrieved resonance and plasma frequencies found in table 2.3 (f_{mo} = 10.08 GHz, f_{mp} = 10.56 GHz). In order to account for losses present in measurement, the loss term was set to γ_m = 0.4 GHz. The magnetic damping factor primarily affects the roll off into and out of the stop band. With γ_m = 0, there is no roll

off and the transition between stop and pass band is practically instantaneous. The sample thickness also affects the stop band width when losses are introduced. The permittivity was set to $\epsilon_y = 1.64$ corresponding with the low frequency value from retrieval.

In figure 2-12 the measured transmission is shown when Teflon is used in the background material. The Teflon strips used to separate the PCB cards is a quarter inch thick (6.35 mm). Simulation results for this configuration give resonance and plasma frequencies of 9.16 GHz and 9.47 GHz respectively. The predicted stop band is noticeably lower than the measured stop band in this case. This discrepancy could come from the fact that the air gaps between the top plate and Teflon may be significant. Nevertheless, the measurements show clearly that the effect of the background dielectric is to lower the stop band by about 500 MHz.

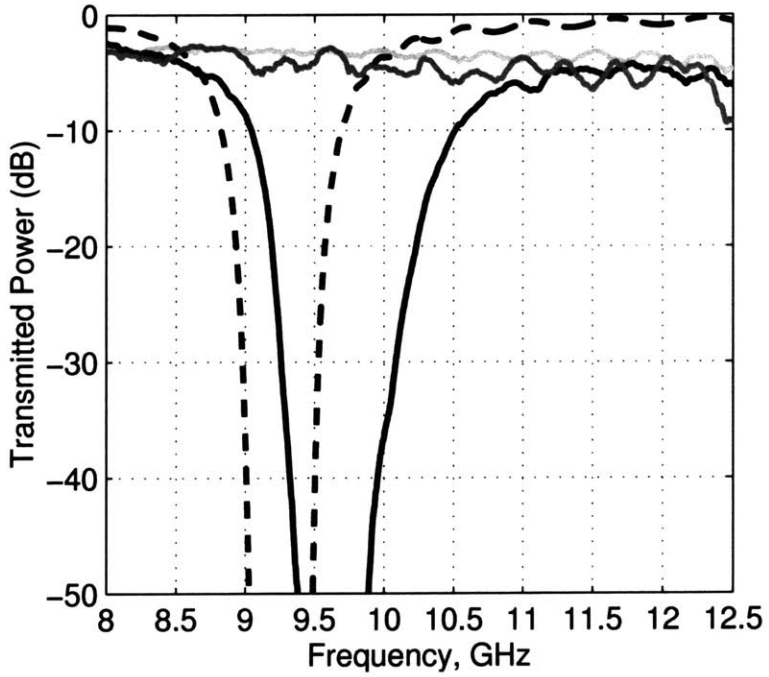

Figure 2-12: SSRR with Teflon background for $\hat{x}$ and $\hat{z}$ orientations. *Solid Black*– $\hat{x}$ Measurements. *Solid Dark Gray*– $\hat{z}$ Measurements. *Dashed Black*– $\hat{x}$ Simulation. *Solid Light Gray*– Air baseline.

2.2.4 Symmetric Split-Ring Resonator with Rod

The addition of a rod to the SSRR on the opposite side of the printed circuit board results in a plasmatic permittivity in addition to the resonant permeability. The rod is centered on the reverse side of the printed circuit board and extends from the top to the bottom in the $\hat{y}$ direction. The unit cell structure is shown in figure 2-13. The dimensions of the cell are the same as those in table 2.2. The rod is continuous from cell to cell, and is assumed to have perfect electrical contact with the plates of the waveguide. The primary technical challenge with structure is achieving good electrical contact with the waveguide plates. The behavior or the structure is also considered when a small gap is present between the plates and the rods.

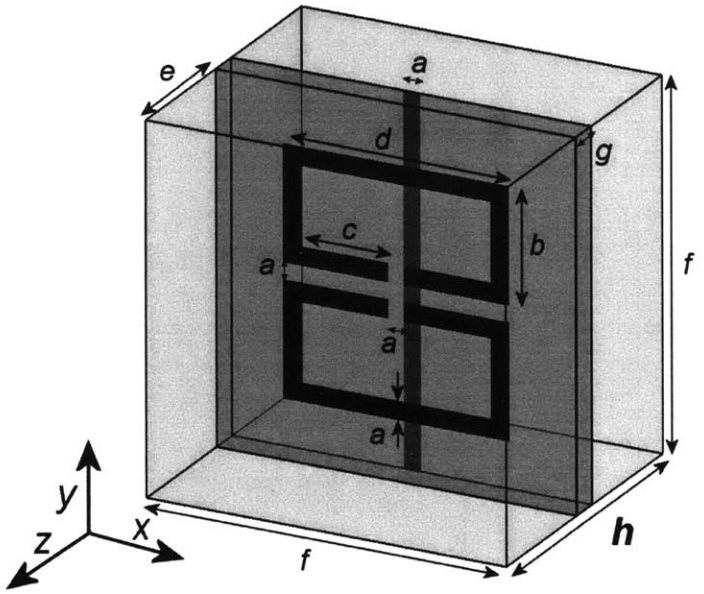

Figure 2-13: Symmetric SRR design with rod.

Retrieval Results for the SSRR and Rod Structure

The retrieval in figure 2-14 shows the results when the background material is air and the card spacing is 5 mm for an $\hat{x}$ directed incidence. The Drude and Lorentz models have been used to fit the retrieval results. In order to better fit the retrieved permittivity the value of ϵ_{bg} is set to 1.64, the low frequency value of the permittivity

for the SSRR only case found in figure 2-8(a). From figure 2-14, there is clearly a region where both ϵ and μ are negative.

Retrieval results for incidence in the $\hat{z}$ direction are not shown in the figure but give a plasmatic permittivity with a plasma frequency very close to that $\hat{x}$ incidence result. The permeability, μ_x, is close to 1.

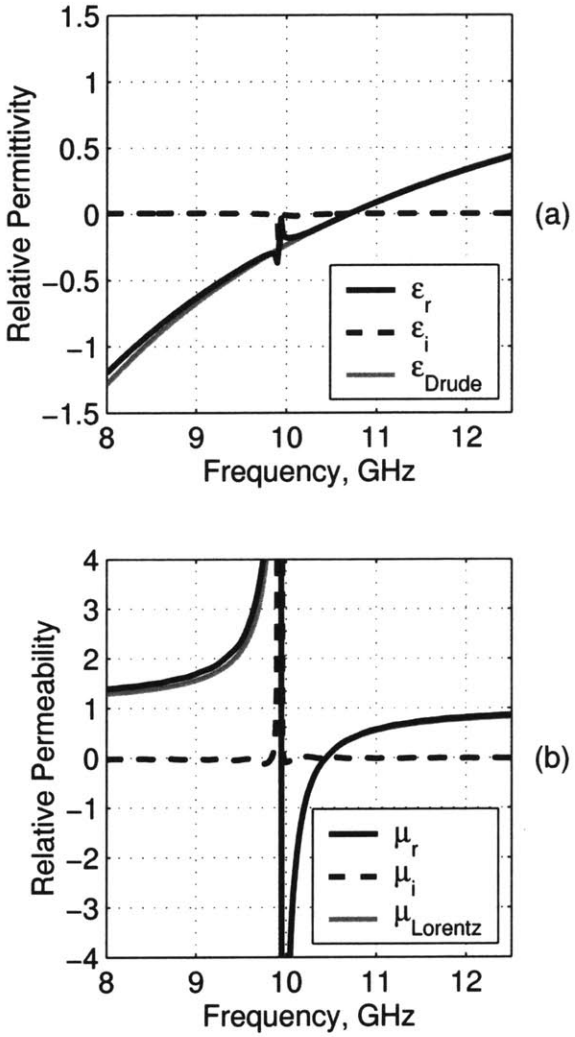

Figure 2-14: Symmetric SRR with rod retrieval with $\hat{x}$ directed incidence. $\epsilon_{bg} = 1$. (a) Permittivity. (b) Permeability.

Inserting a dielectric spacer between the printed cards can cause the dispersive properties to change as they did for the SSRR only case in the previous section. Here we consider a background medium with permittivity, $\epsilon_{bg} = 2$. The retrieval results

are shown in figure 2-15. The addition of the dielectric is seen to move the resonance and plasma frequencies down. The electric plasma frequency is moved below the magnetic resonance frequency so that no region of double negative behavior exists. The results are summarized in table 2.4; the results for $\epsilon_{bg} = 3$ are also given.

Introduction of a gap in between the rod and the plates can cause the permittivity to follow the Lorentz model more closely than it does the Drude model. Simulations show that a resonance is introduced and at low frequencies both constitutive parameters may be positive, resulting in a low frequency pass band.

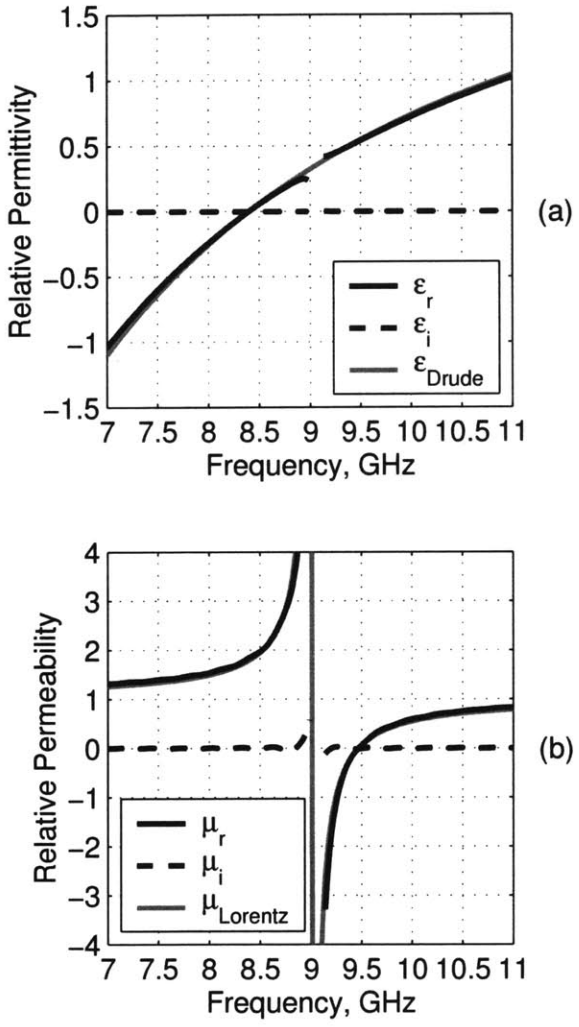

Figure 2-15: Symmetric SRR with rod retrieval, $\epsilon_{bg} = 2$. (a) Permittivity. (b) Permeability.

Table 2.4: SSRR with rod retrieval results summary.

Figure	ϵ_{bg}.	f_{mo}	f_{mp}	f_{ep}	Dbl. Neg. BW (MHz)
2-14	1	9.95	10.44	10.69	490
2-15	2	9.01	9.47	8.40	0
–	3	8.28	8.71	7.16	0

SSRR with Rod Measurements

The measurement of the SSRR structure with rod is complicated by the ambiguity of the nature of the electrical contact between the rod and the parallel plates for any given measurement. In order to improve contact and minimize the gap, pressure is generally applied to the top plate. Even this can yield varying results. The coveted feature of this measurement is the double negative bandwidth, or LH band. Further complicating matters is that the material tends to be very lossy in the LH region leading to significantly lower transmitted power than found in the double positive bandwidths.

Figure 2-16 shows the experimental transmission results for the SSRR with rod material. Low frequency transmission is seen for both the $\hat{x}$ and $\hat{z}$ incidences because of the imperfect contact between the rods and plates. The measurement does not go to high enough frequencies to view the high pass band. For the $\hat{x}$ incidence case the transmission peak is in the bandwidth where both ϵ_y and μ_z are negative. The measurement results are in very good agreement with the retrieval results. In the double negative bandwidth, where ϵ and μ are negative, the transmission is at least 10 dB higher when compared to the surrounding stop band.

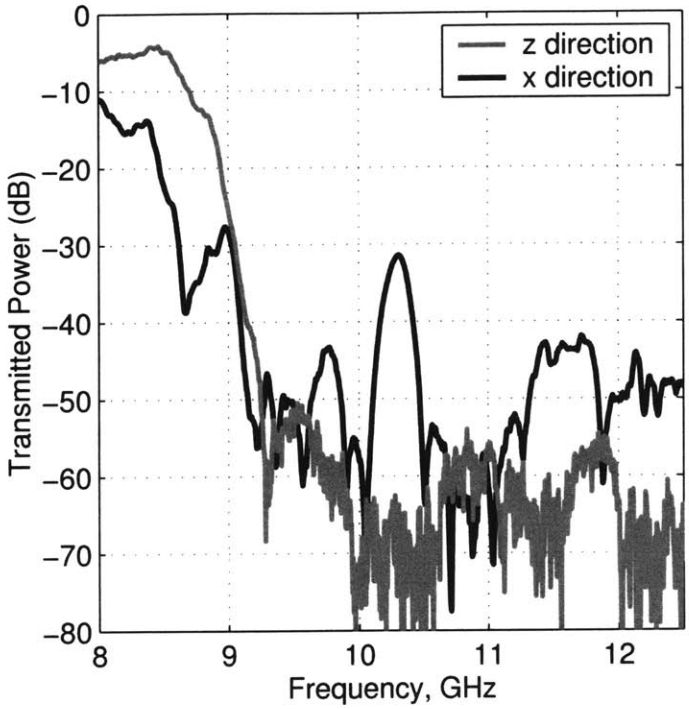

Figure 2-16: Symmetric SRR with rod transmission experiment in $\hat{x}$ and $\hat{z}$ directions. $\epsilon_{bg} = 1$.

2.2.5 Omega Ring Structure

The omega ring structure combines the ring and rod into a single metallization that is printed on both sides of the printed circuit board substrate [24, 25]. The Ω shaped structures are inverted rings such that the gaps are adjacent to the top of the opposing Ω. A unit cell is shown in figure 2-17 and a photo of the material is shown in 2-18. The omega structure available for measurement is a single solid block of material. This construction maximizes the homogeneity of the background material and improves passband transmission levels. While it lacks the flexibility of a strip based construction, the design is ideal for a transmission experiment where maximum transmission is desired in the left-handed bandwidth.

Table 2.5: Omega structure dimensions when referred to figure 2-17.

Label	a	b	c	d	e	f
Value (mm)	5.00	3.00	0.40	1.90	1.50	0.50

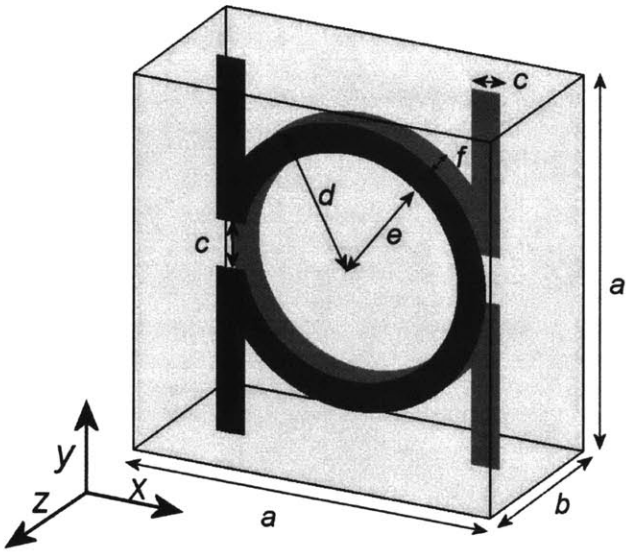

Figure 2-17: Omega Unit Cell schematic.

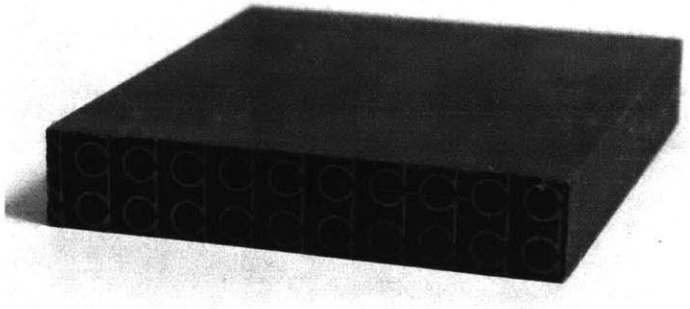

Figure 2-18: Omega Structure (photo).

Retrieval Results for the Omega Ring Structure

The background dielectric has an approximate relative permittivity of 2.65. The omega structure unit cell is simulated using a fine mesh to minimize the discretization effects of the ring. The retrieval results are shown in figure 2-19. From the figure it is evident that the Drude or Lorenz model does not fit the retrieval results as well as they do with the previous two structures. The permittivity has a positive second derivative above the apparent plasma frequency, and in fact resonates at higher frequency. The resonance frequency of the permeability is unclear as it it has asymptotes at both 7 GHz and 9 GHz. The zero crossing is 13.0 GHz but the small derivative near the plasma frequency may limit the accuracy of this value.

Omega Ring Structure Measurements

The omega ring measurement perhaps offers more insight into the material properties than the retrieval itself. We see a very strong transmission band above 10.5 GHz for both incidents in figure 2-20. The measurements are in good agreement with [26], where the same structure has been measured. For the $\hat{x}$ directed incidence we have a strong passband from about 8.2 to 9 GHz. This region has been suppressed in the retrieval results in figure 2-19, because the retrieval gives negative imaginary parts. Nevertheless, the trend of the retrieval results suggests that this may be a double negative bandwidth. The $\hat{z}$ directed incidence does not have this feature further suggesting that the orientation of the loop makes the passband possible. The high pass band suggests that the plasma frequency of the permeability is not as high as calculated by the retrieval. The slab measured has dimensions 5.2 cm by 9 cm in the $\hat{x}$ and $\hat{z}$ directions respectively.

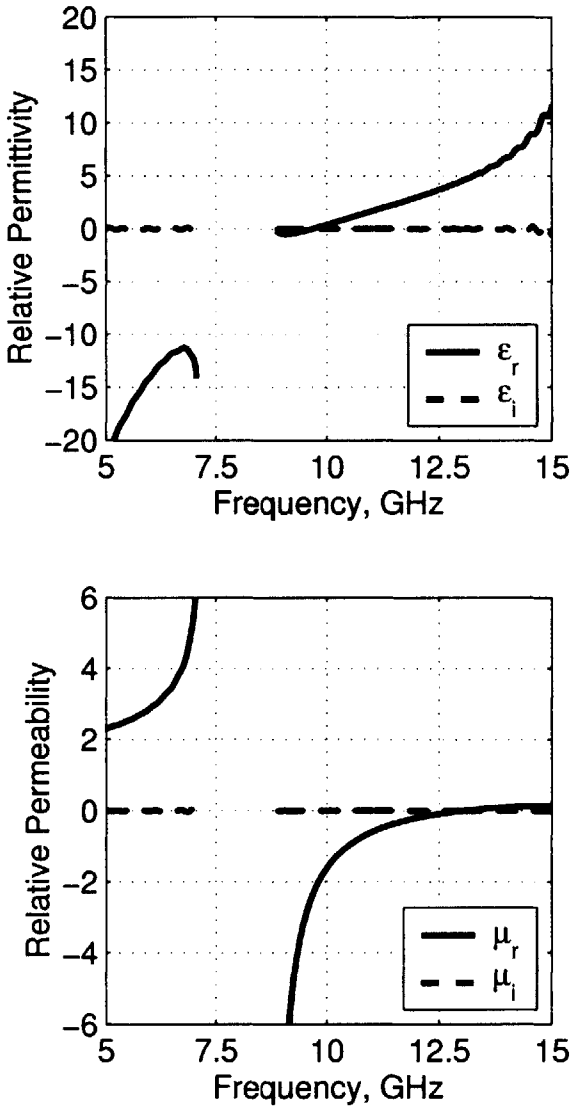

Figure 2-19: Omega structure retrieval results.

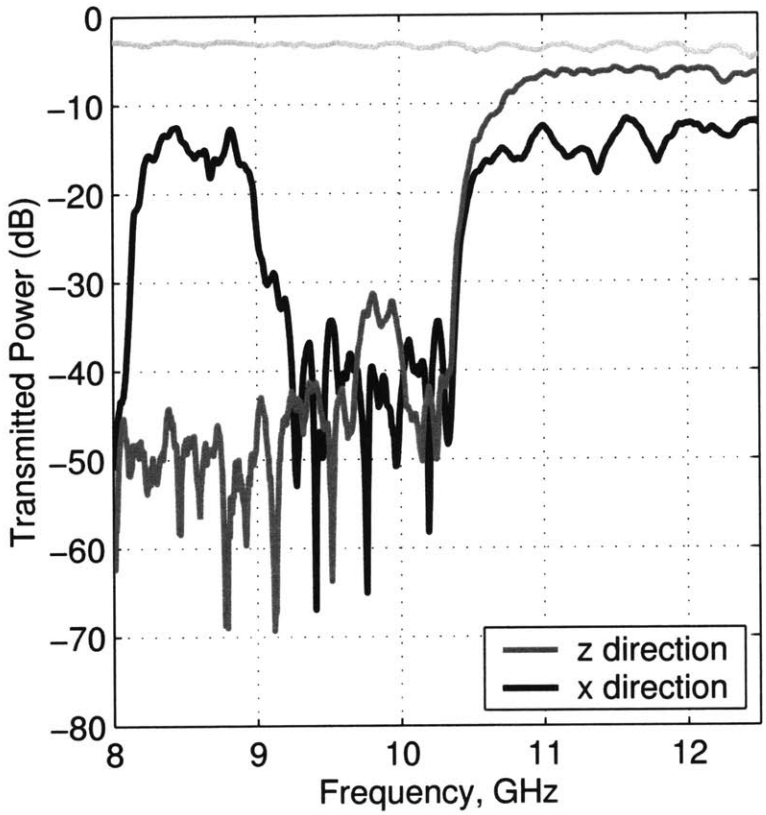

Figure 2-20: Omega structure transmission experiment in $\hat{x}$ and $\hat{z}$ directions.

2.2.6 S-Ring

The S-ring structure pictured in figure 2-21 is quite different from the first three metamaterials presented [27, 28, 29]. The "S" formations are connected, forming a continuous conductor. At the edge of the material a gap is left so that the S rings do not come in contact with the waveguide. This implies that the the S-ring unit cell structure depends on the height of the material and is always one cell "tall." Like the omega structure, the S-rings are flipped relative to each other on the front and back of each dielectric PCB.

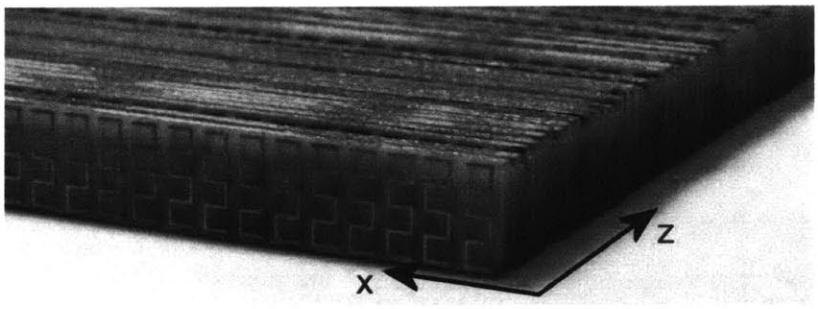

Figure 2-21: S-Ring Structure (photo).

S-Ring Measurements

The transmission experimental results in figure 2-22 show a passband in the frequency range from 9.7 GHz to 11.7 GHz. The experimental sample measured 10 cm by 10 cm. The attenuation of passband is significant because of the large sample thickness. A sample with smaller dimensions is expected to have a stronger passband transmission level.

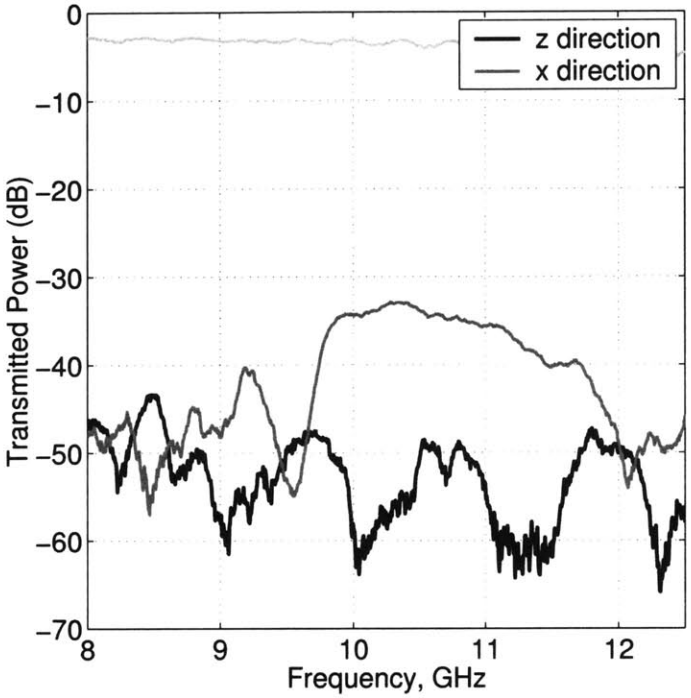

Figure 2-22: S-ring structure transmission experiment in $\hat{x}$ and $\hat{z}$ directions.

Chapter 3

Experimental Measurements

In this chapter we present several measurements that can be used to verify various properties of left-handed materials. The first two experiments are conducted to measure the effective index of refraction of a metamaterial. The prism and beam shifting methods have been attempted, however, only the prism experiment has yielded reliable results. The hyperbolic dispersion relationships and the inversion of critical angle expected for certain metamaterials is discussed and measured.

The power measurements presented in this chapter are calculated from the measured S-parameters. The reader is referred to appendix A where an introduction to the scattering matrix is given along with details of the experimental equipment used. The appendix also includes the measurement results for a preliminary verification exercise conducted to measure the permittivity of air, Teflon and Plexiglas.

3.1 Metamaterial Prism Experiment

In appendix A the received phase from a prism experiment is used to calculate the permittivity of air, Teflon, and Plexiglas. By measuring the phase progression along the baseline in 3-1 the index of refraction can be found using Snell's law. A similar experiment has been attempted using a left-handed material, however, the phase progression is not steady enough to achieve a good estimate.

In this section we use the amplitude of the transmission to determine the angle

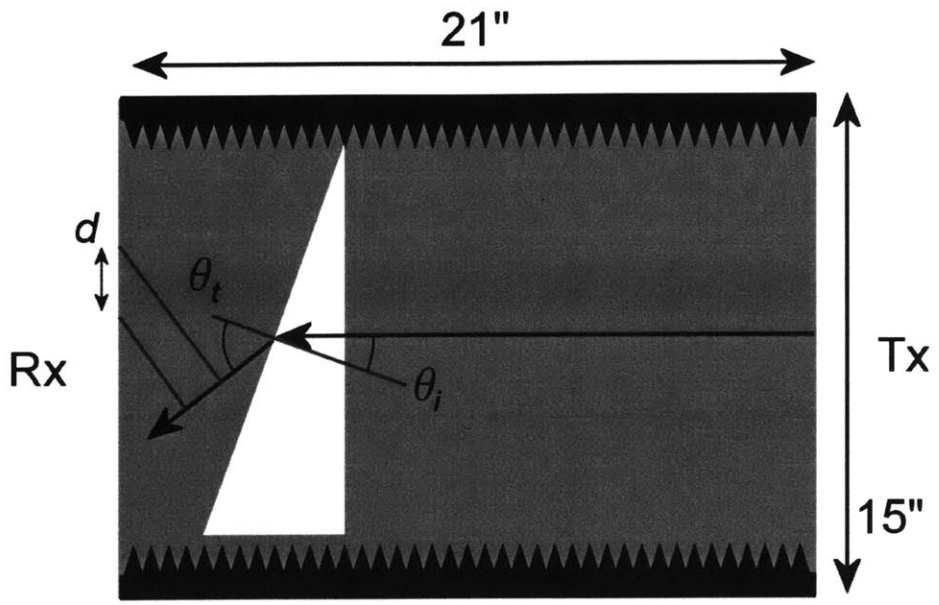

Figure 3-1: Schematic for a phase based retrieval measurement. Tx – transmitter. Rx – receiver.

of refraction through the prism. Two experimental setups are used, a circular plate waveguide and a rectangular plate waveguide. The schematics are shown in figure 3-2 and photographs of the experimental setups are shown in figure 3-3. Two different sizes of circular discs were used with diameters of 30 and 15 inches. The larger is photographed. We discuss the experimental results achieved with the rectangular and circular plates and compare the results with theoretical predictions. In both cases the index of refraction is estimated and compared with the theoretical results.

The LHM prism used for experimental measurements is in fact not an isotropic structure. Due to the incidence, however, the magnetic field is always in the $\hat{z}$ direction inside the metamaterial, and μ_x is never seen by the field. We compare the measured index of refraction with the index calculated from the retrieval results in section 2.2.4. Figure 3-4 gives a graphical interpretation of this phenomenon. The axis correspond to the orientation of the material shown in figure 2-13 which has been superimposed for reference. The wave in air has the $\bar{k}$ vector shown by the gray arrow. The wave enters the LHM slab normal to the boundary and becomes a backwards wave (lower black arrow). At the exit interface, the backwards wave is

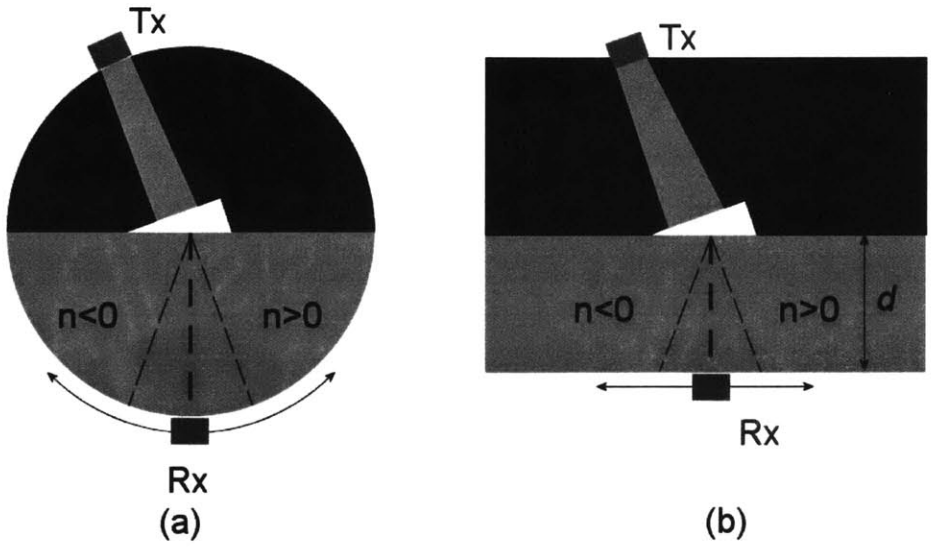

Figure 3-2: (a) Circular and (b) rectangular plate prism transmission experimental setup schematic. The thick dashed line indicates the refraction direction for a zero index material. The right and left hand side indicate positive and negative indexes, respectively. The thin dashed line indicates the direction of refraction from a ± 1 index prism. Tx – transmitter. Rx – receiver.

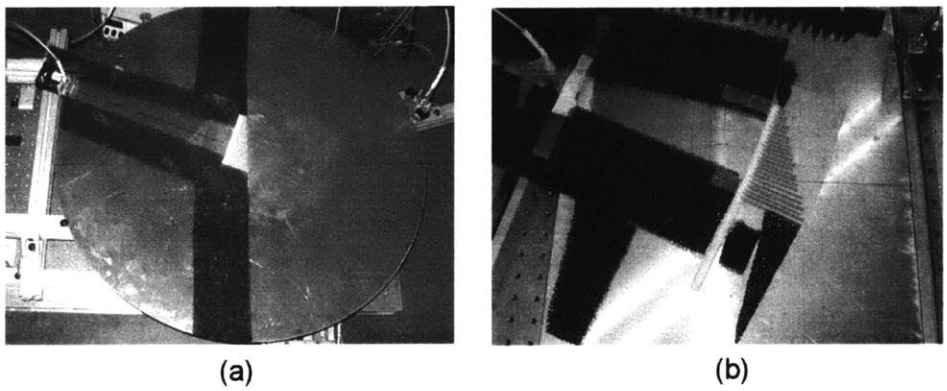

Figure 3-3: (a) Circular and (b) rectangular plate prism transmission experimental setup. (photo)

phase matched to air yielding negative refraction.

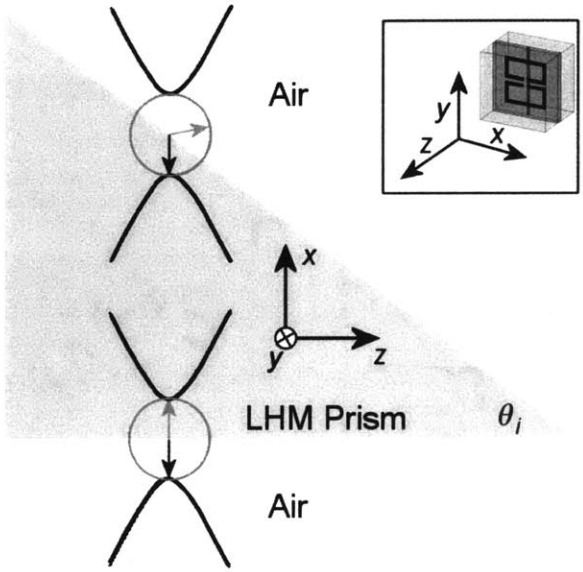

Figure 3-4: Demonstration of phase matching in an LHM prism composed of SSRRs and rods. The gray and black arrows represents the $\hat{k}$ vectors in air, and the LHM respectively. The unit cell of the SSRR and rod metamaterial has been superimposed for reference.

3.1.1 Rectangular Plate Measurements

We use the rectangular plate setup shown in figure 3-2(b) to calculate the index of refraction from the prism as a function of frequency. The values follow directly from Snell's law and the geometry of the experimental setup.

A beam enters the parallel plates from the transmitting source, Tx, and travels down the channel entering the prism at normal incidence. At the second boundary of the prism, which is cut at an angle θ_i and is aligned with the baseline edge of the plates, the wave exits the prism and is refracted according to Snell's law. The receiver, Rx, sweeps the baseline measuring the amplitude of the electromagnetic field over frequency and position.

The location of the center of power is at position x along the baseline, and is measured with respect to the center of the refracted power for a zero index prism.

The transmission angle is measured from the prism face normal is found to be

$$\theta_t = \arctan\left(\frac{x}{d}\right), \tag{3.1}$$

where d is the distance between the prism face and the baseline. The transmission angle can easily be converted into the effective index of refraction of the material by use of Snell's law.

$$n = \frac{\sin\theta_t}{\sin\theta_i} \tag{3.2}$$

The term *effective* index of refraction is used to refer to n above because the prism is not isotropic, however, the refraction is only dependent on ϵ_y and μ_z. The effective index is $n = \sqrt{\epsilon_y \mu_z}$.

If an air prism is used, $\theta_t = \theta_i$. In order for the above equations to predict the correct transmission angle we must properly calibrate the zero point of x so that it corresponds to the point of zero index of refraction. Calibration has been done using an air measurement where $n = 1$.

To detect a negative index of refraction, an LHM prism of symmetric split-ring resonators and rods is measured. The prism consists of cards with staggered length. A staircase approximation is used to avoid cutting the unit cell structure at any point. For this experiment a 2 to 1 step ratio is used giving a prism angle of $\theta_i = 26°$. Air, Teflon, and Plexiglas are measured for comparison.

The distance $d = 14$ cm is selected arbitrarily for measurements. The measurement is taken along the baseline by the receiver. The center of the beam is determined by finding the center of mass of the measured power. The measured frequency range is the X-band. Figure 3-5 shows the normalized power in dB through a SSRRs and rods prism. The position axis is such that a transmission at 0 cm corresponds to a material with zero index. Superimposed is a black line indicating the center of the beam for each frequency.

There is a frequency band from approximately 10 GHz to 10.5 GHz where the center of the beam is negative corresponding to a negative index of refraction.

In figure 3-6 the calculated index refraction is plotted for the LHM prism measure-

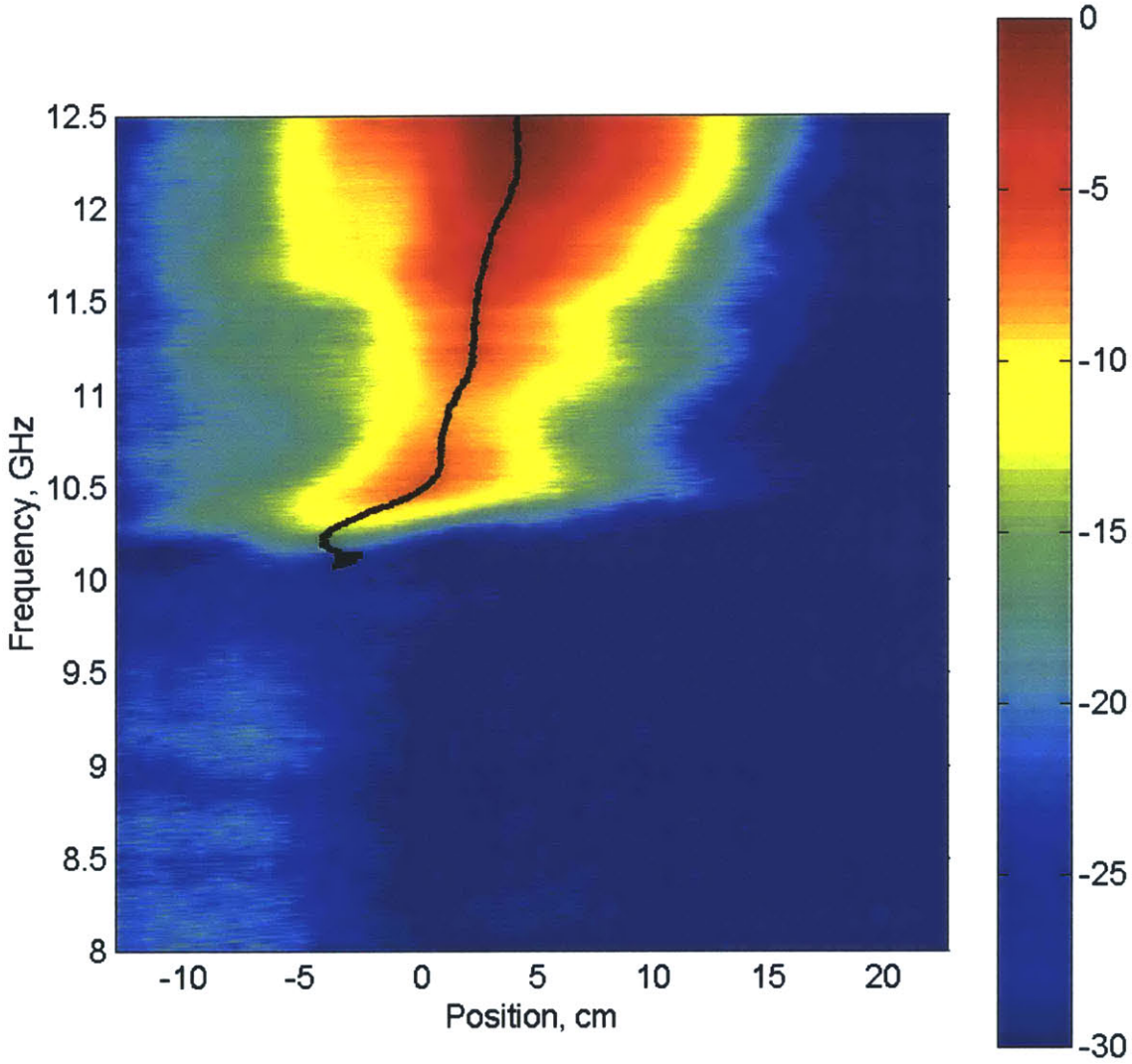

Figure 3-5: Normalized measured transmitted power in dB through the SSRRs and rods prism using the rectangular plate measurement setup. The center of power is indicated by the black line. (color)

ment and compared to the index calculated from the retrieval results. It is seen to be in very good agreement with the measurement results. Below about 10 GHz, the transmission is so low, the measured index of refraction is expected to be meaningless. This is in agreement with theory since we anticipate the permittivity to be negative while the permeability is positive resulting in an imaginary index of refraction. The index of refraction measured for air, Teflon and Plexiglas are also plotted.

The center of mass approach used here may result in bias due to the measurements having been taken over a finite extent of the baseline. Because the power is very low at the edges of the baseline, the bias is negligible.

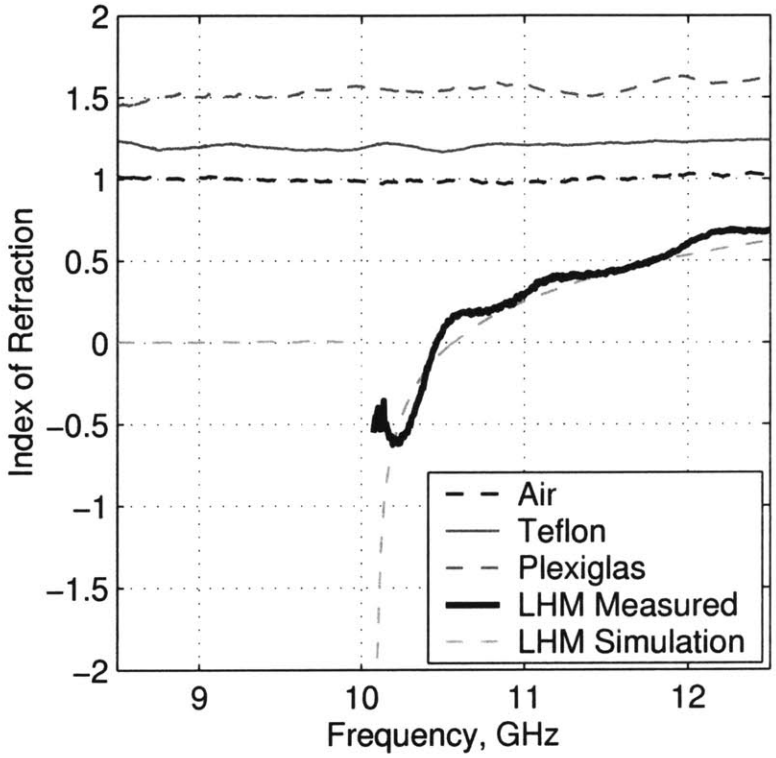

Figure 3-6: Experimentally measured index of refraction using rectangular plate setup.

3.1.2 Circular Plate Measurements

When circular plates are used, the calculation of the index of refraction, n, is simplified slightly since the transmission angle, θ_t, is measured directly. The measurements for

the SSRRs and rods prism is shown in figure 3-7. The center of power calculated using the center of mass method is shown in black. A 3 to 1 step ratio is used for the LHM prism. This corresponds to $\theta_i = 18.43°$.

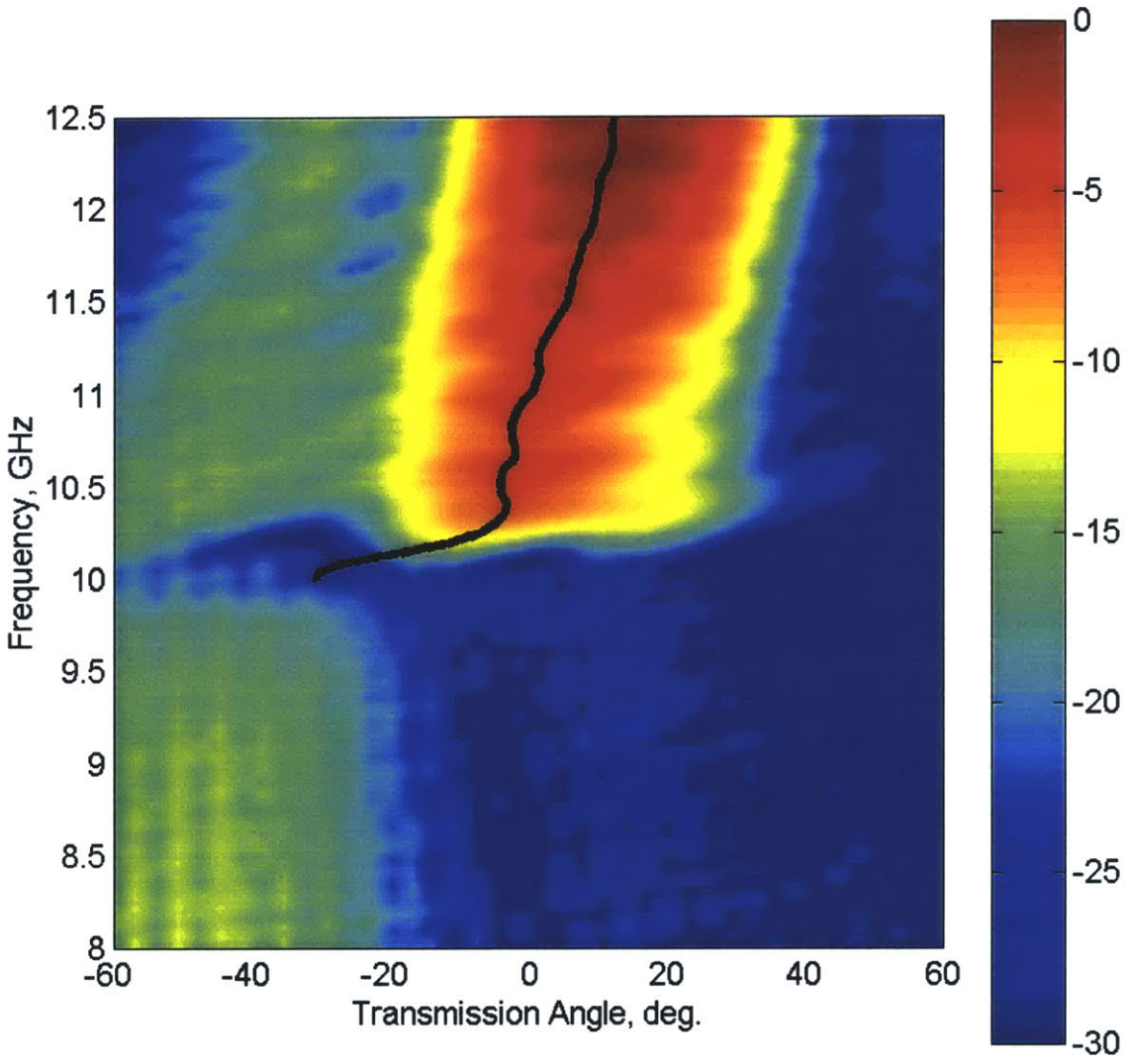

Figure 3-7: Normalized measured transmitted power in dB through the SSRR with rod prism using the circular plate measurement setup. The center of power is indicated by the black line. (color)

In both figures, for very negative positions and angles, there is an almost constant low power transmission. This is in fact due to the absorber and prism being thinnest in this direction.

The measured index of refraction is shown as a function of frequency in figure 3-8

along with measurements for air and Teflon. The retrieved results are compared to the theoretical results. We find the for indexes of refraction, $|n| > 0.5$, the agreement is good.

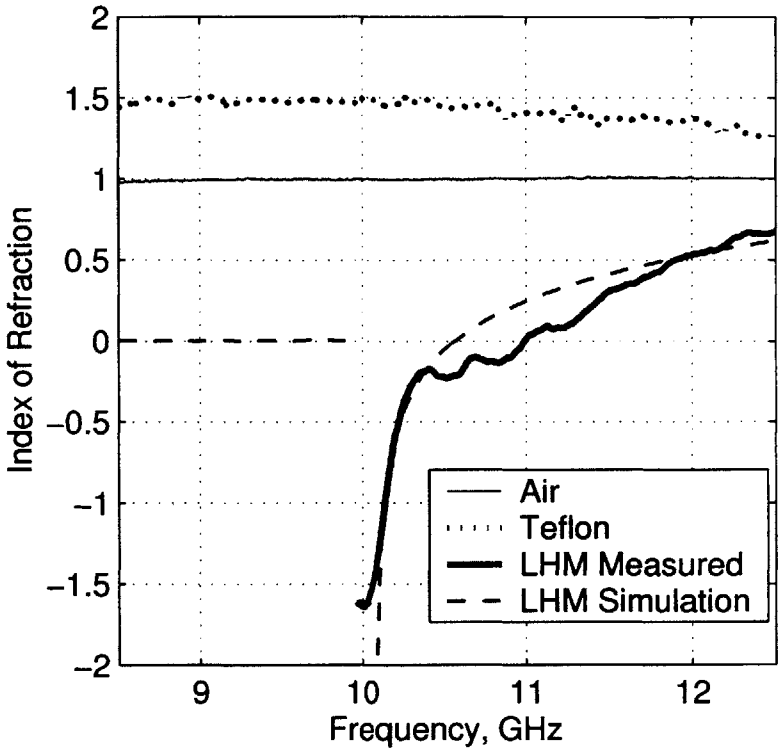

Figure 3-8: Measured index of refraction for SSRRs and rods, air, and Teflon prisms. The predicted index of refraction for the LHM prism is also shown.

3.2 Beam Shifting Experiment

The beam shift experiment can also be used to measure the index of refraction [30, 31]. The experimental setup is shown in figure 3-9. In this experiment a beam is incident onto a slab of thickness, d, at an angle θ_i is laterally shifted a distance x as a result of the different index of refraction of the slab, n. These values are labelled in figure 3-10.

The amount of lateral shift is used to determine the index of refraction.

$$w = x/\cos\theta_i \tag{3.3}$$

$$\theta_t = \arctan\left(\frac{w}{d}\right) \tag{3.4}$$

Once θ_t is found, equation 3.2 can be used to determine the index of refraction. Though arbitrary, here the choice has been made to have a 0 beam shift, represent the crossing point from a negative to positive effective index of refraction.

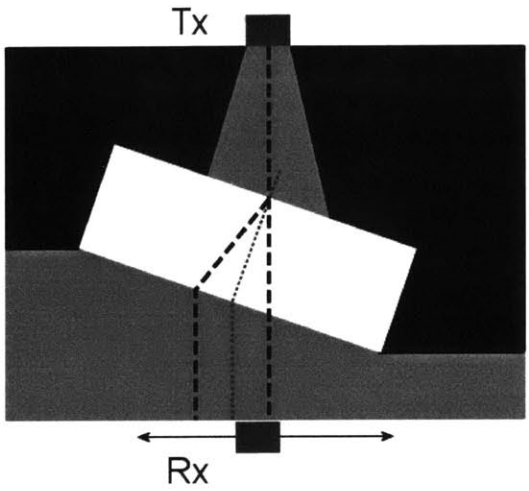

Figure 3-9: Schematic for the beam shift experiment. The gray base represents the bottom parallel plate. Black indicates absorbing material. The white rectangle represents the material to be measured. The beam shift is the lateral displacement of the beam due to refraction in the slab.

The larger the incidence and thicker the slab, the larger the beam shift for a given index. Large beam shifts require slabs of long lateral extent in order to prevent the length from affecting the results. On the other hand the index can change very rapidly requiring a very high sensitivity if a small incidence and slab thickness is used. The beam shift experiments are conducted experimentally on air, Teflon, Plexiglas, and the omega medium. We have found that for the samples available, realizable values of θ_i and d are insufficient to achieve a good beam shift measurements with the waveguide coupler which has an aperture of .9 in (2.28 cm).

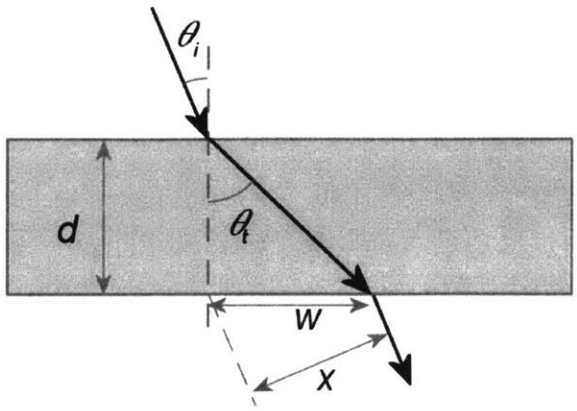

Figure 3-10: Beam shift conceptual drawing. A beam is incident at an angle, θ_i, and is refracted at an angle, θ_t, inside the prism. The beam exists at the angle θ_i. The lateral displacement of the beam, x, is the measured quantity.

For example the omega medium has a thickness of $d = 5.2$ cm. For $\theta_i = 20°$ the index has been calculated as a function of the beam shift and the analytical results are shown in figure 3-11. Noting that the width of the WR90 coupler, it is quite obvious that a greater sensitivity is needed than can be provided from this experimental setup. Even for the dielectric materials measured, calibrating the zero position has proven difficult. Small errors in position are magnified and have a dramatic effect on the measured value.

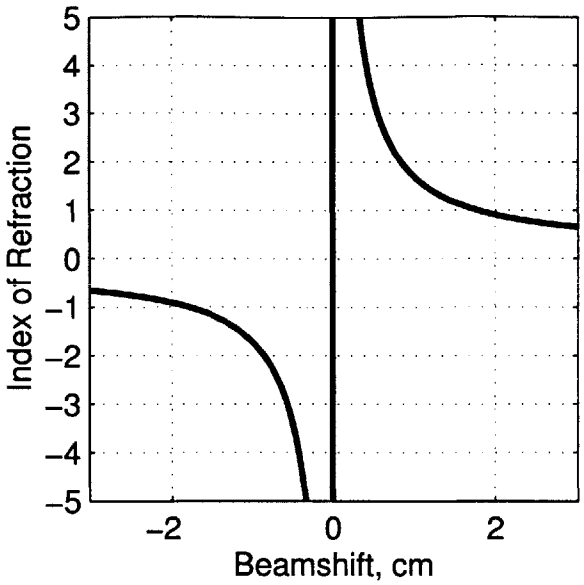

Figure 3-11: Index of refraction as a function of beam shift for $d = 5.2$ cm and $\theta_i = 20°$.

3.3 Critical Angle Study

In positive isotropic media the dispersion relationship is circular. At the interface between two such media there is an incidence angle at which phase matching from the denser medium to less dense medium is no longer possible. At incident angles greater than this critical angle, phase matching is not possible and total reflection results. Only evanescent waves transmit into the medium. In metamaterials the dispersion relationship may be hyperbolic, and the significance of the critical angle can in fact be inverted such that for incidence angles smaller than the critical angle phase matching is not possible. This case is referred to as anti-cutoff as was discussed in section 2.1.

For an interface such as in figure 2-2, where medium 1 is air, and medium 2 is an LHM oriented such that $\text{sign}(\epsilon_y) = \text{sign}(\mu_z) \neq \text{sign}(\mu_x)$, the inversion of critical angle is expected for a $\hat{y}$ polarized electric field incidence.

Using the values in table 2.4 for $\epsilon_{bg} = 1$ and the Drude and Lorentz models for permittivity and permeability, the transmission through a 3 cm thick anisotropic slab is calculated using the formulation presented in [32]. The LHM is assumed lossless.

The calculated results are shown in figure 3-12. In the band from f_{mo} to f_{mp}, where $\epsilon_y < 0$, $\mu_z < 0$, and $\mu_x = 1$, the anti-cutoff criteria are met. The power transmitted in this band increases with increasing incidence angle. This behavior is consistent with the inversion of critical angle. The slab has finite thickness, therefore, some power is transmitted by tunnelling even when phase matching is not possible at the first boundary. Above f_{ep}, all parameters are positive, and the dispersion relationship is elliptical.

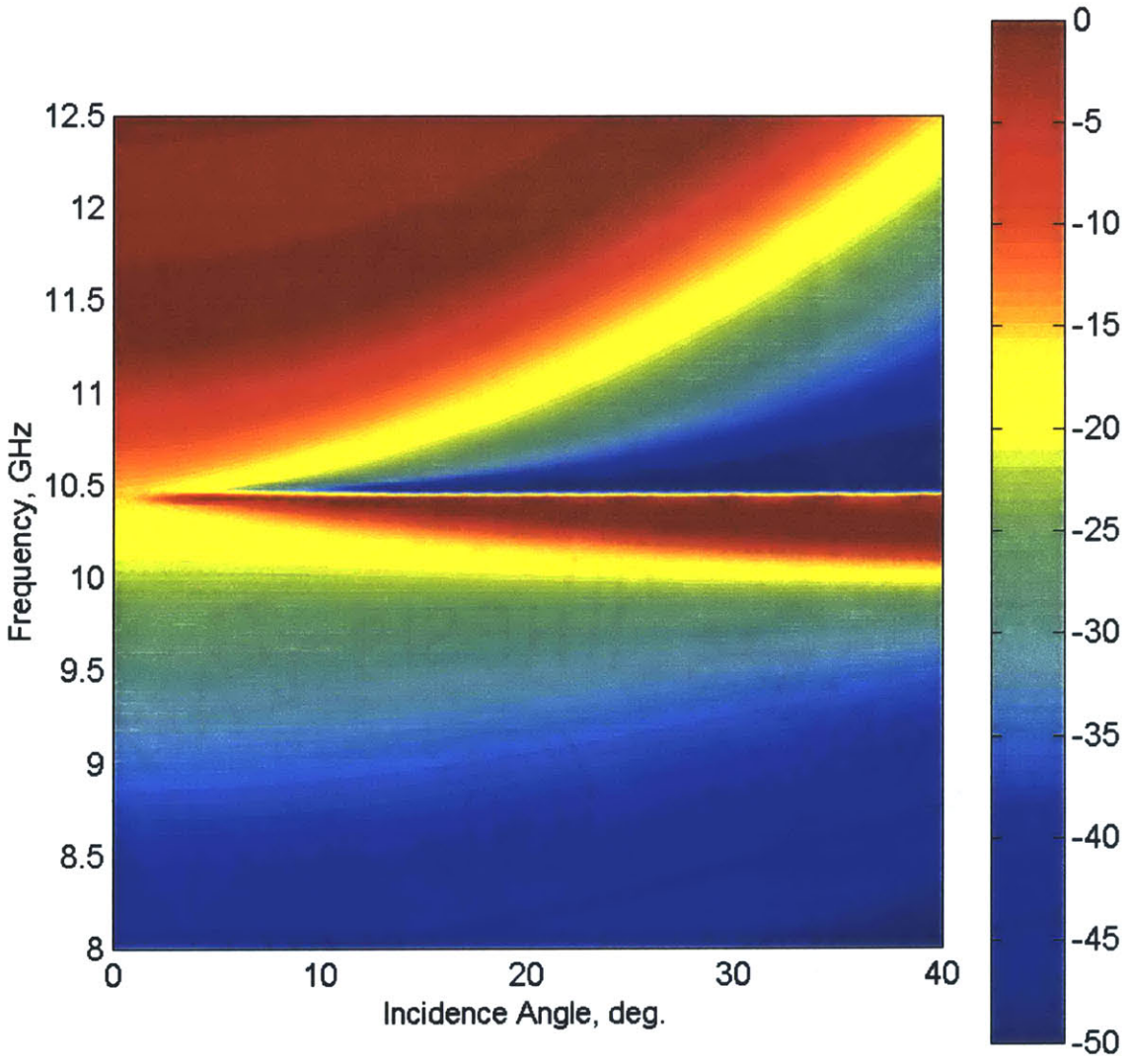

Figure 3-12: Theoretical transmitted power through a lossless 3 cm LHM slab. (color)

In order to measure this effect experimentally, setup in figure 3-13 is used. The

transmitter was moved in 5° increments from normal incidence to up to a 40° incidence angle. The receiver is scanned over a wide degree of angles and a portion of the results are averaged to give the transmitted power. Several experimental samples were measured primarily using the SSRRs and rods structure with various sample thicknesses and widths. In figure 3-14 the experimental measurement results are

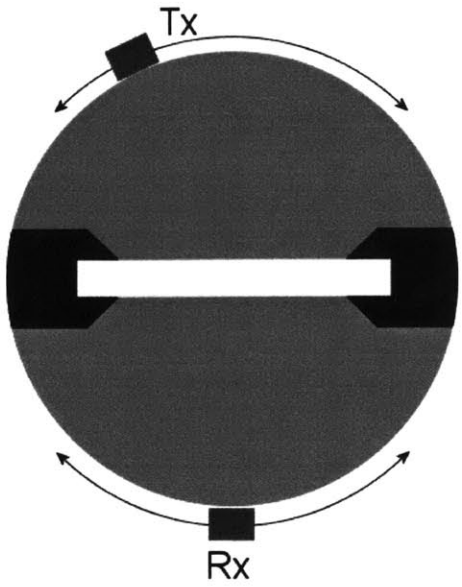

Figure 3-13: Schematic of transmission angle experiment. Tx – transmitter. Rx – receiver.

plotted showing the received transmitted power as a function of incidence angle and frequency. Reasonably good agreement is seen between the theoretical figure and the measured figure, however, the inversion of critical angle predicted is not visible. While both figures 3-12 and 3-14 have a passband from 10 GHz to 10.5 GHz, only the theoretical results show the transmitted power increasing consistently with angle. This is not visible from the measurement. This difference can be attributed to the significant losses of the realized material.

In order to verify that the Drude and Lorentz models reasonably describe the dispersive permittivity and permeability of the slab, losses are introduced, and the theoretical results are recalculated and shown in figure 3-15. The similarity increases substantially. In order to witness the predicted inversion of critical angle, an LHM

with significantly lower losses is needed.

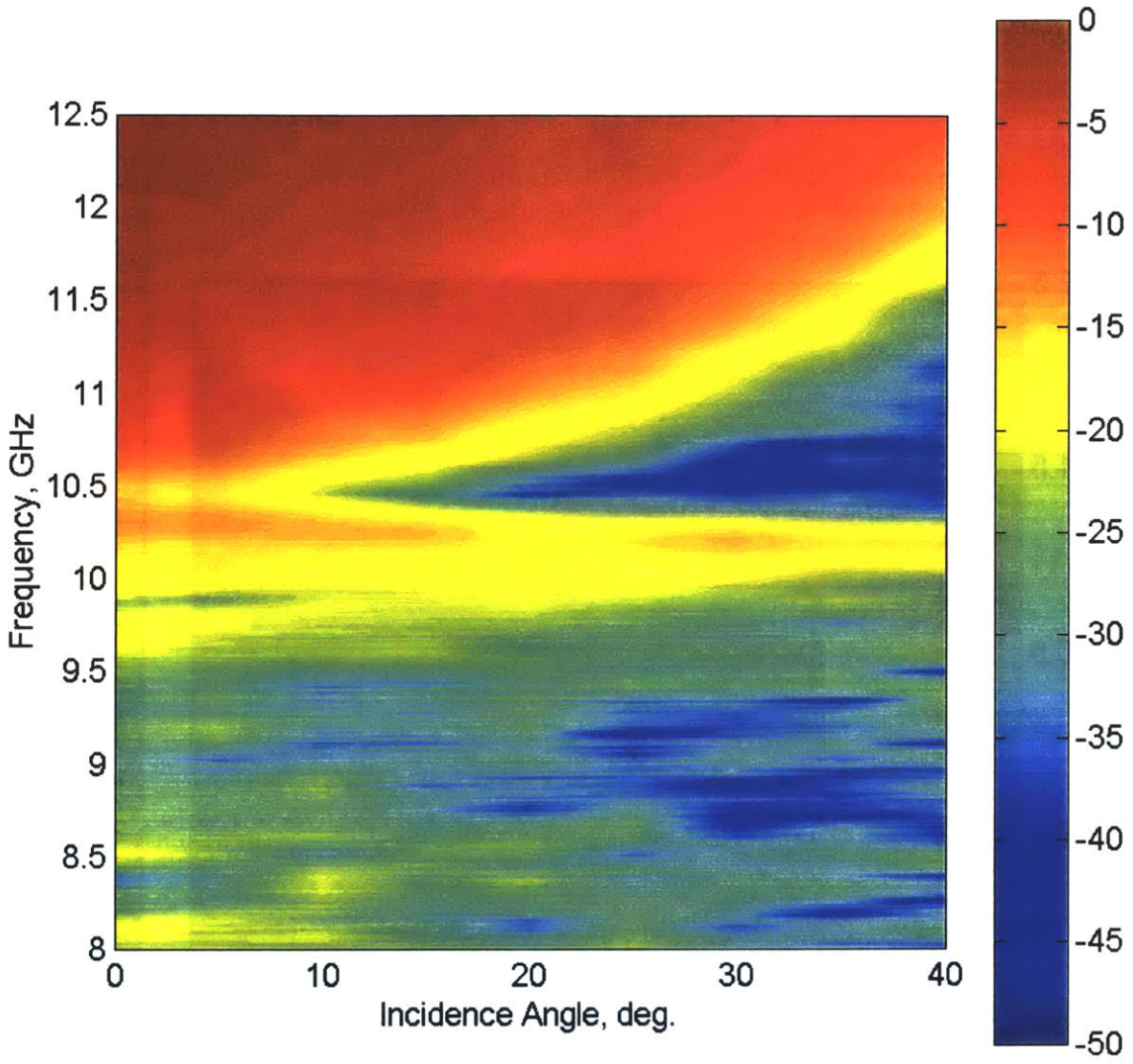

Figure 3-14: Normalized measured transmission through a 3 cm LHM slab over incident angle and frequency. (color)

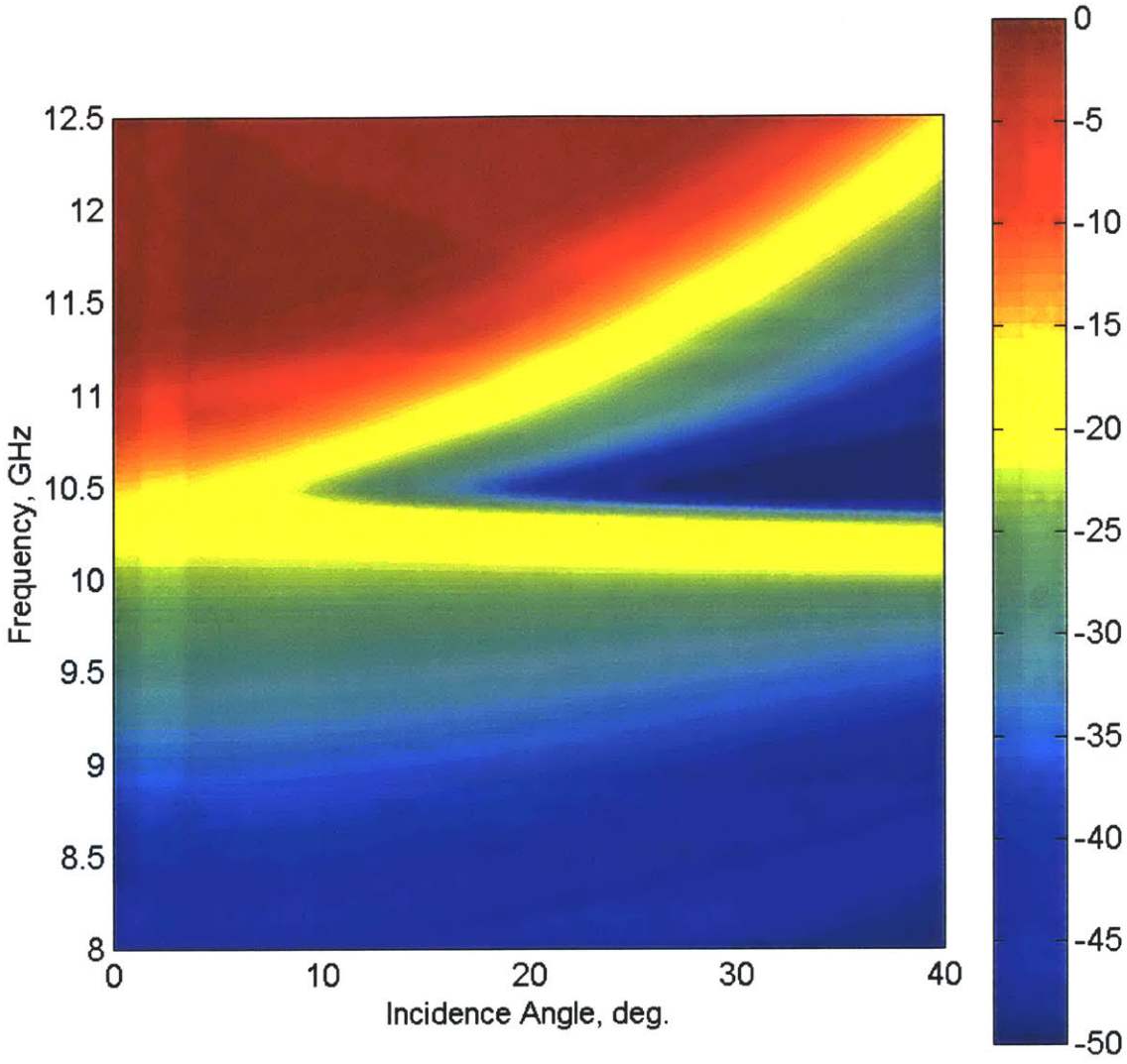

Figure 3-15: Theoretical transmitted power through 3 cm LHM slab over incident angle and frequency with $\gamma_{e,m} \neq 0$. (color)

Chapter 4

Measurement Results for a Four-Port Device

4.1 Introduction

Left-handed metamaterials are necessarily frequency dispersive, which can result in a frequency dependent sign of refraction. This feature could be used to make a three-port device of the T-junction setup studied in [33, 34], which used a metamaterial prism inside a waveguide to demonstrate negative refraction of power.

In this chapter we extend this idea to a four-port device, a conceptual representation of which is shown in figure 4-1. The device consists of a metamaterial wedge at the junction of the four ports. An electromagnetic wave is fed into port 1 which is then incident upon the wedge. Frequency dependent refraction and reflection occur at the interface. The transmitted "LH frequency band" is negatively refracted towards port 4. Similarly the transmitted "RH frequency band" is positively refracted towards port 3. The reflected power is collected at port 2.

We define the passband at each port as the 3 dB band centered at the most highly transmitted frequency. Designing the device consists of selecting an appropriate metamaterial and defining a geometry for the wedge that allows transmission to the LH and RH ports.

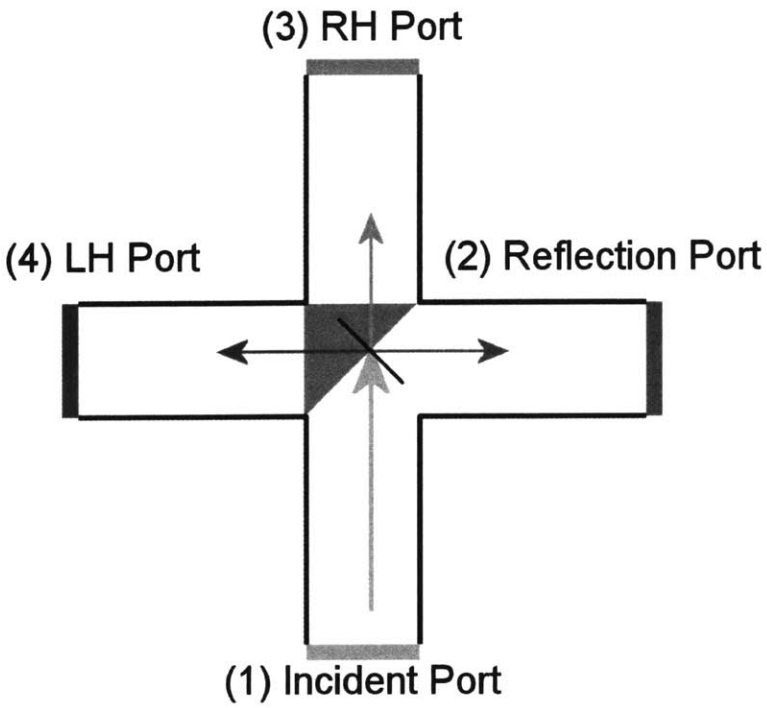

Figure 4-1: Four-Port device concept.

4.2 Metamaterial Selection

In order for the four-port device to work properly, a metamaterial that supports negative refraction is needed. We consider metamaterials that can be described by biaxial, anisotropic constitutive parameters as potential candidates in the design. Reproducing equations 2.1 and 2.2 compactly, the frequency dependent permittivity and permeability tensors are written respectively as:

$$\overline{\overline{\epsilon}} = diag\left[\epsilon_x(\omega), \epsilon_y(\omega), \epsilon_z(\omega)\right]\epsilon_o \tag{4.1}$$

$$\overline{\overline{\mu}} = diag\left[\mu_x(\omega), \mu_y(\omega), \mu_z(\omega)\right]\mu_o. \tag{4.2}$$

The free space constants are represented by ϵ_o and μ_o such that $\epsilon_{x,y,z}$ and $\mu_{x,y,z}$ represent the relative values. These relative values are functions of the radial frequency, ω.

The device is built inside a parallel plate waveguide with a plate separation small

enough such that the incident field consists only in the TEM mode. We take the plate separation in the $\hat{y}$ direction, which gives a $\hat{y}$ polarized electric field for the TEM mode. The dispersion relationship for this field is [1]:

$$k_z^2 = \frac{\omega^2}{c^2}\mu_x(\omega)\epsilon_y(\omega) - \frac{\mu_x(\omega)}{\mu_z(\omega)}k_x^2 \tag{4.3}$$

where c represents the speed of light in vacuum and the wave-vector is $\overline{k} = \hat{x}k_x + \hat{z}k_z$. Note that only $\{\epsilon_y, \mu_x, \mu_z\}$ are relevant for this mode. This dispersion relation has been studied in detail in [21] as a function of the sign of these parameters. When the $\hat{y}$ polarized electric field is incident from air onto a boundary that corresponds with a principle axis of the metamaterial, the sign of the refraction can be determined by the sign of the constitutive parameters, assuming phase matching is possible [1]. Table 2.1 summarizes the refraction properties when the physical boundary is parallel to the x principle axis of the material. The shape of the dispersion relation in the (k_x, k_z) plane is also given.

The refraction properties of anisotropic metamaterials given in table 2.1 are not exhaustive since they do not include any of the cases where the material axis and boundary are not aligned. However, most metamaterials are deficient in representing such boundaries well since the sub-wavelength structural unit cell the materials are composed of generally have a cross section in the x, z plane that is rectangular. Boundaries that do not fall along the unit cell grid must be approximated by a corrugated edge which may introduce unintended diffraction [35]. This issue is avoided here by taking the boundary along a principle axis.

As negative refraction of the power is indispensable to the operation of the four-port device, cases *ii*, *vi*, and *viii* are all possible solutions. Case *ii* is the simplest, as it only requires one dispersive component. The other cases require two or three simultaneously negative parameters.

4.3 Metamaterial Construction and Effective Parameters

We proceed by focusing on case *ii* in Table 2.1, which requires only negative permeability in one direction. To that affect, the symmetric split-ring resonator (SRR) first introduced in [22] is used as the unit cell structure. The cell constructed for measurement is shown in figure 2-6. The dimensions are given in table 2.2 and was designed in [14]. It consists of two metallic rings printed on a dielectric substrate.

The material axes are taken as marked so that the dispersive permeability (normal to the surface of the rings) is in the $\hat{z}$ direction. The structure was simulated using CST's Microwave Studio and the dispersive component of the permeability was found using the retrieval method of [18]. The permeability, μ_z, can be approximated by the Lorentz model [8] with the characteristic resonance frequency $f_{mo} \approx 10.08$ GHz and plasma frequency $f_{mp} \approx 10.56$ GHz.

The components ϵ_y and μ_x are approximated as constants. Ignoring the metallic structure, ϵ_y and μ_x assume the values of the background material which is dominantly air leading us to use $\epsilon_y = \mu_x = 1$.

Fabrication of the unit cell is done by printing rows of the SRRs onto large sheets of the dielectric substrate. The material is formed by cutting the sheet into strips which are lined up with the appropriate periodicity.

4.4 Geometric Design Issues

An appropriate geometry for the wedge needs to be specified in which the four parameters (shown in figure 4-2) can be optimized: the angle of incidence, θ_i, that the wave from port 1 impinges the material; the material rotation angles, ϕ_3 and ϕ_4, at the RH and LH ports (3 and 4); and the scale or size of the material, S. The rotation angle is defined as the counter-clockwise angle between the x axis of the material and the boundary. In the figure, the material axes are shown and dashed lines indicate port boundaries as absorbing material has been suppressed for clarity. The gray lines

forming the material indicate the orientation of the dielectric cards with SRRs for reference.

Each geometric parameter is discussed in terms of the effect it has in transmitting power to the measurement ports. Consistent with our selection of case *ii* from Table 2.1, the x axis of the material is parallel to the boundary where waves from port 1 strike the metamaterial.

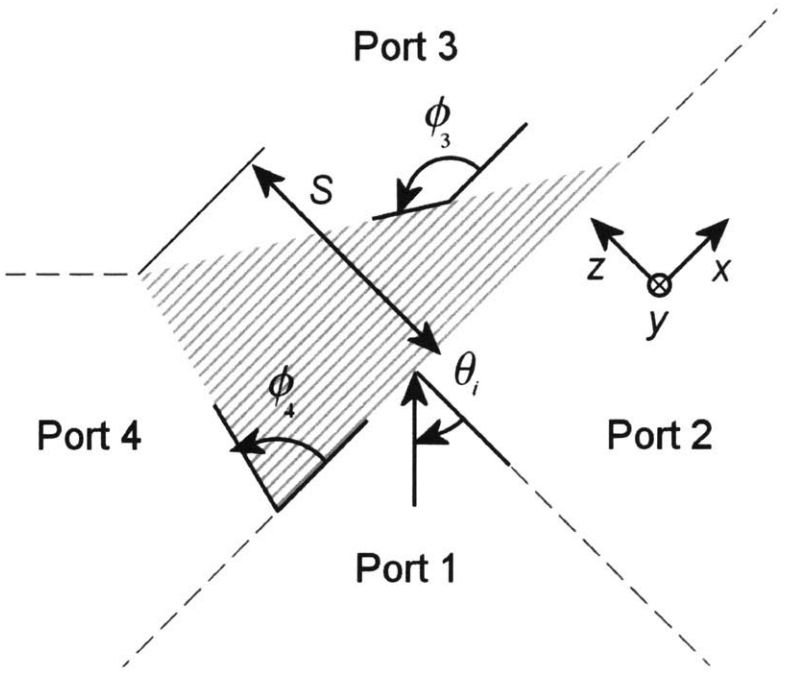

Figure 4-2: Metamaterial Design parameters.

4.4.1 LH Port

Having a transmission band at the LH port places restrictions primarily on θ_i and ϕ_4. These angles should be chosen so that a propagating wave transmits to port 4, and the positively refracted band does not meet the port 4 material boundary. By studying equation (4.3) in the region where $\mu_z(\omega) < 0$, we find many restrictions on these two angles which can simultaneously be met only over a small portion of the LH band [?].

We choose to design the device for the band near $\mu_z = -0.5$. Figure 4-3 shows the

path of an incident wave from port 1 to port 4 using the final selected values of $\phi_4 = 60°$, and $\theta_i = 15°$. The small and large arrows indicate the direction of energy flow in air and in the negative medium, respectively. The dashed line indicates the phase matching component of the suppressed k vector. The inset figures detail the dispersion relation in the area of interest. The thick line in the detail of the second interface indicates the possible k vectors in the negative medium that meet the transmission requirement. We see that if ϕ_4 were made significantly larger, phase matching would no longer be possible at the second boundary. Even if a correspondingly smaller θ_i was used, the negative refraction may not be large enough for the wave to reach the boundary. Also, if ϕ_4 is made smaller, some of the RH band strikes the boundary at port 4 rather than at port 3, deteriorating the stop band measured at port 4. While the scale parameter, S, also plays a role in determining if a refracted wave reached the port 4 or port 3 boundary, the issue is differed by assuming that the incident wave can be adjusted relative to the corner of the wedge. The material then can look as large or small as necessary to achieve the desired operation.

4.4.2 RH Port

It is convenient to select the orientation of the RH boundary, ϕ_3, to be the same as the incident boundary. We can justify this selection by noting that if $\phi_3 = 0$, the material appears as a slab to the positively refracted frequencies. By symmetry, incident waves that propagate into the medium can be phased matched at the second boundary. The net effect is a frequency dependent beam shift of the RH band [36, 37, 38].

4.4.3 Reflection Port

In the frequency band just past the plasma frequency, where $0 < \mu_z \ll 1$, the dispersion relation describes a narrow ellipse where $k_x \ll k_o$ for real k_z. Since $\theta_i > 0$ implies $k_x \neq 0$, there will be a frequency band above the plasma frequency where phase matching cannot be satisfied and a wave cannot propagate into the material. We expect the power reflected to port 2 to be high in this bandwidth. This

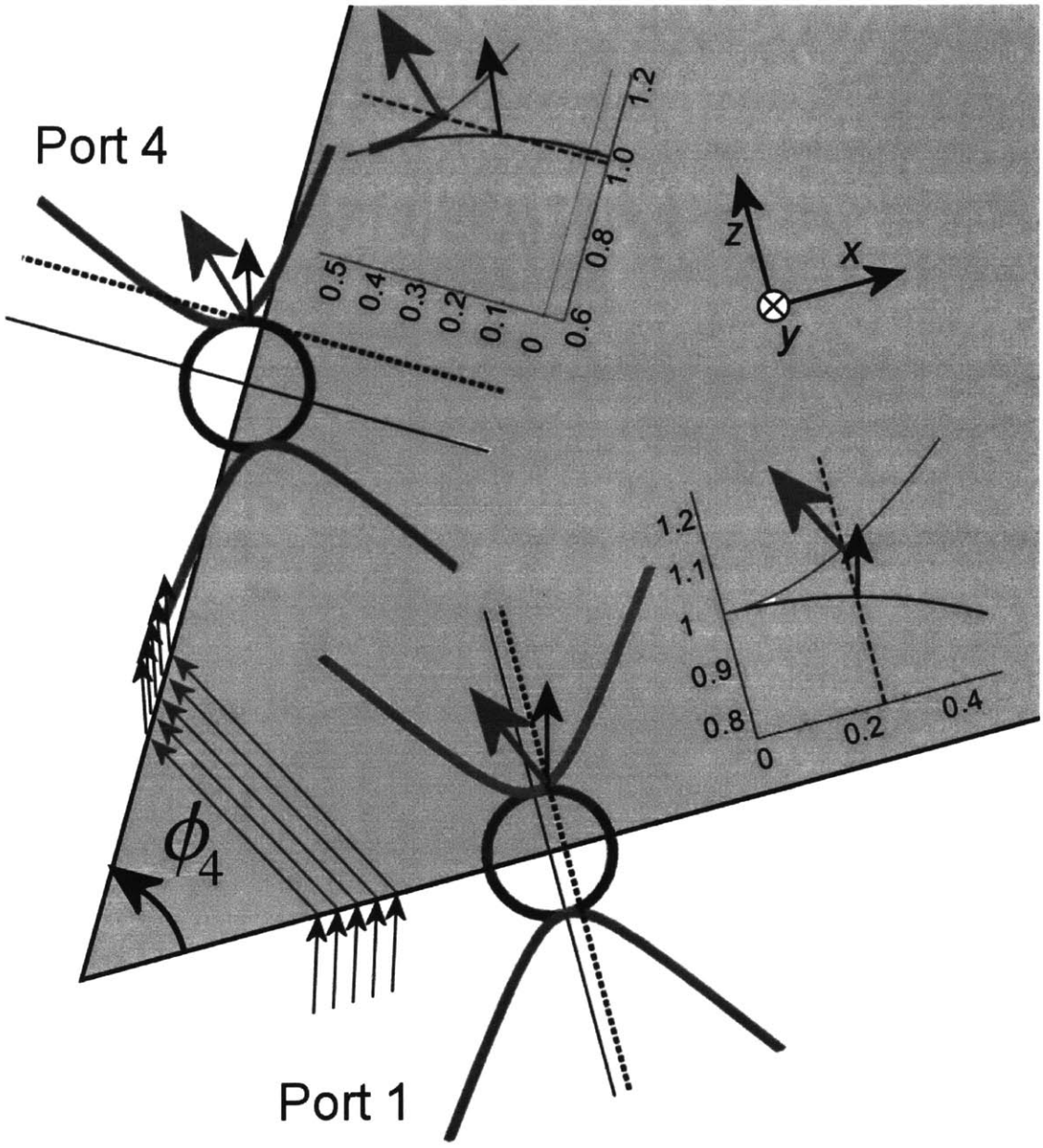

Figure 4-3: Demonstration of the refraction of a wave towards port 4.

conclusion is supported by theory when the material is approximated as a 2D slab and the analytical formulations are used to calculate the reflected power for a 15° incidence [32, 39].

4.4.4 Scale

The scale, or thickness of the material, S, is a parameter that serves as a wild card in design. So far we have only defined angles for the structure, which has left the scale at large. The material must be ample enough so that the unit cells form an effective medium. It also must be thick enough to define a boundary at port 4. Nevertheless, the material cannot be arbitrarily large since the refracted angle of the RH band is less than ϕ_4 for frequencies sufficiently above the plasma frequency. If the material was too big, these waves would first reach the port 4 boundary rather than that of port 3. A thickness of 6 cm (twelve layers of unit cells) from the incident to the port 4 material boundaries has proven satisfactory in measurements.

4.5 Experimental Setup and Results

The material construction itself was consistent with the description in Sec. 4.3 but with one notable difference. In order to minimize corrugation at the LH port boundary, the centers of the unit cells were shifted to fall directly onto the boundary. This technique avoided uneven stair-stepping in favor of a constant shift of the cells from row to row insuring that diffraction effects are minimal [35].

For measurement, the metamaterial was placed inside a parallel plate waveguide like shown in [8]. A diagram of the setup is shown in figure 4-4. The bottom plate is shown in gray. Microwave absorbing material is represented by the black wedges and the material axes are shown. The final design angles are used: $\phi_4 = 60°$ and $\theta_i = 15°$. The choice of S as twelve unit cells corresponds to a thickness of $S = 6$ cm.

Microwave absorber was used as necessary to maintain plate separation, minimize direct coupling between ports, minimize diffraction, and minimize influences from the external environment. A WR90 waveguide to SMA adapter fed the microwave signal

between the plates at port 1. The same type of adapter was used for measurement at ports 2, 3, and 4. The plate separation was approximately the height of the material, 1 cm.

In comparison to figure 4-1, port 1 and 2 are much closer due to the small incidence angle needed. In fact, there was no need to use absorber between these two ports to achieve the desired device operation. Also, the conceptual triangular shape is replaced with one more suited to insuring propagating waves at ports 3 and 4. Finally port 4 is closer to the edge of the material due to the generally large transmission angle anticipated at the port 4 material boundary.

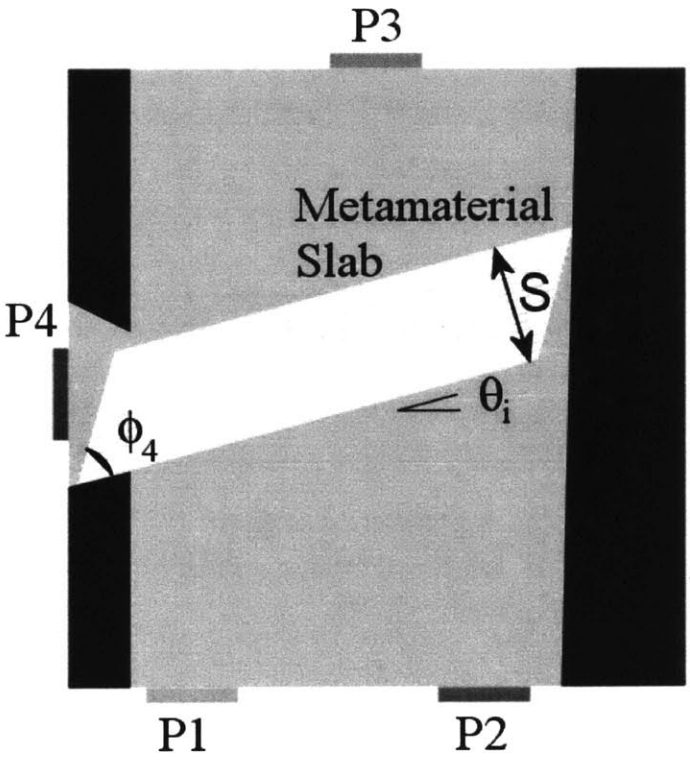

Figure 4-4: Top view of experimental setup with top plate removed.

An HP-8510 network analyzer was used for measurements in the X-band, (8.2 GHz to 12.4 GHz), and the measurement results are presented in figure 4-5. The dash-dot line indicates the power at port 2, the reflection port. The dashed line shows transmission at the RH port (3) and the solid line indicates the power at the LH port (4). The 3dB passbands are indicated by shading.

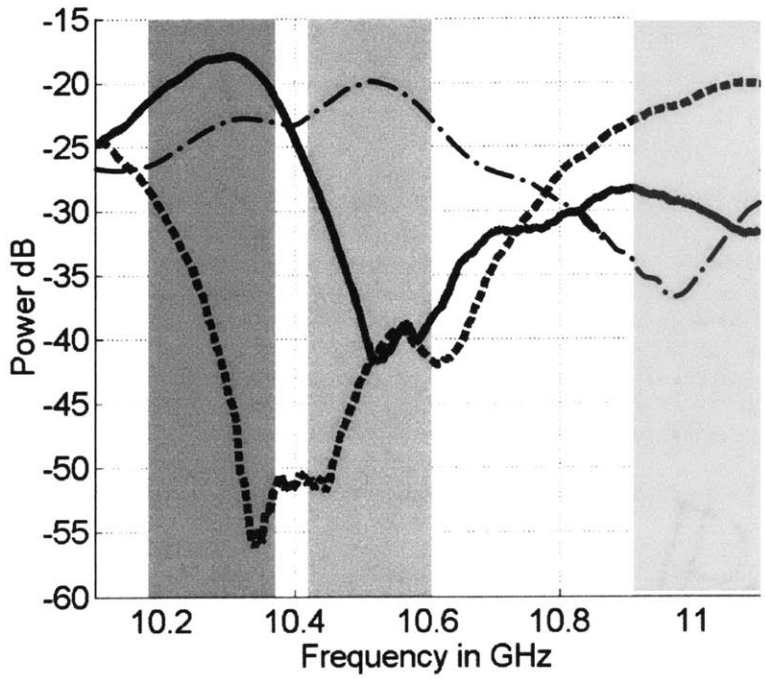

Figure 4-5: Four-Port Device experimental measurement results.

The measurement at the RH port shows a strong stop band centered near 10.4 GHz which is inside the negatively refracted band. The left portion of the stop band can be attributed to power being refracted towards the LH port, and the right due to high reflection. Measurements at the LH and reflection ports corroborate this assessment. At the LH port a peak appears in a band corresponding to $\mu_z < 0$. The measured LH band is in good agreement with the retrieval results, peaking at 10.3 GHz. In the region near the plasma frequency, where $|\mu_z| \ll 1$ the reflected power increases and peaks at 10.5 GHz. Above the plasma frequency, as $\mu_z \to 1$, transmission to the RH port dominates.

Passbands have been shaded using the criteria outlined in Sec. 4.1. In the operating band of 10.1 GHz to 11.1 GHz, we find that an LH band of 190 MHz is achieved at port 4. At port 2, a bandwidth of 187 MHz is measured and at port 3, the RH band is 192 MHz. The RH bandwidth however is superficially limited by the band of interest and could easily be increased by raising the upper limit of the frequency range. In the remainder of the X-band the signal at port 3 is dominant.

4.6 Chapter Summary

In this chapter we have realized a four-port band select device using an anisotropic metamaterial with a permeability that is frequency dispersive and achieves negative values. The use of frequency dependent refraction to differentiate an incident signal into different bands has been verified experimentally.

While case *ii* of table 2.1 was studied in detail, the dispersion curves for two (case *vi*) or three (case *viii*) dispersive parameters suggest a device in which negatively refracted waves can more easily be phase matched over a broader band at the LH port. Many of the metamaterial structures thus far proposed (and those available at the time of measurement) use vertical rods to achieve plasmatic permittivity, which cases *vi* and *viii* both require. Good electrical contact between the rods and parallel plates is needed for the plasma effect, which is difficult to achieve in measurement. S-shaped structures which achieve both negative permittivity and permeability have been proposed to eliminate this issue [27, 29]. Negative permittivity could be skirted entirely if a denser dielectric was used outside the wedge in case *ii*, allowing for easier phase matching at the LH port due to the larger dispersion circle.

In the next chapter the four-port device is reinvestigated analytically. Stricter geometric properties are required for a more practical device. Left-handed materials with up to three dispersive parameters are investigated and the transmission properties for three example designs are calculated.

Chapter 5

Theoretical Exploration of the Four-Port Device

5.1 Introduction

In this chapter we investigate analytically the four-port device introduced in chapter 4. Several refinements are made to the device, primarily to improve the physical layout of the ports. The transmission properties are studied for metamaterials with one, two, or three dispersive parameters.

A schematic of the four-port device is shown in figure 5-1. The device operates on an input signal incident onto the metamaterial prism from port 1. The dispersion relationship at each frequency determines the refraction angle, if any, at the the port 1 boundary of the metamaterial. If no real refraction angle exists, the signal is primarily reflected towards port 2, labelled as the reflection port. When the refraction angle is real, some power propagates into the metamaterial and is directed towards port 3 or port 4 if the refraction is positive or negative, respectively.

5.2 Design Constraints

There are many variables at our disposal in designing the four-port device. In order to constrain the problem several parameters are fixed to practical values.

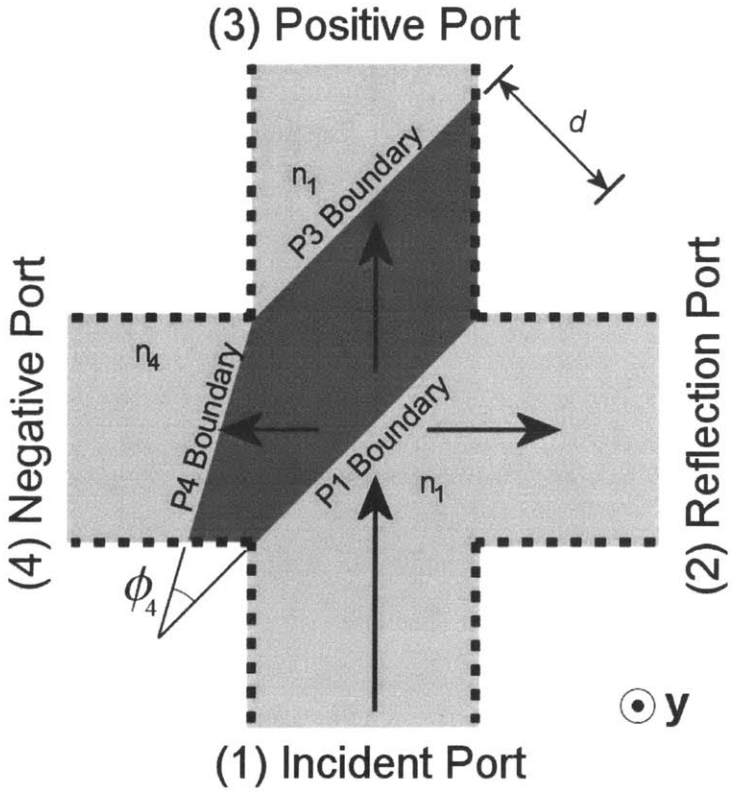

Figure 5-1: Top view of the four-port device. The dark gray indicates the metamaterial prism and the light gray indicates the bottom parallel plate waveguide conductor. The top plate has been suppressed. n_1 and n_4 indicate the dielectric materials between the PEC boundaries. ϕ_4 indicates the angle between the port 1 and port 4 boundaries. d indicates the distance between the parallel port 1 and 3 boundaries. The dashed black lines indicate absorbing material so that the ports are coupled only through the prism.

The device studied is designed to be realized in a parallel plate waveguide where the plate separation and frequency are limited such that the incident signal consists of only the fundamental mode. The $\hat{y}$ axis in figure 5-1 corresponds to the direction of separation between the parallel plates.

In this chapter the same permittivity and permeability tensors are assumed as in chapter 4 (eqs. 4.1 and 4.2). The dispersion relationship for the $\hat{y}$ polarized electric field is given by equation 4.3.

The frequency dependent parameters are described by the lossless Lorentz model which is assumed to be valid for the frequencies of interest [8].

$$\delta(f) = \delta_{bg}\left(1 - \frac{f_p^2 - f_o^2}{f^2 - f_o^2}\right) \tag{5.1}$$

The parameters f_p and f_o represent the plasma and resonant frequencies, respectively. We require $f_p > f_o$ for dispersive μ and $f_o = 0$ for dispersive ϵ. δ_{bg} represents the high frequency limit defined by the dielectric background material with relative permeability $\mu_{bg} = 1$ and relative permittivity ϵ_{bg} to be specified.

The angles between adjacent ports are fixed to 90°. The transmitted power to ports 2 and 3 must reach these ports such that the group velocity vector, $\bar{v}_g$, is normal to them. This exit angle requirement demands that the port 1 boundary is at a 45° angle with respect to the incident signal. The port 3 boundary is parallel to the port 1 boundary so that the prism can be approximated as an infinite slab for positively refracted waves. Since the medium on both sides of the slab has an index n_1, the exit angle requirement is met at port 3.

The exit angle at port 4 varies with frequency and a similar constraint cannot be met for a non-zero bandwidth. We define a center frequency, f_c, at which $\bar{v}_g$ is normal to the boundary and consider a band where the group velocity makes an angles less than 10° with the normal. The band within ±20° is also reported.

5.3 Design Parameters and Performance Estimation

5.3.1 Design Parameters

In designing the device the constitutive parameters of the metamaterial prism must be specified. This includes the selection of all resonance and plasma frequencies, as well as the background permittivity. The $\hat{y}$ axis of the metamaterial corresponds with the $\hat{y}$ direction labelled in figure 5-1. The orientation of the $\hat{x}$ and $\hat{z}$ axes of the metamaterial is specified by ψ_m, defined as the clockwise angle from the port 1 boundary to the $\hat{x}$ principle axis of the metamaterial.

The angle ϕ_4 in figure 5-1 refers to the angle between the port 1 and port 4 boundaries. The distance d is measured from the port 1 boundary to the port 3 boundary.

5.3.2 Performance Estimation

The power transmitted to each port is estimated to characterize the performance of a given design. The infinite slab approximation discussed previously is used to calculate the port 3 power [30, 31]. Calculations are made for positive and imaginary refraction angles at the port 1 boundary [32, 40].

Since the metamaterial is lossless, the power reflected to port 2 is simply the complement of the power transmitted to port 3, except when the refraction is negative. Here the power is estimated by the half space reflection. The power transmitted to port 4 is calculated by the product of the power transmitted through both the port 1 and port 4 boundaries when both are treated as half spaces. The derivation of the transmission coefficient is shown in appendix D. The incidence on the second boundary is based on the refraction angle from the first [41].

Any analytical approximation has deficiencies in predicting the behavior of this device. Two limitations of those used here are worth mentioning: the infinite slab approximation is only valid for sufficiently small beam shifts, and any power reflected

Table 5.1: Four-port device example parameters.

Parameters		Example 1	Example 2	Example 3
ϵ_y	ϵ_{bg}	1	2	3
	f_{yp} (GHz)		9.51	10.98
μ_x	f_{xo} (GHz)			9.00
	f_{xp} (GHz)			10.00
μ_z	f_{zo} (GHz)	9.00	9.00	9.00
	f_{zp} (GHz)	10.00	10.00	10.00
ψ_m		0°	0°	0°
ϕ_4		90°	90°	45°
n_1		1	1	1
n_4		1.9	1	1
d (cm)		5	5	5

from the port 4 boundary is not accounted for.

5.4 Device Design

In total there are eleven design parameters which are listed in table 5.1. For clarity the resonance and plasma frequencies have the added subscript of the direction they are associated with. In general, design is an optimization process whereby these parameters are selected to meet specific performance criteria. Here we discuss the design process and give examples for incrementally more complex metamaterial prisms. The design examples give preference to the the most practical values of the parameters, particularly in the choice of n_1, n_4, ψ_m, and ϕ_4.

Although d only comes into the formulation directly when estimating the power to ports 2 and 3, we note that the length of the boundary at port 4 is directly affected by its choice. The choice $d = 5$ cm is used in the three example designs we present.

5.4.1 One Dispersive Parameter

In order for a wave to be negatively refracted at the port 1 boundary, the metamaterial must have dispersion in at least one component of the permeability. If μ_z is the

dispersive component and $\psi_m = 0$, the refraction at the port 1 boundary is negative from f_{zo} to f_{zp}, the band where the dispersion relationship is hyperbolic. Changing n_1 and ϵ_{bg} alters the way the refraction changes from 0° to −90° within this band. The effect is demonstrated in figure 5-2(a) where $f_{zo} = 9$ GHz and $f_{zp} = 10$ GHz. The solid black curve shows the refraction angle variation with frequency when $\epsilon_y = 1$ and $n_1 = 1$. If ϵ_y is increased, the curve bends towards the upper right corner of the graph (dashed gray). If n_1 is increased, the curve to bends downwards towards the limit where $n_1 \to \infty$ (solid gray). A rotation by ψ_m (dashed black) changes the band of negative refraction to include frequencies below 9 GHz where the material is strictly positive. Here the dispersion relationship describes a rotated ellipses with high eccentricity making negative refraction possible.

The transmitted power must also be considered before any configuration is selected, as can be seen in figure 5-2(b) where the transmission for each case is plotted. The case where n_1 is very large is completely reflected.

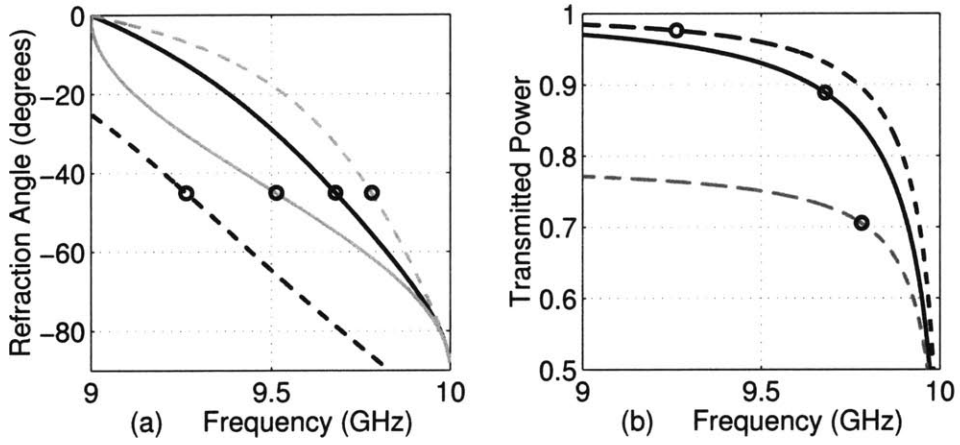

Figure 5-2: Refraction angle (a) and transmitted power (b) with dispersive permeability (μ_z) at the port 1 boundary. $f_{zo} = 9$ GHz, $f_{zp} = 10$ GHz. *Solid Black* $\epsilon_y = 1$, $\psi_m = 0°$, $n_1 = 1$. *Solid Gray* $\epsilon_y = 1$, $\psi_m = 0°$, $n_1 \to \infty$. *Dashed Gray* $\epsilon_y = 4$, $\psi_m = 0°$, $n_1 = 1$. *Dashed Black* $\epsilon_y = 1$, $\psi_m = -25°$, $n_1 = 1$. Each circle indicates the $-45°$ refraction point.

The frequency, f_r, refracted at a $-45°$ angle, is the ideal center frequency of the transmission band at port 4. To have $f_c = f_r$, the choice of n_4 and ϕ_4 is made to minimize the refraction and maximize the transmission at f_r. The maximum power

received at port 4 occurs at the frequency f_S. Ideally f_S is the same frequency as f_c.

We now give an example of the four-port device with one dispersive parameter. We continue using the selection of $f_{zo} = 9$ GHz and $f_{zp} = 10$ GHz to define the characteristics of the dispersive parameter μ_z. Simplicity dictates the selection of the free-space value for the index n_1 and the permittivity ϵ_{bg}. The black curve in figure 5-2 shows that negative refraction and good transmission through the first boundary are expected if $\psi_m = 0°$. Our preference is to choose $n_4 = 1$, however, for this choice there is no selection of ϕ_m where a center frequency exists. We therefore choose $\phi_4 = 90°$ and calculate the index that leads to $f_r = f_c$ to be $n_r \approx 1.9$. The design parameters are summarized in table 5.1 as example 1.

Figure 5-3(a) shows the calculated transmission to each of the three ports as a function of frequency. The variation of the refraction angle at the port 1 boundary is visualized in figure 5-4(a) for frequencies from 5 to 20 GHz. The arrow indicates the wave incident from air (white) onto the metamaterial (light gray) at a 45° angle. At each frequency (represented by the thickness of the dark gray line) the refraction angle is shown.

The beam shift at port 3 is shown as the dashed black curve in figure 5-5. For these parameters the maximum power to port 4 is 90% of the incident power at $f_S = 9.64$ GHz. We find $f_r = 9.68$ GHz and $f_c = 9.63$ GHz. The slight difference in f_r and f_c is due to rounding the value of n_4. The band satisfying the $\pm 10°$ and $\pm 20°$ exit angle requirement while also having transmission greater than 50% has widths of 449 MHz and 507 MHz, respectively.

The negatively refracted bandwidth is from 9 GHz to 10 GHz. Due to the limitations of the transmission approximation, power is not conserved in this region. Just above 10.9 GHz, the beam shift is very large and the accuracy depends on the lateral extent of the metamaterial.

5.4.2 Two Dispersive Parameters

In allowing a second constitutive parameter to be dispersive we have the choice between ϵ_y and μ_x. The choice of μ_x, however, does not lead to any particular advantage

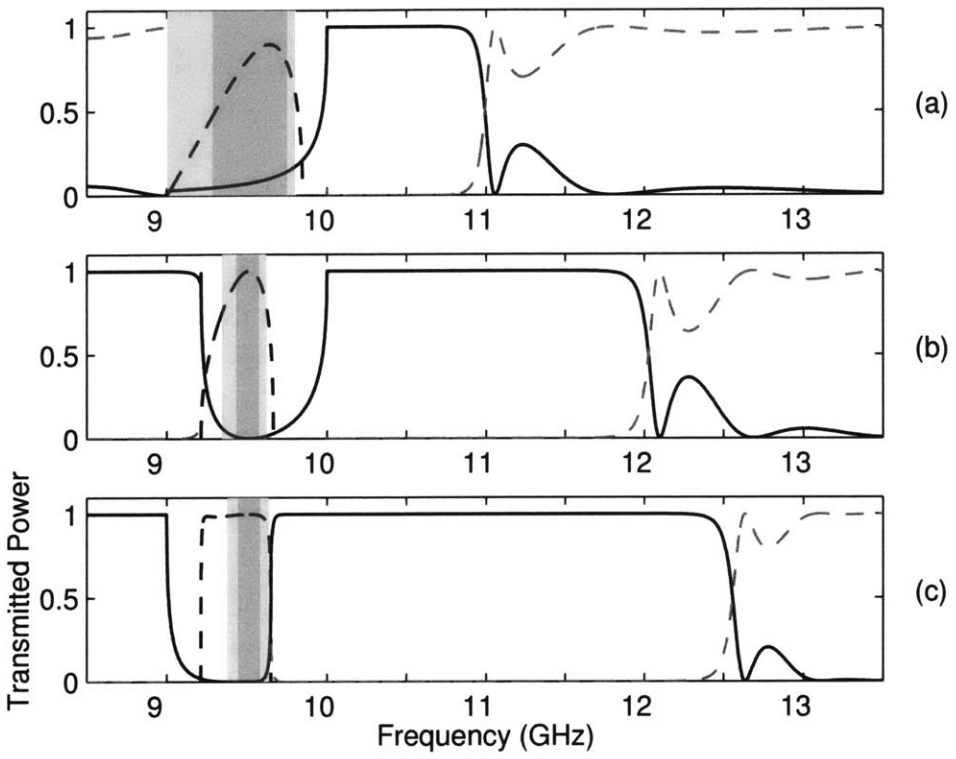

Figure 5-3: Absolute transmitted power to ports 2, 3, and 4 for examples 1, 2, and 3. *Solid*– Port 2, *Dashed Gray*– Port 3, *Dashed Black*– Port 4. The dark gray and light gray boxes indicate the bandwidth where the exit angle is within $\pm 10°$ and $\pm 20°$ of center frequency respectively.

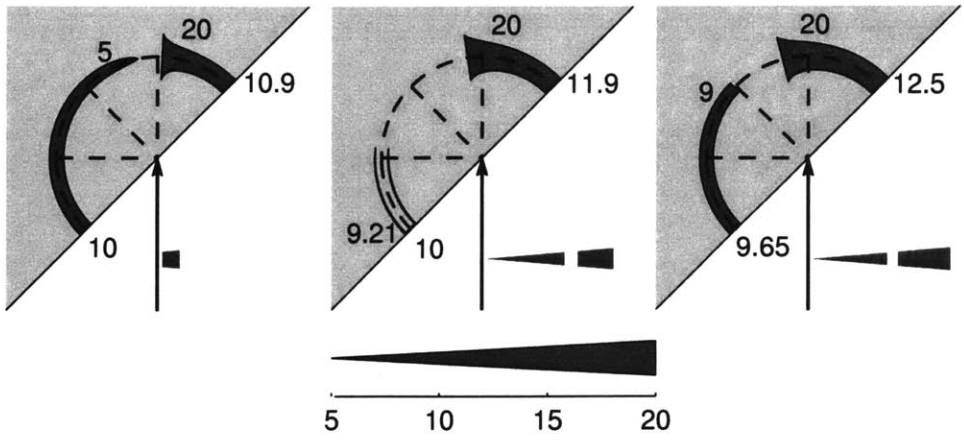

Figure 5-4: Visualization of the variation of refraction angle with frequency at the port 1 boundary for examples 1, 2, and 3. Frequency is represented by the line thickness and the refraction angle is represented directly by the angle shown. The first and last frequencies of each continuously refracted frequency range are labelled. Note that in (b), the negative refraction angle folds back on itself, beginning and ending at $-90°$. The spectrum with no real refraction angle is shown in the white space.

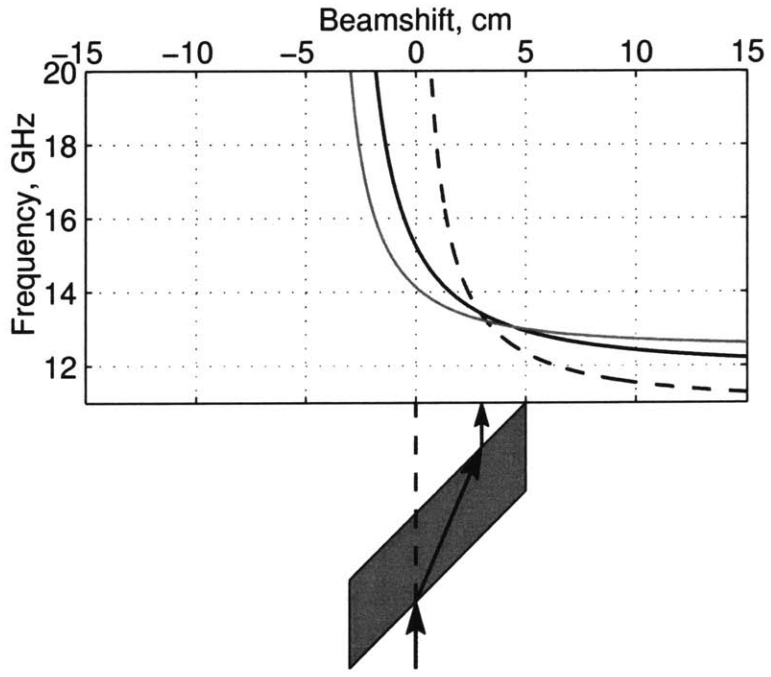

Figure 5-5: Beam shift for the positively refracted region. *Dashed Black*– Example 1. *Solid Black*– Example 2. *Solid Gray*– Example 3.

over the first case in exchange for the added complexity. Selecting the permittivity to be dispersive offers a much more interesting case for study since it can eliminate the need to choose a dielectric material at port 4.

In example 1, waves refracted towards the port 4 boundary could not be phased match without $n_4 > 1$. This problem can be eliminated by decreasing the value of the permittivity in the negative permeability band, essentially bringing he hyperbolic curves closer to the origin of the k space. Near f_{yp}, the sign of the permittivity is irrelevant to the refraction behavior which is dictated entirely by the hyperbola's asymptotes. The selection of f_{yp} is a tradeoff between bandwidth and power.

As an example for the case of two dispersive parameters we modify the first example to operate with $n_4 = 1$ by adding the plasmatic permittivity with f_{yp} chosen so that $f_r = f_c = f_S$. We find that without changing ϵ_{bg}, the asymptotic return to the background material parameters broadens the reflection bandwidth considerably. Increasing the background permittivity to $\epsilon_{bg} = 2$ makes phase matching possible at a considerably lower frequency.

The modified design parameters are listed as example 2 in table 5.1. The results are shown in figures 5-3(b), 5-4(b), and 5-5 (solid black). The electric plasma frequency, f_{yp}, is chosen such that $\mu_z(f_{yp}) = -1$. At f_{yp}, equation 4.3 reduces to $k_z^2 = k_x^2$ and the refraction angle is $-45°$ implying $f_{yp} = f_r$. From equation 5.1 we find $f_{yp} = 9.51$ GHz. The calculated results show $f_S = f_c = f_r = 9.51$ GHz. The port 4 bands satisfying the $\pm 10°$ and $\pm 20°$ exit angle requirement have widths of 144 MHz and 278 MHz, respectively. The transmitted power is 75% of the incident power or higher throughout the $\pm 20°$ port 4 band.

Refraction from the port 1 boundary at $-45°$ also occurs at $f_r = 9.25$ GHz. This is expected since the negatively refracted band begins and ends at $-90°$, as is depicted in figure 5-4(b). It is interesting to note that the turning point is $-40°$ at 9.34 GHz. While the direction of the group velocities from $-90°$ to $-40°$ are achieved at two frequencies, the wave vectors at these frequencies are different, leading to very different transmission properties.

5.4.3 Three Dispersive Parameters

If μ_x, μ_z, and ϵ_y are all dispersive, there are five resonance and plasma frequencies to be specified. There are thirty combinations of the relative locations of these parameters, twelve of which have a region where all three are simultaneously negative. It is beyond the scope of this work to comment on each case, but we note that it is now possible to have two distinct bandwidths of negative refraction.

As an example we study an isotropic material where the dispersive parameters are chosen such that $\mu_x = \mu_z = \epsilon_y = -1$ at $f_r = 9.51$ GHz. The parameters are listed in table 5.1. Perfect transmission into the metamaterial is predicted at f_r where the refraction angle is $-45°$. The choice of $\phi_4 = 45°$ is made such that $f_r = f_c = f_S$ while having $n_4 = 1$. The results for example 3 are shown in figures 5-3(c), 5-4(c), and 5-5 (solid gray). The choice of $\epsilon_{bg} = 3$ is made to reduce the reflection bandwidth. The width of the bands at port 4 satisfying the $\pm 10°$ and $\pm 20°$ are 139 and 254 MHz, respectively. The transmitted power throughout the $\pm 20°$ band is 89% or higher.

5.5 Chapter Summary

The four-port device introduced in this chapter utilizes the dispersive nature of left-handed materials to differentiate an input signal into three bandwidths. Selecting values for the parameters available for design can be viewed as an optimization problem, however, our approach has been to demonstrate the functionality of the device using parameters that could be realized experimentally.

The examples given demonstrate the trend towards a reduction in bandwidth as the number of dispersive parameters the metamaterial has is increased. However, the added complexity has been shown to improve transmission in the band.

Chapter 6

LHM Microstrip Measurements

6.1 Introduction

The design of LHM has been mainly focused on 3D structures but similar structures have found use in planar applications. In [42], dielectric split-ring resonators are milled from the ground plane of a microstrip to create a stopband in transmission. This effect, however, is not predicted by treating the substrate as an effective medium. In this chapter an LHM consisting of implanted split-ring resonators (SRR) is used as a substrate for a microstrip line. We show here that the effective medium parameters of the substrate predict the microstrip transmission behavior. The use of an LHM substrate is shown to enhance the performance of a microstrip filter.

The microstrip is aligned with the LHM substrate such that the surface of each SRR is perpendicular to the propagation direction and the microstrip surface. This orientation is selected because the magnetic field of the guided wave is also primarily in this direction. Since in the frequency band of negative permeability the permittivity is still positive, the quasi-TEM wave has a primarily imaginary wave vector so that the wave is attenuated producing a natural stopband. This natural stopband capability is combined with a planar microstrip filter design to enhance the overall bandwidth.

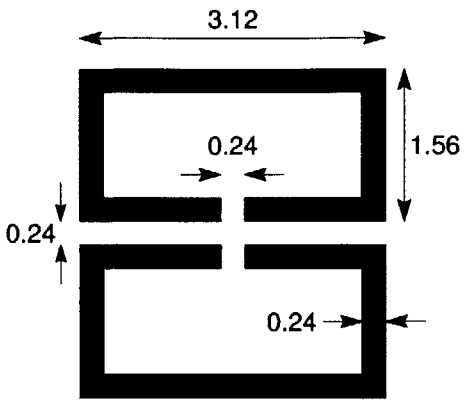

Figure 6-1: Symmetric split-ring resonator with the dimensions labelled in millimeters.

6.2 Microstrip Substrates

A non-dispersive and a dispersive substrate are constructed for measurements. The dispersive substrate is a metamaterial consisting of symmetric split-ring resonators (SSRRs) [22], implanted with a fixed periodicity and orientation in a dielectric material. The dominant effect of the SSRR is to produce a dispersive permeability in the direction normal to its surface area, as can be directly seen from a reflection and transmission experiment followed by a retrieval process [18]. All the SSRRs are oriented in the same direction such that the permeability of the substrate may be approximated by a uniaxial tensor with two constant components and one frequency dependent component.

The SSRR design used in these experiments was first presented in [14]. The dimensions and structure are shown in figure 6-1. The rings are printed on a dielectric strip of thickness 0.5 mm and relative permittivity, $\epsilon_r = 3.6$. To realize the substrate, the SSRR structure is printed sixteen times on a single strip as shown in figure 6-2. The spacing between unit cells is 5.0 mm in the printed direction giving a total strip length of 8.0 cm. The height of the strip is 5.0 mm.

In order to achieve the lateral periodicity, two additional strips lacking the SSRR metallizations are placed contiguously with the printed strip. These dielectric strips have a width of 0.38 mm each giving a lateral periodicity of 1.27 mm. The total

substrate is the compilation of 36 repetitions of the lateral periodicity. The completed substrate has a height of 5.0 mm, a length of 8.0 cm, and a width of 4.5 cm. Figure 6-2 summarizes the construction process.

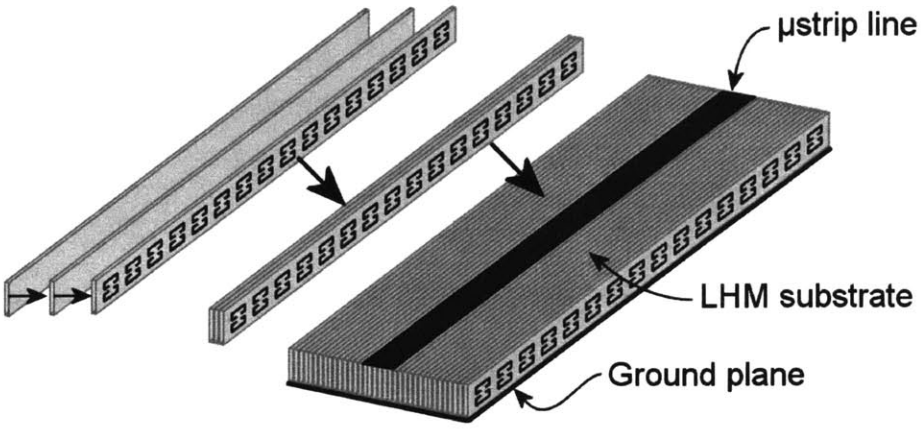

Figure 6-2: Schematic view of the metamaterial substrate constructed by combining dielectric strips with and without SSRRs in a two to one ratio. Thirty-six repetitions of this periodicity are combined to form the substrate. The final stage of construction is the addition of a microstrip and ground plane.

In order to determine the effective material parameters of the dispersive substrate, a single SSRR surrounded by a dielectric ($\epsilon_r = 3.6$) with the dimensions of the periodicity is simulated using the commercial software package CST Microwave Studio (MWS). The constitutive parameter retrieval algorithm presented in [18] is then applied to the simulated S-parameters. The frequency dependence of the retrieved permeability is similar to the Lorentz dispersion model [8], with parameters $f_{mo} = 7.0$ GHz and $f_{mp} = 8.1$ GHz.

The non-dispersive substrate is constructed in a similar fashion except that only dielectric strips without printed SSRRs are included in the stack. The dimensions of the non-dispersive substrate are the same as those of the dispersive substrate.

6.3 Microstrip Measurements

The device is completed with the addition of a 4.0 mm wide aluminum microstrip line and ground plane to each substrate, as shown in figure 6-2. An HP-8510 vector

network analyzer with 50 Ω air lines is used to measure the transmission. SMA to microstrip adapters are connected to the ends of the line and manually connected to the ground plane and microstrip line. To test the homogeneity of the dispersive substrate, measurements are taken for three different placements of the microstrip. The results were similar in each case. Figure 6-3(a) shows the transmitted power for the non-dispersive and dispersive substrates. The average of the three measurements is shown for the dispersive substrate.

The dispersive substrate exhibits a stopband centered at 7.5 GHz. The stopband corresponds to the region near the negative permeability bandwidth which confirms that the substrate can be treated as an effective medium even when it is used as a microstrip substrate. The stopband extends slightly beyond the bandwidth of strictly negative values and includes the region both below and above, where the permeability takes very large and very small values, respectively. The location of the stopband is consistent with MWS simulations where a dispersive, anisotropic substrate with a Lorentz permeability having the same parameters given earlier is used.

Both measurements are seen to have the general trend of decreasing with increasing frequency. Simulation results confirm that this is primarily due to radiation rather than mismatch. Radiation losses can be reduced by using a thinner substrate.

6.4 Stopband Filter Design

A simple stopband filter can be created by the addition of an open circuit shunt stub to an existing transmission line. At the frequency where the stub is a quarter wavelength, the stub appears from the line as a short circuit, which creates a simple stopband filter. The filter design can be enhanced by introducing multiple stubs and specifying the characteristic impedance of each to achieve the desired bandwidth and passband ripple level [43].

The stopband of a quarter-wave stub filter can be enhanced by the use of the LHM substrate. Stubs will be added perpendicularly to the microstrip such that the non-dispersive permeability component is dominant, and we can use the non-dispersive

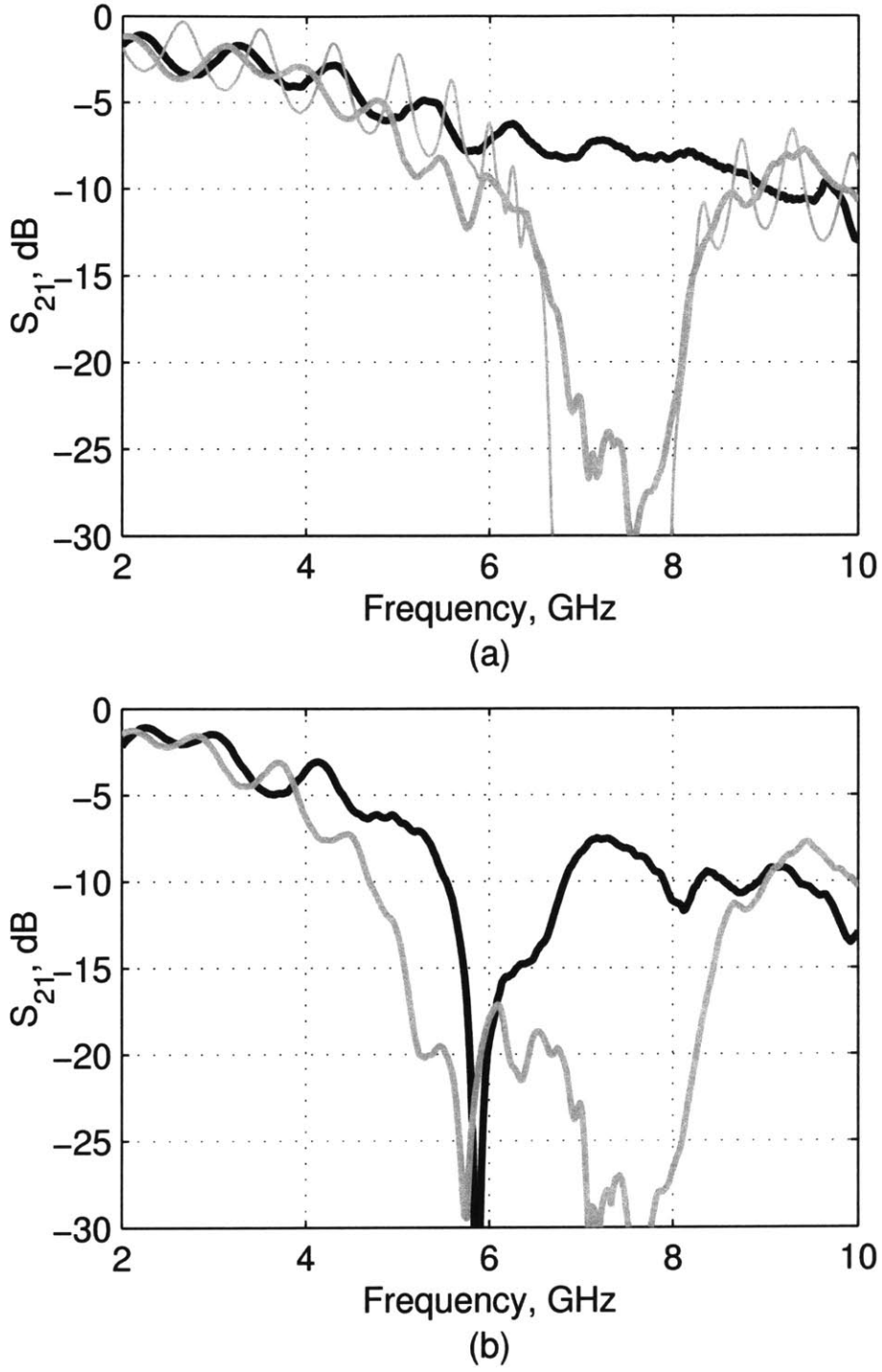

Figure 6-3: (a) S_{21} in dB for transmission on 4 mm microstrip on the non-dispersive (black) and dispersive (thick gray) substrate. Simulation results are shown for the dispersive substrate (thin gray). (b) Microstrip filter measurements on the non-dispersive (black) and dispersive (gray) substrates.

substrate to estimate the appropriate stub length. The unwrapped phase, ϕ, from the non-dispersive substrate measurement is used to calculate the phase velocity as

$$v_p = \frac{2\pi d}{d\phi/df}, \tag{6.1}$$

where d is the 8 cm length of the strip, and f is the frequency [1]. The quarter-wave strip length, l, is then estimated as

$$l = \frac{v_p}{4f}. \tag{6.2}$$

Figure 6-4 shows the calculated length l needed for the shunt stub of the filter. The gray curve shows the calculated length when $d\phi/df$ is the derivative of unwrapped measurement, $\angle S_{21}$. The black curve shows the result when the unwrapped phase measurement is fit to a straight line over the 5 to 8 GHz band. In this case v_p is a constant and l is simply proportional to $1/f$. We see that the linear fit predicts a stopband at 6.0 GHz for $l = 5$ mm.

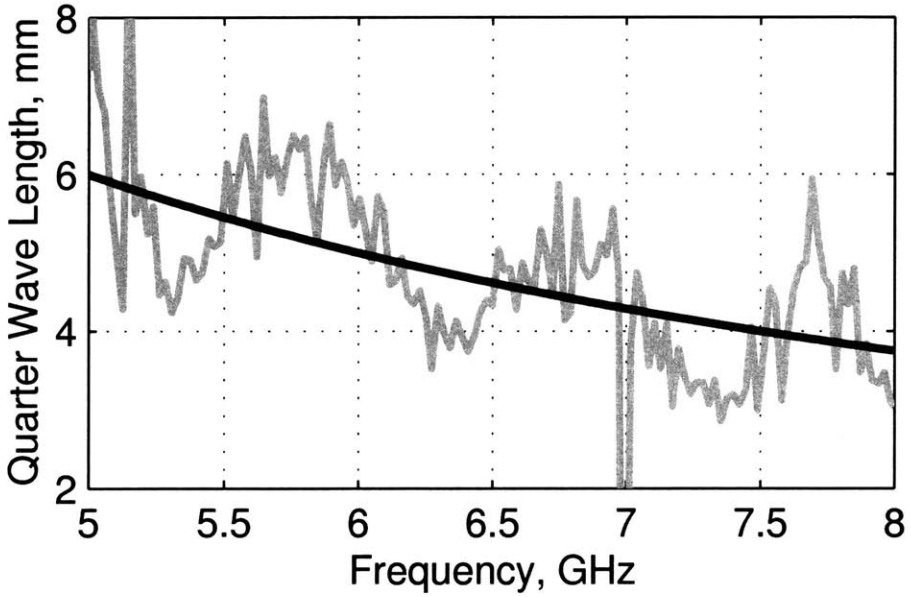

Figure 6-4: Quarter-wave line length as a function of frequency. The gray curve shows the value predicted from measurement, and the black curve shows the straight line fit to ϕ over the frequency range shown.

The final design of the filter shown in figure 6-5 has two 5 mm stubs separated by an internal distance of 4 mm. The stubs are centered on the microstrip.

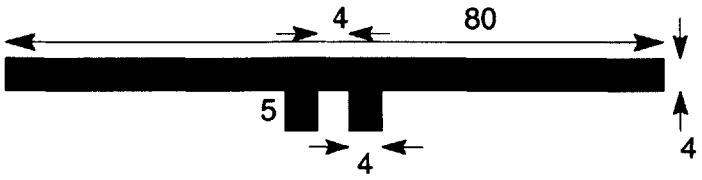

Figure 6-5: Microstrip stopband filter design with the dimensions labelled in millimeters.

6.5 Microstrip Filter Measurements

Measurements of the microstrip filter design are made on the non-dispersive substrate. The results are shown in figure 6-3(b). The filter produces a stopband at 5.87 GHz.

The microstrip filter is now measured at three different lateral positions on the dispersive substrate. The measurements are all comparable and the the average of the three is shown in figure 6-3(b). The microstrip filter bandwidth has been expanded significantly in comparison to the measurement on the non-dispersive substrate. The stopband also exceeds that of the dispersive substrate with the 4 mm microstrip only. The deep null at 5.76 GHz corresponds closely with the center of the stopband measured on the non-dispersive substrate.

6.6 Chapter Summary

The constitutive relations describing a left-handed metamaterial have previously been verified using waveguide and free-space measurements. It has been shown here that the properties of an LHM substrate can be predicted by the now standard reflection and transmission measurement and retrieval algorithm. In addition it has been shown that the natural properties of the substrate can be combined with those of a microstrip filter to enhance its bandwidth. A similar concept can be used to enhance the properties of other microstrip designs such as couplers.

The metamaterial used in these experiments was originally designed for antenna and waveguide applications and as a result the substrate has an uncharacteristically large height for microstrip applications. This thickness yields significant radiation losses in the measurements and simulation. LHM structures optimized for minimal substrate height are needed to reduce radiation losses.

Chapter 7

Conclusion

This thesis has investigated the construction, characterization, and design with left-handed metamaterials. A specific focus has been placed on the representation of LHM properties by constitutive parameters which can be used to predict the behavior of electromagnetic waves inside these media. Experimental results have been compared to the behavior predicted from the constitutive parameters obtained through retrieval from the simulated structure. In many cases good agreement has been exhibited.

A four-port device design has been introduced and demonstrated experimentally. It makes use of the frequency dependent reflection and refraction characteristics found at an LHM interface. Measurement results have demonstrated that the variation of refraction angle between positive, negative and imaginary, can be used to separate an incident signal, by spatially redirecting different bandwidths. More complicated four-port designs than the one used for measurements have been studied theoretically. The behavior and limitations of the device have been explored.

The use of a LHM substrate for a microstrip has been investigated. The LHM substrate consisting of symmetric split-ring resonators described by a Lorentz permeability in one direction, has been shown to behave in a way consistent with predictions from theory, where it is treated as a homogeneous material. The use of LHM substrates may allow for the enhancement of existing microstrip designs. As an example, the performance of a traditional microstrip stop band filter utilizing open circuit stubs has been enhanced with the use of an LHM substrate.

The ability to use constitutive parameters to describe LHM materials is essential for enabling engineers to design devices using these materials. LHM structures are needed that can easily and accurately be described by effective media parameters. This thesis has compared the consistency of effective media parameters to modern metamaterials, finding good agreement in many cases. However, many challenges still exist in realizing practical low-loss left-handed materials.

Bibliography

[1] J. A. Kong, *Electromagnetic Wave Theory.* EMW, 2000.

[2] V. G. Veselago, "The electrodynamics of substances with simultaneously negative values of ϵ and μ," *Soviet Physics USPEKI*, vol. 10, no. 509, pp. 509–514, January 1968.

[3] J. B. Pendry, A. J. Holden, W. J. Stewart, and I. Youngs, "Extremely low frequency plasmons in metallic mesostructures," *Phys. Rev. Lett.*, vol. 76, no. 25, pp. 4773–4776, June 1996.

[4] J. B. Pendry, A. J. Holden, D. J. Robbins, and W. J. Stewart, "Magnetism from conductors and enhanced nonlinear phenomena," *IEEE Trans. Microwave Thoery Tech.*, vol. 47, no. 11, pp. 2075–2084, November 1999.

[5] R. E. Collin, *Field theory of guided waves.* Oxfod University Press, 1991.

[6] D. R. Smith, W. J. Padilla, D. C. Vier, S. C. Nemat-Nasser, and S. Schultz, "Composite medium with simultaneously negative permeability and permittivity," *Phys. Rev. Lett.*, vol. 84, no. 18, pp. 4184–4187, May 2000.

[7] R. A. Shelby, D. R. Smith, S. C. Nemat-Nasser, and S. Schultz, "Microwave transmission through a two-dimensional, isotropic, left-handed metamaterial," *Applied Physics Letters*, vol. 78, no. 4, pp. 489–491, January 2001.

[8] R. A. Shelby, D. R. Smith, and S. Schultz, "Experimental verification of a negative index of refraction," *Science*, vol. 292, pp. 77–79, April 2001.

[9] J. B. Pendry, "Negative refraction makes a perfect lens," *Phys. Rev. Lett.*, vol. 85, no. 18, p. 3966, October 2000.

[10] J. B. Brock, A. A. Houck, and I. L. Chuang, "Focusing inside negative index materials," *Applied Physics Letters*, vol. 85, no. 13, pp. 2472–2474, September 2004.

[11] G. Eleftheriades and O. Siddiqui, "Negative refraction and focusing in hyperbolic transmission-line periodic grids," *IEEE Trans. Microwave Thoery Tech.*, vol. 53, no. 1, pp. 396–403, January 2005.

[12] A. Iyer and G. Eleftheriades, "Negative refractive index metamaterials supporting 2-D waves," *Microwave Symposium Digest, 2002 IEEE MTT-S International, Seattle, WA, USA*, vol. 2, no. 2-7, pp. 1067 - 1070, June 2002.

[13] A. Grbic and G. V. Eleftheriades, "Experimental verification of backward-wave radiation from a negative refractive index metamaterial," *J. Appl. Phys.*, vol. 92, no. 10, pp. 5930–5935, November 2002.

[14] W. Wang, "Directive antenna using metamaterial substrates," *MIT Masters Thesis*, June 2004.

[15] T. M. Grzegorczyk, Z. M. Thomas, and J. A. Kong, "Inversion of critical angle and Brewster angle in anisotropic negative metamaterials," *Applied Physics Letters*, 2005, submitted for publication.

[16] Z. M. Thomas, T. M. Grzegorczyk, B.-I. Wu, X. Chen, and J. A. Kong, "Design and measurement of a four-port device using left-handed metamaterials," *Optics Express*, 2005, submitted for publication.

[17] Z. M. Thomas, T. M. Grzegorczyk, and J. A. Kong, "Design of a four-port device utilizing metamaterials with multiple dispersive parameters," *New Journal of Physics*, 2005, submitted for publication.

[18] X. Chen, T. M. Grzegorczyk, B.-I. Wu, J. P. Jr., and J. A. Kong, "Improved method to retrieve the constitutive effective parameters of metamaterials," *Phys. Rev. E*, vol. 70, no. 016608, pp. 1–7, 2004.

[19] Z. M. Thomas, T. M. Grzegorczyk, B.-I. Wu, and J. A. Kong, "Enhanced microstrip stopand filter using a left-handed metamaterial substrate," *IEEE Microwave and Wireless Components Letters*, 2005, submitted for publication.

[20] E. Lifshitz, L. Landau, and L. Pitaevskii, *Electrodynamics of Continuous Media*, 2nd ed., ser. Course of Theoretical Physics. Butterworth-Heinemann, 1984, vol. 8.

[21] D. R. Smith and D. Schurig, "Electromagnetic wave propagation in media with indefinite permittivity and permeability tensors," *Phys. Rev. Lett.*, vol. 90, no. 7, p. 077405, February 2003.

[22] S. O´Brien and J. B. Pendry, "Magnetic activity at infrared frequencies in structured metallic photonic crystals," *J. Phys.: Condens. Matter*, pp. 6383–6394, June 2002.

[23] T. M. Grzegorczyk, C. D. Moss, J. Lu, X. Chen, J. P. Jr., and J. A. Kong, "Properties of left-handed metamaterials: transmission, backward phase, negative refraction, and focusing," *IEEE Trans. Microwave Thoery Tech.*, 2005, accepted for publication.

[24] M. M. I. Saadoun and N. Engheta, "Theoretical study of electromgnetic properties of non-local ω medium," *Progress in Electromagnetics Research*, vol. 9, no. 15, pp. 351–397, 1994.

[25] J. Huangfu, L. Ran, H. Chen, X. min Zhang, K. Chen, T. M. Grzegorczyk, and J. A. Kong, "Experimental confirmation of negative refractive index of a metamaterial composed of omega-like metallic patterns," *Applied Physics Letters*, vol. 84, no. 9, pp. 1537–1539, March 2004.

[26] L. Ran, J. Huangfu, H. Chen, X. Zhang, K. Cheng, T. M. Grzegorczyk, and J. A. Kong, "Experimental study on several left-handed metamaterials," *Progress In Electromagnetics Research*, vol. 51, no. 249-279, pp. 249–279, 2005.

[27] H. Chen, L. Ran, J. Huangfu, X. Zhang, K. Chen, T. M. Grzegorczyk, and J. A. Kong, "Left-handed materials composed of only S-shaped resonators," *Phys. Rev. E*, vol. 70, no. 057605, 2004.

[28] ——, "Negative refraction of a combined double S-shaped metamaterial," *Applied Physics Letters*, vol. 86, p. 151909, 2005.

[29] H. S. Chen, L. X. Ran, J. T. Huangfu, X. M. Zhang, K. S. Chen, T. M. Grzegorczyk, and J. A. Kong, "Magnetic properties of S-shaped split-ring resonators," *Progress In Electromagnetics Research*, vol. 51, pp. 249–279, 2005.

[30] X. Chen and C.-F. Li, "Lateral shift of the transmitted light beam through a left-handed slab," *Phys. Rev. E*, vol. 69, no. 066617, 2004.

[31] R. W. Ziolkowski, "Pulsed and CW Gaussian beam interactions with double negative metamaterial slabs," *Optics Express*, vol. 11, no. 7, pp. 662–681, April 2003.

[32] T. M. Grzegorczyk, X. Chen, J. P. Jr., J. Chen, B.-I. Wu, and J. A. Kong, "Reflection coefficients and Goos-Hänchen shifts in anisotropic and bianisotropic left-handed metamaterials," *PIER*, no. 51, pp. 83–113, 2005.

[33] H. Chen, L. Ran, J. Huangfu, X. Zhang, K. Chen, T. M. Grzegorczyk, and J. A. Kong, "T-junction waveguide experiment to characterize left-handed properties of metamaterials," *J. Appl. Phys.*, vol. 94, no. 6, pp. 3712–3716, September 2003.

[34] C. Caloz, C.-C. Chang, and T. Itoh, "Full-wave verification of the fundamental properties of left-handed materials in waveguide configurations," *J. Appl. Phys.*, vol. 90, no. 11, pp. 5483–5486, December 2001.

[35] D. R. Smith, P. Rye, J. J. Mock, D. C. Vier, and A. F. Starr, "Enhanced diffraction from a grating on the surface of a negative-index metamaterial," *Phys. Rev. Lett.*, vol. 93, no. 13, p. 137405, September 2004.

[36] L. Ran, J. Huangfu, H. Chen, X. Zhang, K. Chen, T. M. Grzegorczyk, and J. A. Kong, "Beam shifting experiment for the characterization of left-handed properties," *J. Appl. Phys.*, vol. 95, no. 5, pp. 2238–2241, March 2004.

[37] J. A. Kong, B.-I. Wu, and Y. Zhang, "Lateral displacement of a Gaussian beam reflected from a grounded slab with negative permittivity and permeability," *Appl. Phys. Lett.*, vol. 80, no. 12, pp. 2084–2086, 22 March 2002.

[38] ——, "A unique lateral displacement of a Gaussian beam transmitted through a slab with negative permittivity and permeability," vol. 33, no. 2, pp. 136–139, 20 April 2002.

[39] J. A. Kong, "Electromagnetic wave interaction with stratified negative isotropic media," *Progress in Electromagnetics Research*, vol. 35, pp. 1–52, 2002.

[40] R. W. Ziolkowski and E. Heyman, "Wave propagation in media having negative permittivity and permeability," *Physical Review E*, vol. 64, no. 056625, 2001.

[41] T. M. Grzegorczyk, M. Nikku, X. Chen, B.-I. Wu, and J. A. Kong, "Refraction laws for anisotropic media and their application to left-handed metamaterials," *IEEE Microwave Theory and Techniques*, vol. 53, no. 4, pp. 1443–1450, April 2005.

[42] S. N. Burokur, M. Latrach, and S. Toutain, "Study of the effect of dielectric split-ring resonators on microstrip-line transmission," *Microwave Optical Technol Lett*, vol. 44, no. 5, pp. 445–448, March 2005.

[43] D. M. Pozar, *Microwave Engineering*, 3rd ed. Wiley, January 2004.

[44] R. E. Collin, *Foundations for Microwave Engineering*, 2nd ed. Wiley-Interscience, 2001.

[45] D. Ghodgaonkar, V. Varadan, and V. Varadan, "Free space measurement of complex permittivity and complex permeability of magnetic materials at microwave frequencies," *IEEE Trans. on Inst. and Measurement*, vol. 39, no. 2, pp. 387–394, April 1990.

[46] R. Afzalzadeh, "Dielectric constant measurements of finite-size sheet at microwave frequencies by pseudo-brewsters angle method," *IEEE Trans. Microwave Theory Tech.*, vol. 46, no. 9, pp. 1307–1309, September 1998.

[47] V. V. Varadan, K. A. Jose, and V. K. Varadan, "In situ microwave characterization of nonplanar dielectric objects," *IEEE Trans. Microwave Theory Tech.*, vol. 48, no. 3, pp. 388–394, March 2000.

Appendix A

Microwave Measurement Theory and Demonstrations

In this appendix a brief review is given on the methods used to present microwave measurements in this thesis. The definition of the scattering matrix to characterize an N port device is presented along with its physical interpretation as it pertains to the work. The experimental equipment used for measurements is introduced and discussed. Measurements demonstrating known behavior are used to show that the equipment is operating properly. This is done by measuring the refraction angle from several dielectric prisms, and using it to calculate the permittivity of the material.

A.1 Microwave Measurements

This thesis is fundamentally based on microwave measurements of new materials. While the basic concepts needed are well understood and widely published, I believe it useful to provide a brief review for the reader, who is referred to [44] if additional information is desired.

In microwave measurements we are primarily interested in the response of the device under test (DUT) to an input signal. The DUT consists of one or more ports and each port can potentially have an input and output signal. A port is matched when an input signal is completely transmitted and results in no output signal at

the same port. If the port is mismatched, part of the input signal is reflected as an output signal. Matching is frequency dependent, and most devices are designed to be matched over a small bandwidth of frequencies.

In this thesis the scattering matrix is used to define the properties of a DUT. The scattering matrix relates the input and output voltages at each port. Equation A.1 gives the relationship between the input (V^+) and output (V^-) voltages for an N port device.

$$\begin{bmatrix} V_1^- \\ V_2^- \\ \cdots \\ V_N^- \end{bmatrix} = \begin{bmatrix} S_{11} & S_{12} & S_{13} & \cdots & S_{1N} \\ S_{21} & S_{22} & S_{23} & \cdots & S_{2N} \\ \cdots & \cdots & \cdots & \cdots & \cdots \\ S_{N1} & S_{N2} & S_{N3} & \cdots & S_{NN} \end{bmatrix} \begin{bmatrix} V_1^+ \\ V_2^+ \\ \cdots \\ V_N^+ \end{bmatrix}. \tag{A.1}$$

The S-parameter S_{nm} is a complex quantity representing the ratio of the output signal at port n to the input signal at port m. The amplitude of S_{nm} represents the relative amplitudes of the two signals, and the angle represents the relative phase delay.

Because the measurement equipment can connect to only two ports at a time, the two port device is primarily of interest. The S-parameters can be measured using a vector network analyzer by sending an input signal into port 1 and measuring the reflection (S_{11}) and transmission (S_{21}) of the signal. The remaining S-parameters, S_{22} and S_{12} represent the reflection and transmission going from port 2 to port 1.

The S-parameters represent the ratio of the voltages of the respective signals. Typically we are interested in transmitted power which is given by $|S_{mn}|^2$. Most of the measurements presented in this thesis are given as power in dB. The measured S-parameter S_{mn} is converted to power in dB by the following equation.

$$\mathrm{P}_{\mathrm{dB}mn} = 20 \log_{10} (|S_{mn}|) \tag{A.2}$$

In a lossless system the S-parameters have the property that the conjugate transpose of any column in the S-matrix times that column is unity [44]. For the two port

device the statement can be written mathematically as

$$S_{11}^* S_{11} + S_{21}^* S_{21} = 1. \tag{A.3}$$

More simply the amplitudes at the input and output must add to one in a lossless device.

A.2 Measurement Equipment

Electromagnetic measurements at microwave frequencies can be made using a vector network analyzer (VNA). While simpler tools do exist, the VNA allows for the complete measurement of the S-parameters of a device, including both amplitude and phase. All of our work is done using an Hewlett-Packard 8510B, which is capable of taking measurements of signals from megahertz, to over twenty gigahertz. The actual range depends on the synthesized sweep signal generator attached to, and controlled by the VNA. In this work, an HP 83640A synthesized sweep was used, with a dynamic range from 10 MHz to 40 GHz. Our interest is confined to the frequencies from 1 to 20 GHz.

The input and output of the VNA is done through an S-parameter test kit. Cables with an SMA compatible connector are attached and can be connected to various devices, typically cables and SMA to waveguide adapters. The HP 8516A S-parameter test kit is used in all measurements discussed here.

In order to export data from the VNA, a GPIB interface card from National Instruments was installed on a PC and connected to the VNA. Commands found in the Instrument Control MATLAB toolbox are used to both fully control the VNA and also to download data for analysis.

Equipment is also used to maneuver the transmitters and receivers into the right location for measurements. In many cases measurements are needed over frequency and position. The frequency dimension is quickly scanned at each position by the VNA, the position, however, must be adjusted via motor control. Linear motor

controls are used to control linear position and angular position as is needed for a particular experiment.

A listing of the equipment used in this thesis is given in appendix B.

A.3 Verification Measurements

In order to determine if our measurement setup and equipment is working as expected, measurements with expected results demonstrating well known properties of certain materials are conducted. The typical setup for these measurements is shown in figure A-1. The setup is a parallel plate waveguide consisting of a set of aluminum plates measuring 15 by 21 inches. The black strips in the figure are the microwave absorbing material that is used to line the sides of the plates. This absorber supported the top plate, maintaining the appropriate plate separation and minimized reflections from the sides of the plates. In this photo a teflon prism is about to be measured.

Two SMA to rectangular waveguide adapters were used to interface between the SMA cables connected to the VNA and the parallel plate waveguide. In this case they are WR90 adapters which cover the X band of the microwave spectrum (8.2 to 12.4 GHz). The receiver on the left of the figure is mounted on a motor controlled platform that is moved along the the baseline of the plates. Measurements are taken over a range of frequencies at each position.

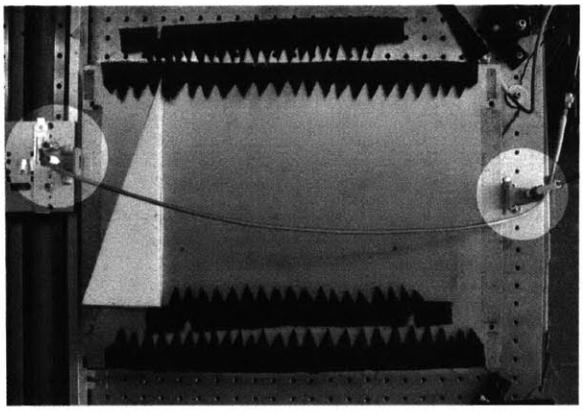

Figure A-1: Phase based retrieval experimental setup (photo).

A.3.1 Refraction Measurement

To demonstrate the proper operation of the measurement equipment a simple measurement is preformed to calculate the relative permittivity for air, Teflon, and Plexiglas. The three media are assumed to be nonmagnetic allowing for the direct calculation of the relative permittivity by use of Snell's law of refraction [1]. Figure A-2 shows an overview of the measurement. A wave incident from port one enters the prism at normal incidence and propagates into the material without refraction. It is then incident upon the second interface at the angle θ_i. Snell's refraction law can predict the transmission angle θ_t. The black arrows show the path of the wave, and the gray lines perpendicular to the transmitted beam show the phase fronts. By measuring the distance between phase fronts, d, or equivalently finding the rate in change of phase delay along the baseline, we can determine the index of refraction.

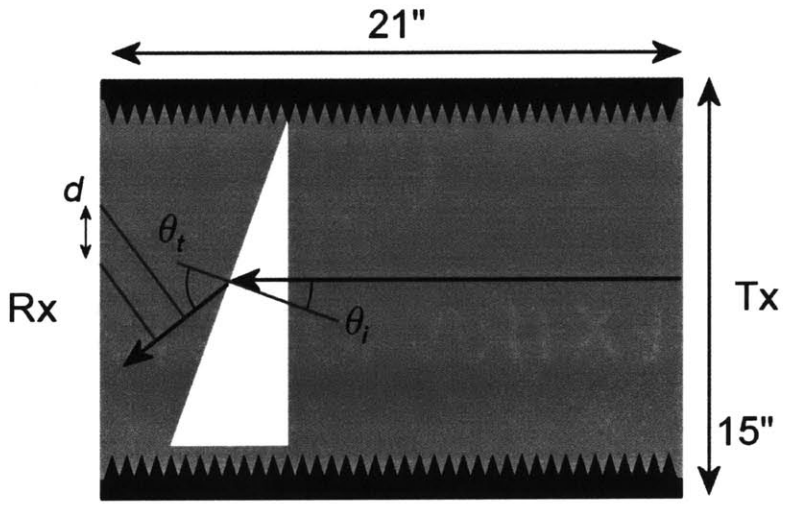

Figure A-2: Schematic for right-handed prism phase based retrieval.

For measurements, a right triangular prism is cut for both Teflon and Plexiglas. The side lengths are 4, 11, and 11.7 inches. The prism angle is 20.0°. The distance from the receive baseline is arbitrary provided it is small enough that the refraction angle can be measured. Various positions are used in measurements to verify consistent results.

The waveguide transmitter is approximated as a point source. The phase fronts are

circular and because the distance is known can be predicted. The curvature is removed by subtracting the predicted free space phase delay so that the change in phase along the baseline is easily fit to a straight line. Fitting the corrected measurement to a first order polynomial the slope m is found. The freespace wavelength is known and we solve sequentially for d, θ_t, and the relative permittivity of the prism, ϵ_r. Equations A.5−A.6 follow directly from the geometry and Snell's law.

$$d = \frac{2\pi}{m} \tag{A.4}$$

$$\theta_t = \arcsin\left(\frac{\lambda}{d}\right) + \theta_i \tag{A.5}$$

$$\epsilon_r = \left(\frac{\sin\theta_t}{\sin\theta_i}\right)^2 \tag{A.6}$$

To demonstrate these equations explicitly, measurements taken at 10.8 GHz for air, Teflon, and Plexiglas are shown in figure A-3. The solid black curve shows the measured phase data, zeroed to the position $x = -4$ cm. The dashed black curve is the same in all three cases and is the predicted phase for air. The solid gray curve is the difference between the measured curve and the air curve. Finally the dashed gray curve is a straight line fit the the difference curve. Since only the slope of the dashed gray curve is important the vertical position is immaterial and for clarity has been offset. The slope of the fit, m is in degrees per centimeter. From these figures we see that position is measured from bottom to top in figure A-2.

These measurement results show that the air is non-refracting ($m \approx 0$) while Teflon and Plexiglas both refract the incident wave, but with Plexiglas having a higher index of refraction as can be seen from the larger slope. Using equations A.5-A.6 we find the relative permittivity for the three substances over the measured frequencies. The results are shown in figure A-4. These results are the averaged results of two measurements for air, four measurements for Teflon, and five measurements for Plexiglas. The average permittivity over frequency for each of the five curves are given in table A.1.

While more sophisticated retrieval techniques are available to do determine con-

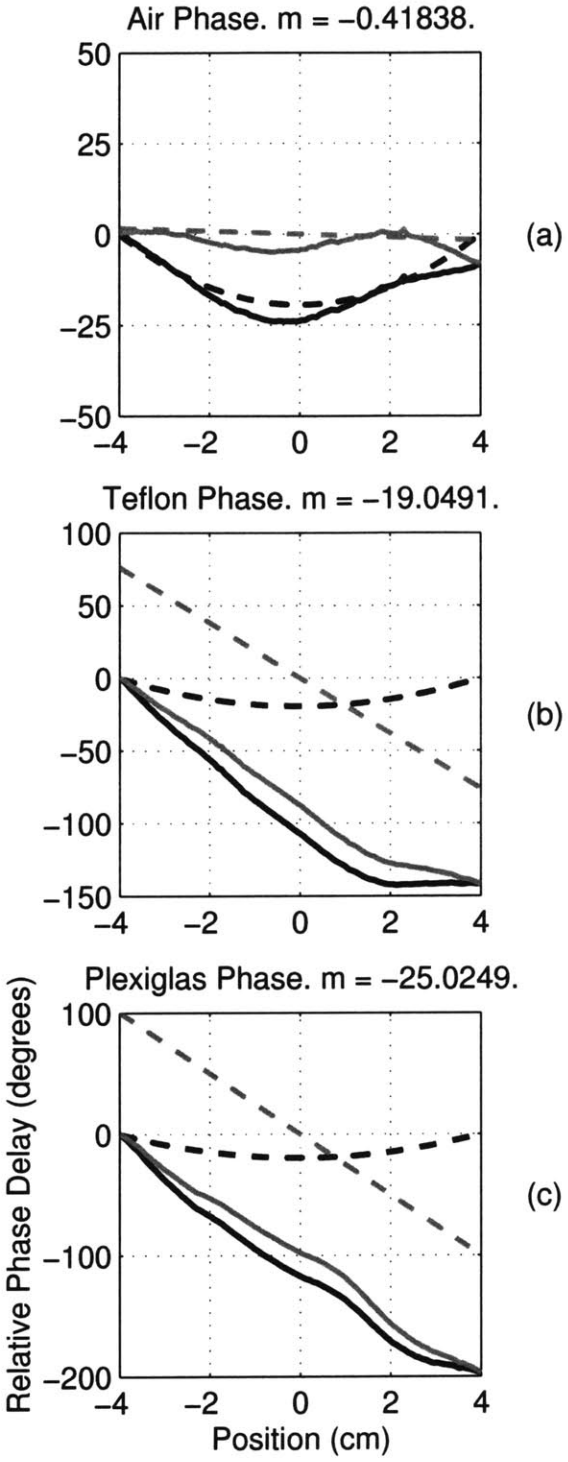

Figure A-3: Baseline phase delay for air (a), Teflon (b), and Plexiglas (c). *Solid Black*– Measurement result. *Dashed Black*– Theoretical air prism result. *Solid Gray*– Difference between measurement and air. *Dashed Gray*– Offset straight line fit to difference curve.

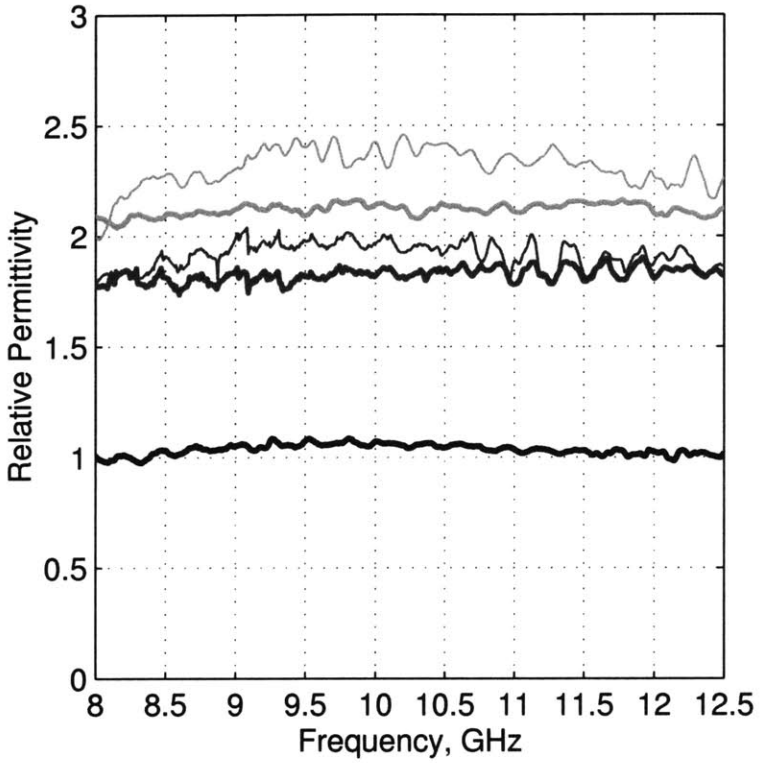

Figure A-4: Measured relative permittivity as a function of frequency for air, Teflon, and Plexiglas. *Thick Black*– Air. *Thick Dark Gray*– Teflon average. *Thin Dark Gray*– Teflon best. *Thick Light Gray*– Plexiglas average. *Thin Light Gray*– Plexiglas best.

Table A.1: Average permittivity of air, Teflon, and Plexiglas.

Measurement	Average Permittivity
Air	1.0343
Teflon, averaged measurements	1.8269
Teflon, best measurement	1.9163
Plexiglas, averaged measurements	2.1208
Plexiglas, best measurement	2.3145

stitutive parameters of parameters, this technique gives satisfactory results. The literature includes many reports of the permittivity of Teflon and Plexiglas. In [45] teflon is measured to have a relative permittivity of $\epsilon_r = 2.0$, $\mu_r = 1.0$. The values of Plexiglas in general have greater frequency dependence and are less consistent from reference to reference. For frequencies between 10 GHz and 13 GHz, [46] reports values of $\epsilon_r = 2.55 \pm .13$. In [47] the authors report values from 8 GHz to 12.5 GHz with typical values of $\epsilon_r = 2.68$.

The results for Teflon and Plexiglas are both slightly lower than expected, however, there are several factors that could contribute to this. For example, the wave will be refracted at the first boundary because the wavefront is in fact curved. Also, the prisms used were not single solid blocks, but rather consisted of two quarter inch thick pieces that were stacked. It is possible that a portion of the wave went through this gap, and there is a possibility of a gap above the sample. Of course numerous other factors could also contribute to measurement errors but are tolerated here.

Appendix B

Equipment List

The following is a listing of the specialized equipment used in this thesis.

- HP 8510B Network Analyzer
- HP8516A S-Parameter Test Kit
- 83640A Synthesized Sweep
- GPIB Interface Card
- Personal Computer
- WR-90 Waveguide to SMA Adapter
- 50 Ω Air Cables
- SMA Cables
- Precision Experimentaters Table
- Computer Controlled Positioning System
- Parallel Plate Waveguide
- Microwave Absorber
- Teflon and Plexiglas

- CST Microwave Studio
- Metamaterials

Appendix C

Demonstration of Dispersion Relationship

Here we a mathematical demonstration of the dispersion relationship, 2.4.

We begin with Maxwell's equations for time harmonic linear media and the assumed the solution. The dispersion relationship is thus the constraint under which the assumed solutions satisfies Maxwell's equations.

$$\nabla \times \overline{E} = i\omega\bar{\bar{\mu}} \cdot \overline{H} \tag{C.1}$$

$$\nabla \times \overline{H} = -i\omega\bar{\bar{\epsilon}} \cdot \overline{E} \tag{C.2}$$

The assumed solution is

$$\overline{E} = \hat{y}\mathrm{E}_y = \hat{y}e^{i(k_x x + k_y y)}. \tag{C.3}$$

Substituting equation C.3 into C.1 we have

$$\nabla \times \overline{E} = \begin{vmatrix} \hat{x} & \hat{y} & \hat{z} \\ \partial_x & \partial_y & \partial_z \\ \mathrm{E}_x & \mathrm{E}_y & \mathrm{E}_z \end{vmatrix} = -\hat{x}ik_z\mathrm{E}_y + \hat{z}ik_x\mathrm{E}_y = i\omega\bar{\bar{\mu}} \cdot \overline{H} \tag{C.4}$$

Writing in matrix form we find.

$$\begin{bmatrix} -k_z \mathrm{E}_y \\ 0 \\ k_x \mathrm{E}_y \end{bmatrix} = \begin{bmatrix} \omega \mu_x \mathrm{H}_x \\ \omega \mu_y \mathrm{H}_y \\ \omega \mu_z \mathrm{H}_z \end{bmatrix} \tag{C.5}$$

We can now solve for each component of $\overline{H}$.

$$\overline{H} = \hat{x}\frac{-k_z}{\omega \mu_x}\mathrm{E}_y + \hat{z}\frac{k_x}{\omega \mu_z}\mathrm{E}_y \tag{C.6}$$

We must also satisfy Ampere's Law. Substituting the expressions for both fields into equation C.2 we have

$$\begin{vmatrix} \hat{x} & \hat{y} & \hat{z} \\ \partial_x & \partial_y & \partial_z \\ \mathrm{H}_x & 0 & \mathrm{H}_z \end{vmatrix} = \begin{bmatrix} 0 \\ \left(\frac{ik_x^2}{\omega \mu_x} + \frac{ik_z^2}{\omega \mu_z}\right)\mathrm{E}_y \\ 0 \end{bmatrix} = \begin{bmatrix} 0 \\ i\omega \epsilon_y \mathrm{E}_y \\ 0 \end{bmatrix} \tag{C.7}$$

Canceling the E_y and i and solving for k_z^2 we have

$$k_z^2 = \omega^2 \epsilon_y \mu_z - \frac{\mu_x}{\mu_z} k_x^2. \tag{C.8}$$

If we change notation to allow the constitutive parameters to represent the relative values the equation takes the form of equation 2.4.

Appendix D

TE Reflection and Transmission at the Interface of Two Diagonalizable Media

D.1 Definition of Geometries

We begin by defining the three coordinate systems needed to find the transmission and reflection coefficients. The x, y, z coordinate system defines the orientation of the interface between the two media. It is referred to as the interface coordinate system. The x_A, y_A, z_A defines the principles axis in the incidence medium, Medium A. It is rotated an angle ϕ_A in the clockwise direction relative to the interface coordinate system. A positive rotation is shown. The x_B, y_B, z_B defines the principles axis in the transmitted medium, Medium B. The angle ϕ_B represents the angle of this coordinate system and is measured the same way. A negative rotation is shown.

The rotation matrix $\overline{\overline{\mathrm{T}}}_{A,B}$, is used to move between the material coordinate systems and the interface coordinate system.

$$\begin{bmatrix} x \\ y \\ z \end{bmatrix} = \begin{bmatrix} cos\phi_{A,B} & 0 & sin\phi_{A,B} \\ 0 & 1 & 0 \\ -sin\phi_{A,B} & 0 & cos\phi_{A,B} \end{bmatrix} \begin{bmatrix} x_{A,B} \\ y_{A,B} \\ z_{A,B} \end{bmatrix} \tag{D.1}$$

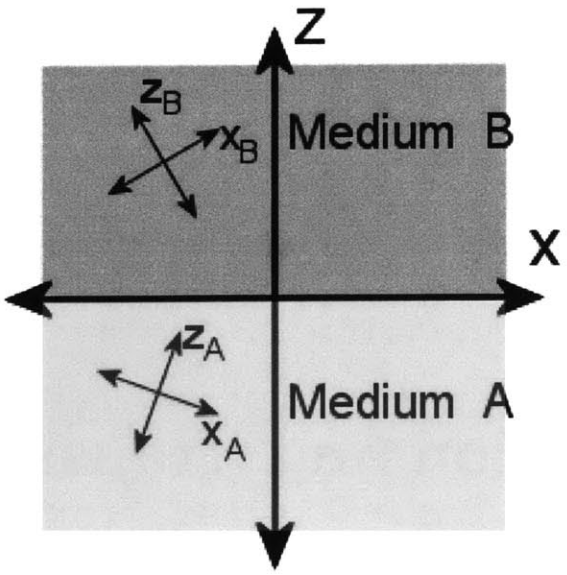

Figure D-1: Coordinate systems at the boundary of two diagonalizable anisotropic media.

The constitutive relations in the Medium A, and B coordinate systems are $\overline{\overline{\epsilon}}_A, \overline{\overline{\mu}}_A$ and $\overline{\overline{\epsilon}}_B, \overline{\overline{\mu}}_B$ respectively. In this article we assume that the tensors are diagonalizable in their principle axis coordinate systems. To find the corresponding tensors in the interface coordinate system we note the relation:

$$\overline{D} = \overline{\overline{\epsilon}} \cdot \overline{E} \qquad \overline{B} = \overline{\overline{\mu}} \cdot \overline{H} \tag{D.2}$$

and

$$\overline{C} = \overline{\overline{\mathrm{T}}}_{A,B} \cdot \overline{C}_{A,B} \tag{D.3}$$

where $\overline{C}$ is $\overline{E}, \overline{H}, \overline{D}$, or $\overline{B}$. We can then write:

$$\overline{D}_i = \underbrace{\overline{\overline{\mathrm{T}}}_A \cdot \overline{\overline{\epsilon}}_A \cdot \overline{\overline{\mathrm{T}}}_A^{-1}}_{\overline{\overline{\epsilon}}_i} \cdot \overline{E}_A \tag{D.4}$$

D.2 Fields

The dispersion relationship, equation 2.4, and the assumed incidence,

$$\overline{E} = \hat{y} E_o e^{i(k_x x + k_z z)}, \tag{D.5}$$

are used to derive the incident, reflected, and transmitted fields.

D.2.1 Incident Fields

The field is assumed to be incident from Medium A to Medium B. We first write the field in terms of principle coordinate system of Medium A.

$$\overline{E}_A = \hat{y}_A E_o e^{i(k_{x_A} x_A + k_{z_A} z_A)} \tag{D.6}$$

$$\overline{H}_A = \left(-\hat{x}_A \frac{k_{z_A}}{\mu_{x_A}} + \hat{z}_A \frac{k_{x_A}}{\mu_{z_A}} \right) \frac{E_o}{\omega} e^{i(k_{x_A} x_A + k_{z_A} z_A)} \tag{D.7}$$

Using the rotation matrix $\overline{\overline{\mathrm{T}}}_A$ the fields can be written in terms of x, y, and z.

$$\begin{bmatrix} H_x \\ H_y \\ H_z \end{bmatrix} = \overline{\overline{\mathrm{T}}}_A \cdot \begin{bmatrix} H_{x_A} \\ 0 \\ H_{z_A} \end{bmatrix} \tag{D.8}$$

Substituting and simplifying:

$$\begin{bmatrix} H_x \\ 0 \\ H_z \end{bmatrix} = \begin{bmatrix} \frac{k_{x_A}}{\mu_{z_A}} sin\phi_A - \frac{k_{z_A}}{\mu_{x_A}} cos\phi_A \\ 0 \\ \frac{k_{z_A}}{\mu_{x_A}} sin\phi_A + \frac{k_{x_A}}{\mu_{z_A}} cos\phi_A \end{bmatrix} \frac{E_o}{\omega} e^{i(k_{x_A} x_A + k_{z_A} z_A)} \tag{D.9}$$

Letting

$$k_x = k_{x_A} cos\phi_A + k_{z_A} sin\phi_A \tag{D.10}$$

$$k_z = k_{z_A} cos\phi_A - k_{x_A} sin\phi_A \tag{D.11}$$

$$C_1 = \frac{k_{x_A}}{\mu_{z_A}} sin\phi_A - \frac{k_{z_A}}{\mu_{x_A}} cos\phi_A \tag{D.12}$$

$$C_2 = \frac{k_{z_A}}{\mu_{x_A}} sin\phi_A + \frac{k_{x_A}}{\mu_{z_A}} cos\phi_A \tag{D.13}$$

we can write the incident field in the interface coordinate system.

$$\overline{E}_i = \hat{y} E_o e^{i(k_x x + k_z z)} \tag{D.14}$$

$$\overline{H}_i = [\hat{x} C_1 + \hat{z} C_2] \frac{E_o}{\omega} e^{i(k_x x + k_z z)} \tag{D.15}$$

D.2.2 Reflected Field

The transmitted field is simply written based on our knowledge of phase matching and the incident field. We introduce R as the reflection coefficient.

$$\overline{E}_r = \hat{y} R E_o e^{i(k_x x - k_z z)} \tag{D.16}$$

$$\overline{H}_r = (-\hat{x} C_1 + \hat{z} C_2) \frac{R E_o}{\omega} e^{i(k_x x - k_z z)} \tag{D.17}$$

D.2.3 Transmitted Field

We begin by writing the transmitted field in Medium B's coordinate system.

$$\overline{E}_B = \hat{y}_B E_o e^{i(k_{x_B} x_B + k_{z_B} z_B)} \tag{D.18}$$

$$\overline{H}_B = \left(-\hat{x}_B \frac{k_{z_B}}{\mu_{x_B}} + \hat{z}_B \frac{k_{x_B}}{\mu_{z_B}} \right) \frac{E_o}{\omega} e^{i(k_{x_B} x_B + k_{z_B} z_B)} \tag{D.19}$$

Using the following substitutions

$$k_{x_t} = k_{x_B} cos\phi_B + k_{z_B} sin\phi_B \tag{D.20}$$

$$k_{z_t} = k_{z_B} cos\phi_B - k_{x_B} sin\phi_B \tag{D.21}$$

$$F_1 = \frac{k_{x_B}}{\mu_{z_B}} sin\phi_B - \frac{k_{z_B}}{\mu_{x_B}} cos\phi_B \tag{D.22}$$

$$F_2 = \frac{k_{z_B}}{\mu_{x_B}} sin\phi_B + \frac{k_{x_B}}{\mu_{z_B}} cos\phi_B \tag{D.23}$$

and noting that $k_x = k_{x_t}$, we rewrite in the interface coordinate system.

$$\overline{E}_t = \hat{y} T E_o e^{i(k_x x + k_{z_t} z)} \tag{D.24}$$

$$\overline{H}_t = (\hat{x} F_1 + \hat{z} F_2) \frac{T E_o}{\omega} e^{i(k_x x + k_{z_t} z)} \tag{D.25}$$

Equating equations D.10 and D.20 we have:

$$k_{x_A} cos\phi_A + k_{z_A} sin\phi_A = k_{x_B} cos\phi_B + k_{z_B} sin\phi_B \tag{D.26}$$

Assuming the rotation of the two materials is known, along with the incident field, all that is unknown is k_{x_B} and k_{z_B}. We can use the dispersion relation equation 2.4 as our second equation to solve the equation explicitly.

D.3 Transmission and Reflection Coefficients

Now we wish to find the coefficients R and T. Assuming the interface is at $z = 0$ and recalling the boundary condition $\hat{n} \times (\overline{E}_1 - \overline{E}_2) = 0$ we can find R in just a few steps.

$$\hat{n} \times (\overline{E}_1 - \overline{E}_2) = 0 \tag{D.27}$$

$$-\hat{z} \times ((\overline{E}_i + \overline{E}_r) - \overline{E}_t) = 0 \tag{D.28}$$

$$E_{i_y} + E_{r_y} = E_{t_y} \tag{D.29}$$

$$1 + R = T \tag{D.30}$$

Using the boundary condition on the magnetic field

$$\hat{n} \times \left(\overline{H}_1 - \overline{H}_2\right) = 0 \tag{D.31}$$

$$-\hat{z} \times \left(\left(\overline{H}_i + \overline{H}_r\right) - \overline{H}_t\right) = 0 \tag{D.32}$$

$$-\hat{y}H_{i_x} + \hat{y}H_{r_x} + \hat{y}H_{t_x} = 0 \tag{D.33}$$

$$-C_1 + C_1R + F_1T = 0 \tag{D.34}$$

Finally we can solve for R and T

$$R = \frac{1 - \frac{F_1}{C_1}}{1 + \frac{F_1}{C_1}} \tag{D.35}$$

$$T = \frac{2}{1 + \frac{F_1}{C_1}} \tag{D.36}$$